



# Numerical simulation of a jet in crossflow. Application to GRID computing

Simone Camarri, Vanessa Mariotti, Maria Vittoria Salvetti, Bruno Koobus,  
Alain Dervieux, Hervé Guillard, Stephen F. Wornom

## ► To cite this version:

Simone Camarri, Vanessa Mariotti, Maria Vittoria Salvetti, Bruno Koobus, Alain Dervieux, et al.. Numerical simulation of a jet in crossflow. Application to GRID computing. [Research Report] RR-5638, INRIA. 2006, pp.80. inria-00070369

**HAL Id: inria-00070369**

**<https://inria.hal.science/inria-00070369>**

Submitted on 19 May 2006

**HAL** is a multi-disciplinary open access archive for the deposit and dissemination of scientific research documents, whether they are published or not. The documents may come from teaching and research institutions in France or abroad, or from public or private research centers.

L'archive ouverte pluridisciplinaire **HAL**, est destinée au dépôt et à la diffusion de documents scientifiques de niveau recherche, publiés ou non, émanant des établissements d'enseignement et de recherche français ou étrangers, des laboratoires publics ou privés.

***Numerical simulation of a jet in crossflow.  
Application to GRID computing.***

Vanessa Mariotti,  
Simone Camarri,  
Maria Vittoria Salvetti,  
Bruno Koobus,  
Alain Dervieux,  
Hervé Guillard,  
Stephen Wornom

**N° 5638**

Juillet 2005

Thème NUM



***rapport  
de recherche***



## Numerical simulation of a jet in crossflow. Application to GRID computing.

Vanessa Mariotti\*,  
Simone Camarri†,  
Maria Vittoria Salvetti‡,  
Bruno Koobus§,  
Alain Dervieux¶,  
Hervé Guillard||,  
Stephen Wornom\*\*

Thème NUM — Systèmes numériques  
Projet Smash

Rapport de recherche n° 5638 — Juillet 2005 — 80 pages

**Abstract:** This work describes the LES and hybrid RANS/LES simulations for a rounded jet issuing normally into a cross-flow, also known as jet in cross-flow (JICF). This test case is particularly suitable to study the capability of LES and hybrid approaches because of the presence of both separated and non-separated boundary layer regions. Simulations are performed for a jet to cross-flow velocity ratio  $R = 2$  and a  $Re = 82000$ , based on the cross-flow velocity and the jet diameter. The simulations are carried out using a numerical solver of 3D compressible flows, named AERO. Large scales coherent structures observed in experimental flow visualisations are reproduced in both the simulations and the obtained mean and turbulent statistics are compared to experimental data. LES simulations seem to follow in a better way the experimental results than LNS. In the second case, there is not sufficient mixing between jet and cross-flow and thus the jet bends less and a too large recirculation bubble forms behind the jet. This test case has been chosen also because we can split the domain in two different regions, the pipe and the cross-flow, with a limited

\* Dipartimento di Ingegneria Aerospaziale, Università di Pisa, Via Caruso, 56122 Pisa, Italy

† Dipartimento di Ingegneria Aerospaziale, Università di Pisa, Via Caruso, 56122 Pisa, Italy

‡ Dipartimento di Ingegneria Aerospaziale, Università di Pisa, Via Caruso, 56122 Pisa, Italy

§ Université de Montpellier II, Département de Mathématiques, CC.051 34095 MONTPELLIER Cedex 5, France and INRIA

¶ INRIA, 2004 Route des Lucioles, BP. 93, 06902 Sophia-Antipolis, France

|| INRIA, 2004 Route des Lucioles, BP. 93, 06902 Sophia-Antipolis, France

\*\* INRIA, 2004 Route des Lucioles, BP. 93, 06902 Sophia-Antipolis, France

interface. This is a good characteristic in order to test GRID computing, which is another goal of this work. GRID computing is an alternative way to carry out parallel computations with respect to the classical clusters or parallel computers. It consists in using computers allocated in different sites exchanging data between the sites through the web (Internet). In the present work, GRID computing is tested for both JICF and for the flow in a pipe.

**Key-words:** Large-eddy simulation, hybrid RANS/LES simulation, jet in crossflow, GRID computing

# Simulation numérique d'un jet en présence d'un écoulement latéral. Application au calcul parallèle GRID.

**Résumé :** Ce rapport décrit la simulation LES et la simulation hybride LES/RANS d'un jet circulaire dans un écoulement latéral (JICF de l'expression anglaise *jet in crossflow*). Ce cas test est bien adapté à l'étude et à la validation des approches LES et hybride, car il est caractérisé par la présence de couches limites ainsi que de structures tourbillonnaires complexes issues de la séparation des couches limites. Les simulations ont été conduites pour une configuration caractérisée par un rapport entre la vitesse du jet et celle de l'écoulement latéral  $R=2$  et par un nombre de Reynolds  $Re=82000$ . Les simulations ont été effectuées en utilisant un solveur numérique pour des écoulements compressibles 3D (AERO). Les caractéristiques principales de l'écoulement ont été capturées avec les deux différentes approches, mais les résultats de la simulation LES sont en général en meilleur accord avec les données expérimentales que ceux de la simulation hybride. En effet, dans cette dernière simulation le mélange entre le jet et l'écoulement latéral n'est pas bien pris en compte. Par conséquent, la déviation de la trajectoire du jet est moins importante que dans les expériences et on a une région de recirculation derrière le jet trop importante. Ce cas test a été choisi aussi parce que le domaine de calcul peut être divisé en deux parties, le tuyau et la chambre, ayant une interface limitée. Ceci est désirable pour l'application au calcul GRID, ce qui représente un autre objectif de ce travail. Le calcul GRID est un calcul parallèle qui utilise des ordinateurs situés dans différents laboratoires, en échangeant les données parmi les différents sites à travers le web (Internet). Dans ce travail, on utilise le calcul GRID pour la simulation du JICF et de l'écoulement dans un tuyau, afin de donner une contribution à l'évaluation des performances de cette approche de calcul parallèle.

**Mots-clés :** Simulation des grandes échelles, simulation hybride RANS/LES, jet en écoulement latéral, calcul parallèle GRID

## Contents

<b>1</b>	<b>Introduction</b>	<b>6</b>
<b>2</b>	<b>Turbulent flows</b>	<b>7</b>
2.1	Direct numerical simulation . . . . .	7
2.2	Reynolds-Averaged Navier-Stokes Equations . . . . .	10
2.2.1	Standard $k$ - $\epsilon$ model . . . . .	11
2.3	Large Eddy Simulation . . . . .	12
2.3.1	SGS modeling . . . . .	12
2.3.2	Filtered equations of the motion . . . . .	13
2.3.3	Smagorinsky's model . . . . .	15
2.3.4	Resolution requirements for LES . . . . .	16
2.3.5	Boundary conditions . . . . .	16
2.4	Limited Numerical Scales . . . . .	17
<b>3</b>	<b>AERO code</b>	<b>18</b>
3.1	Set of governing equations . . . . .	18
3.2	Space discretization . . . . .	19
3.2.1	Convective fluxes . . . . .	20
3.2.2	Diffusive fluxes . . . . .	22
3.3	Boundary conditions . . . . .	23
3.4	Time advancing . . . . .	23
3.4.1	Explicit time advancing . . . . .	24
3.4.2	Implicit time advancing . . . . .	24
3.5	Parallelization . . . . .	25
3.5.1	Explicit time integration procedure . . . . .	25
3.5.2	Implicit time integration procedure . . . . .	25
<b>4</b>	<b>Grid Computing</b>	<b>26</b>
4.1	MecaGRID project . . . . .	26
4.2	MecaGRID resources . . . . .	26
4.3	Establishment of Grid: Globus and VPN . . . . .	26
4.4	Parallelism and message passing . . . . .	27
<b>5</b>	<b>Jet in cross-flow. Flow dynamics and test-case configuration</b>	<b>29</b>
5.1	Vortex system associated with the transverse jet . . . . .	30
5.1.1	Class 1 structures . . . . .	31
5.1.2	Class 2 structures . . . . .	31
5.2	Flow configuration . . . . .	32
5.3	Mesh geometry . . . . .	33
5.4	LES validation test case . . . . .	35
5.5	Boundary and initial conditions . . . . .	36

<b>6</b>	<b>Results of the LES simulation</b>	<b>41</b>
6.1	Simulation parameters . . . . .	41
6.2	Reproduction of general flow characteristics . . . . .	42
6.2.1	Horseshoe vortex (HSV) . . . . .	44
6.2.2	Counter-rotating vortex pair (CRVP) . . . . .	46
6.2.3	Ring like vortices (RLV) . . . . .	49
6.2.4	Upright vortices (URV) . . . . .	49
6.3	Flow statistics . . . . .	50
6.3.1	Mean velocities . . . . .	50
6.3.2	Turbulent kinetic energy . . . . .	52
6.3.3	Turbulent shear stress . . . . .	54
<b>7</b>	<b>Results of the LNS simulation</b>	<b>54</b>
7.1	Simulation parameters . . . . .	54
7.2	Reproduction of general flow characteristics . . . . .	55
7.2.1	Horseshoe vortex (HSV) . . . . .	59
7.2.2	Ring like vortices (RLV) . . . . .	60
7.2.3	Counter-rotating vortex pair (CRVP) . . . . .	60
7.2.4	Upright vortices (URV) . . . . .	62
7.3	Flow statistics . . . . .	62
7.3.1	Mean velocities . . . . .	62
7.3.2	Turbulent kinetic energy and turbulent shear stress . . . . .	67
<b>8</b>	<b>Grid results</b>	<b>68</b>
8.1	Computational resources . . . . .	68
8.2	Pipe with 241K vertices . . . . .	69
8.3	JICF with 398K vertices . . . . .	73
<b>9</b>	<b>Conclusions</b>	<b>76</b>



## 1 Introduction

The present work is part of two research projects: the first is aimed at developing and validating numerical codes, based on LES (Large-Eddy Simulation) and hybrid RANS (Reynolds averaged Navier-Stokes)/LES approaches, in order to solve unsteady and separated fluid dynamic problems and is carried out in a collaboration between the University of Pisa and the INRIA. The latter is the MecaGRID project and is aimed at testing the Globus Toolkit, a framework used for Grid Computing. The MecaGRID project is sponsored by the French Ministry of Research through the ACI-GRID program <sup>1</sup> and it is a joint project between INRIA-Sophia Antipolis (France), CEMEF of the ENSMP (Ecole de Mines de Paris), located in Sophia Antipolis (France) and IUSTI (Institut Universitaire des Systèmes Thermiques et Industriels), located in Marseille (France).

The interest in developing methodologies to simulate turbulent flows is due to the high computational cost of direct numerical simulation (DNS), which is, in most cases of practical interest, not affordable with the present computational resources. Indeed, due to the fact that the computational cost increases roughly with the 3rd power of the Reynolds number, DNS may be used only for low Reynolds numbers and simple geometries, as explained in details in Section 2. An alternative to DNS is represented by the RANS (Reynolds Averaged Navier-Stokes) approach. With this method only the mean flow is directly simulated, while the fluctuations are taken into account through the Reynolds stress tensor. This term introduces 6 new unknowns, and thus, some closure models, in our case the  $k$ - $\epsilon$  model (see Section 2.2.1), have to be introduced to close the problem. This method leads to widely reduced computational requirements, and this represents a big advantage in comparison with DNS, but it encounters accuracy problems if separated flows or recirculation bubbles have to be simulated. An intermediate approach between DNS and RANS is represented by Large-Eddy Simulation (LES), described in details in Section 2.3. It consists in filtering the Navier-Stokes equations, simulating only the flow scales larger than the filter width and modeling the small eliminated scales with appropriate models, in our case the Smagorinsky model. Computationally, LES is less demanding than DNS, but is much more expensive than RANS. The main advantage of LES in comparison with RANS is the capability of giving more accurate results for complex three-dimensional and time depending problems. The main drawback of the LES approach is represented by the still high computational cost. To have accurate results, indeed, fine meshes are required, especially near solid walls and the mesh resolution requirements increase with the Reynolds number. In order to reduce the needed computational resources, hybrid RANS/LES approaches have been developed. One of these is based on Limited Numerical Scales (LNS), described in detail in Section 2.4, which combines RANS and LES in a single model. The basic idea is to solve the LES equations where the mesh is fine enough to give good results and RANS equations otherwise. In practice, a blending criterion between LES and RANS is used, which is based on the values of the corresponding eddy-viscosities.

---

<sup>1</sup><http://www.recherche.gouv.fr/recherche/aci/grid.htm>

These approaches to turbulence are implemented in a numerical solver of 3D compressible flows, named AERO, which was developed by INRIA (France) and University Colorado at Boulder (USA). It uses a mixed finite-element and finite-volume formulation for the spatial discretization on unstructured meshes made of tetrahedra; both implicit or explicit time advancing are available for the temporal discretization and it is parallelized using MPI.

As we have already pointed out, another goal of this work is to test the performance of Grid Computing within the MecaGRID project. Grid Computing extends older concepts of distributed computing, such as the classical parallel computing, but in contrast with older systems, Grid Computing makes easier the allocation of needs to resources. Information from the different sites, where the computers are located, are exchanged using the web (Internet). The global inter-communications are, indeed, slower than the local inter-communications which use the local net. The main advantage of Grid Computing is the possibility of using computers located in different sites and in this way to be able to use a large number of processors which otherwise will be only partially exploited.

To validate the LES and the hybrid LNS models, a rounded jet issuing normally into a cross-flow, also known as jet in cross-flow configuration(JICF), has been simulated. This configuration has several practical applications because of its ability to mix rapidly with cross-flow and to introduce a controlled jet forced into the flow-field (i.e. injectors for cooling systems, exhaust of vehicles). It is interesting also from the basic research point of view because it is characterized by several vortical structures of different kind and dimension. Simulations are performed for a jet to cross-flow velocity ratio  $R = 2$  and for a Reynolds number  $Re = 82000$ , based on the cross-flow velocity and the diameter of the pipe.  $R = 2$  has been chosen because, for this velocity ratio value, the jet is able to push through the boundary layer of the cross-flow, thus the vortical structures form after the jet. The choice of  $Re = 82000$  is due to the presence of detailed experimental results carried out for this couple of parameters ( $R = 2$  and  $Re = 82000$ ) by Andreopoulos at al., Ref. [24]. The presence of both separated and non-separated flow regions is interesting for validate both LES and LNS models.

For Grid Computing, this test case is also of interest. In particular, the area where the interface between the pipe and the cross-flow is located is quite small. Thus, if the information is exchanged only for this zone, the number of communications is reduced and one of the main problems of Grid Computing, i.e. the communication between sites located in different places, is partially overcome.

## 2 Turbulent flows

### 2.1 Direct numerical simulation

The accurate description of turbulent flow phenomena and their prediction are matter of primary concern for the solution of many engineering problems. Due to the absence of a predictive theory valid for all the different turbulent flows, the simulation of these phenomena is one of the main problems in Computation Fluid Dynamics.

Turbulent flows are always unsteady and three-dimensional and can be represented by the Navier-Stokes equations. In the case of a compressible flow, if we consider a thermally and calorically perfect gas and if the body forces are absent or negligible, the flow is governed by the following equations, in which the Einstein notation is used :

$$\begin{aligned}
\frac{\partial \rho}{\partial t} + \frac{\partial(\rho u_j)}{\partial x_j} &= 0, \\
\frac{\partial(\rho u_i)}{\partial t} + \frac{\partial(\rho u_i u_j)}{\partial x_j} &= -\frac{\partial p}{\partial x_i} + \frac{\partial \sigma_{ij}}{\partial x_j}, \\
\frac{\partial(\rho E)}{\partial t} + \frac{\partial(\rho E u_j)}{\partial x_j} &= -\frac{\partial(p u_j)}{\partial x_j} + \frac{\partial(u_j \sigma_{ij})}{\partial x_i} - \frac{\partial q_j}{\partial x_j}, \\
p &= \rho R T, \\
E &= C_v T + \frac{1}{2} u_i u_i.
\end{aligned} \tag{1}$$

In the above equations density, temperature, pressure, total energy for unit mass and heat capacity at constant volume are represented respectively by  $\rho$ ,  $T$ ,  $p$ ,  $E$  and  $C_v$ . In the last equation  $R$  is equal to  $R/m$  where  $R$  is the universal constant of perfect gas and  $m$  is the moles mass. By assuming the flow Newtonian and under the Stokes hypothesis, the viscous stress tensor becomes:

$$\sigma_{ij} = -\frac{2}{3} \mu \frac{\partial u_k}{\partial x_k} \delta_{ij} + \mu \left( \frac{\partial u_i}{\partial x_j} + \frac{\partial u_j}{\partial x_i} \right) \tag{2}$$

where the viscosity coefficient  $\mu$  is, generally, a function of the temperature. Moreover, the Fourier law is adopted to model the heat flux:

$$q_i = K \frac{\partial T}{\partial x_i} \tag{3}$$

where  $K$  is the conduction coefficient for the gas and is generally a function of the temperature. The system of equations above quoted can be numerically integrated for every turbulent flow if fine enough spatial and temporal resolutions are used. Because of the nonlinearities of the equation system, the problem is characterized by a large range of spatial and temporal turbulent scales which scales with the Reynolds number. These scales take their kinetic turbulent energy from the mean unsteady flow and transfer it to smaller and smaller scales, as predict by the "Energy Cascade" concept. For this reason in all turbulent flows a continuum spectrum of energy is present. A typical distribution of energy is described in Fig. 1 as function of the wave-number,  $n$ , that is inversely proportional to the spatial scale.

Fig. 1 gives information about the mean-energy of the turbulent structures which have the same dimensions. The energetic structures can be split in the following ranges:

- *energy-containing range*, which contains the largest vortical turbulent structures

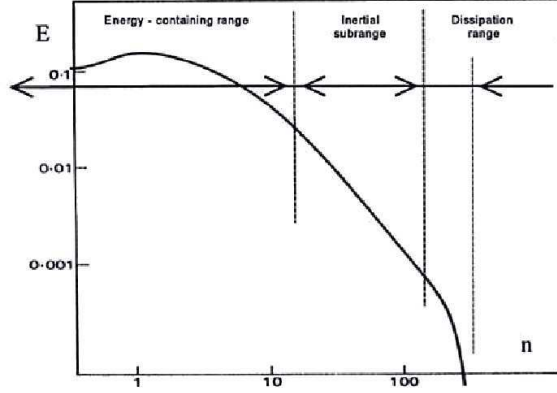


Figure 1: Typical energy spectrum of a turbulent boundary layer

- *inertial range* or *subrange*, which contains vortices of intermediate dimensions
- *dissipation range*, which contains the smallest structures.

To estimate the characteristic time and the characteristic dimensions of turbulence, the results of the *Universal Equilibrium Theory* of Kolmogorov Ref. [3] can be used. The spatial orders of magnitude of the largest scales,  $L$ , and of the smallest scale in the flow,  $l_k$ , are related as follows:

$$\frac{L}{l_k} = Re^{3/4} \quad (4)$$

where  $Re = \frac{UL}{\nu}$  is the Reynolds number of the flow, based on  $L$  and on an integral velocity, which can be assumed similar to the velocity of the largest scales. It can be seen that the separation between large and small scales increases with the Reynolds number. The largest scales of turbulence carry most of the turbulence kinetic energy so they are responsible of the turbulent transport. The smallest scales are responsible of most of the dissipation of kinetic energy, so even if their contribution to the kinetic energy is negligible in comparison with the largest scales they must be considered to obtain accurate results. To this purpose, the single computational cell must have the dimensions of the smallest turbulent scales and the computational domain must have the dimensions of the largest turbulence scales. Thus, the number of nodes,  $N$ , in the whole domain increases with the Reynolds number as follows:

$$N = Re^{9/4} . \quad (5)$$

With the increase of the Reynolds number, strong limitations for numerical simulation also occur due to the time resolution requirements. The governing equations, indeed, must

be advanced for a global time interval,  $\Delta T_c$ , of the order of the largest temporal scales,  $T_c$ , and the temporal step must be small enough to capture all the small temporal scales, of the order of  $t_k$ . The ratio between the largest and the smallest temporal scale is the following:

$$\frac{T_c}{t_k} = Re^{1/2} \quad (6)$$

so if the global step is constant the number of temporal steps needed to cover all the range  $\Delta T_c$  rise quickly with the increase of the Reynolds number.

The huge computational resources needed to directly simulate turbulent flows at high Reynolds numbers are not affordable. For this reason, the direct numerical simulation (DNS) is only used for low Reynolds number and simple geometries. On the other hand the information which can be obtained in DNS, is much larger than what is required in industrial or engineering problems. Due to this, other simplified models were developed in order to obtain the required information at a significantly reduced computational cost. Reynolds Averaged Navier-Stokes (RANS), Large Eddy Simulation (LES) and Limited Numerical Scales (LNS) are examples of these models.

It is important to stress that, unlike LES, RANS and LNS, DNS gives results that are free of errors due to empirical assumptions about intrinsic turbulent physics and produces information about turbulence useful to devise and validate turbulent models for the closure of RANS and LES. Thus, DNS plays an important role for the industrial numerical simulation, although indirect.

## 2.2 Reynolds-Averaged Navier-Stokes Equations

In order to avoid the use of DNS and thus to avoid the solution of the complete system of Eqs. 1, the first alternative model proposed was based on statistical approach and is known as Reynolds Averaged Navier-Stokes model (RANS). This method was introduced by Reynolds and is based on the idea that the characteristic times of the averaged flow are much longer than those of the turbulent structures. Thus, too small integration steps are not needed to resolve the mean flow and, if only the averaged flow is considered, the spatial discretization should capture only the gradients of the average motion. The unknown quantities of the problem are the flow statistical quantities and only the mean flow is simulated where "mean" usually stands for the time-averaged flow. The equations governing the flow statistical quantity are obtained by applying appropriate averaging, often time average, to the Navier-Stokes equations. If averaging is carried, each variable of the problem can be decomposed as follows:

$$x = \bar{x} + x' \quad (7)$$

where  $\bar{x}$  and  $x'$  stand for the mean value and the fluctuating part of the generic quantity, respectively. If we substitute the decomposition (7) in the Navier-Stokes equations and we apply the time-average we obtain, for an incompressible flow, the following classical set of RANS equations for the mean flow, where the Einstein notation is used:

$$\begin{aligned}\frac{\partial \bar{u}_j}{\partial x_j} &= 0, \\ \frac{\partial \bar{u}_i}{\partial t} + \frac{\partial(\rho \bar{u}_i \bar{u}_j)}{\partial x_j} &= -\frac{1}{\rho} \frac{\partial \bar{p}}{\partial x_i} + \nu \frac{\partial^2 \bar{u}_i}{\partial x_i \partial x_j} - \frac{\partial}{\partial x_j} (\rho \overline{u'_i u'_j}) .\end{aligned}\quad (8)$$

The equations for the averaged motion of a turbulent, Newtonian, incompressible flow are formally identical to the Navier-Stokes equations with a new term that is made by the averaged products of the velocity fluctuations. Those terms have the dimensions of a shear per unit of density and can be collected in a symmetrical tensor, known as Reynolds stress tensor, which represents the effects of fluctuations on the mean flow; its components are as follows:

$$R_{ij}^{(t)} = -\overline{\rho u'_i u'_j} . \quad (9)$$

In order to close the problem, the Reynolds stress tensor must be modeled as a function of the mean flow. The number of existing models is huge and their complexity is variable. Due to the conceptual difficulty in modeling the Reynolds stress tensor, it is accepted that it is impossible to find a model of general validity. Moreover there are class of flows, i.e. flows with massive separations or dominated by unsteady phenomena, for which the RANS models are not accurate enough and may be significantly sensitive to the boundary conditions imposed for the turbulent quantities, which are sometimes difficult to be assigned.

### 2.2.1 Standard $k$ - $\epsilon$ model

The standard  $k$ - $\epsilon$  model, proposed by Jones and Launder, Ref. [5], belongs to the class of the eddy viscosity models. In this models the following constitutive equation is applied, in analogy with the modeling equation for the viscous stress tensor in Newtonian fluids:

$$R_{ij} = \mu_t \bar{P}_{ij} - \frac{2}{3} \bar{\rho} k \delta_{ij} = \mu_t \left[ \frac{\partial \bar{u}_i}{\partial x_j} + \frac{\partial \bar{u}_j}{\partial x_i} - \frac{2}{3} \partial \bar{u}_l x_l \delta_{ij} \right] \quad (10)$$

where  $\mu_t$  is the turbulent eddy viscosity and  $\delta_{ij}$  is the Kronecker symbol. Using the Eq. (10), the closure of the model is reduced to assign the eddy viscosity  $\mu_t$  as a function of the averaged flow field. In the  $k$ - $\epsilon$  model the eddy viscosity,  $\mu_t$ , is defined as follows:

$$\mu_t = C_\mu \frac{k^2}{\epsilon} \quad (11)$$

where  $C_\mu$  is a free constant usually equal to 0.09,  $k = \overline{u'_j u'_j}$  is the turbulent kinetic energy and  $\epsilon = 2\nu \overline{\frac{\partial u'_i}{\partial x_j} \frac{\partial u'_i}{\partial x_j}}$  is the turbulent dissipation rate. The spatial distribution of  $k$  and  $\epsilon$  is estimated by solving the following transport equation:

$$\begin{aligned}
\rho \frac{\partial k}{\partial t} + \rho \bar{u}_j \frac{\partial k}{\partial x_j} &= R_{ij} \frac{\partial \bar{u}_i}{\partial x_j} - \rho \epsilon + \frac{\partial}{\partial x_j} \left[ \left( \mu + \frac{\mu_t}{\sigma_k} \right) \frac{\partial \epsilon}{\partial x_j} \right], \\
\rho \frac{\partial \epsilon}{\partial t} + \rho \bar{u}_j \frac{\partial \epsilon}{\partial x_j} &= C_{\epsilon 1} \frac{\epsilon}{k} R_{ij} \frac{\partial \bar{u}_i}{\partial x_j} - C_{\epsilon 2} \rho \frac{\epsilon^2}{k} + \frac{\partial}{\partial x_j} \left[ \left( \mu + \frac{\mu_t}{\sigma_\epsilon} \right) \frac{\partial \epsilon}{\partial x_j} \right]
\end{aligned} \tag{12}$$

where  $C_{\epsilon 1}$ ,  $C_{\epsilon 2}$ ,  $\sigma_k$  and  $\sigma_\epsilon$  are the model parameters and usually are set as follow:

$$C_{\epsilon 1} = 1.44 \quad C_{\epsilon 2} = 1.92 \quad \sigma_k = 1.0 \quad \sigma_\epsilon = 1.3 .$$

## 2.3 Large Eddy Simulation

The large-eddy simulation approach (LES) is intermediate between DNS, where all fluctuations are resolved, and the statistical simulations based on RANS, where only the mean flow is resolved. In LES the severe Reynolds number restrictions of DNS are bypassed by directly simulating the large scales (GS) only and supplying the effect of the missing small scales (SGS) by a so-called sub-grid model. This is obtained by filtering the Navier-Stokes equations in space, in order to eliminate the flow fluctuations smaller than the filter size. In this way, the new unknowns of the problem become the filtered flow variables. Like for RANS, due to the non-linearity of the original problem, the new equations contain additional unknown terms, the so-called sub-grid scale (SGS) terms, representing the effect of the eliminated small scales on the filtered equations. In order to close the problem, these terms must be modeled, but, due to the fact that the small unresolved scales are often simpler in nature than the inhomogeneous large motions, since they do not significantly depend on the large scale motion, rather simple closure models may work well for many applications. Another advantage of this method is the possibility of directly simulating the largest scales, which are usually more interesting from the engineering point of view. Computationally, LES clearly is less demanding than DNS, but in general much more expensive than RANS. The reason is that, independent by the problem to be solved, LES always requires fully three-dimensional and time-dependent calculations even for flows which are two- or one-dimensional in the mean. Moreover LES, like DNS, needs to be carried out for long periods of time to obtain stable and significant statistics. For these reasons, LES should provide best results for the analysis of complex three-dimensional and time-dependent problems where RANS frequently fails. The utilization of LES for engineering problem is not yet very extensive, but in recent years the interest in this method has largely increased.

### 2.3.1 SGS modeling

The energy-carrying large scales structures (GS) mainly contribute for the turbulent transport and the dissipative small scale motions (SGS) carry most of the vorticity and act as a sink of turbulent kinetic energy. For high Reynolds numbers the dissipative part of the spectrum becomes clearly separated from the low wave-number range, in a way shown by

GS turbulence	SGS turbulence
Produced by mean flow	Produced by larger eddies
Depends on boundaries	Universal
Ordered	Chaotic
Requires deterministic description	Can be modeled statistically
Inhomogeneous	Homogeneous
Anisotropic	Isotropic
Long-lived	Short-lived
Diffusive	Dissipative
Difficult to model	Easier to model

Table 1: Qualitative differences between GS turbulence and SGS turbulence

Eq. (4). Some of the significant differences between GS and SGS scales are summarized in Tab. 1, Ref. [2].

To illustrate the role of SGS models, it is useful to consider possible consequences if turbulent simulation are performed with insufficient resolution. In this case the viscous dissipation in the flow cannot properly be accounted for. This will typically result in an accumulation of energy at the high wave-number end of the spectrum which reflect a distorted equilibrium state between production and dissipation of turbulent kinetic energy. For sufficiently high Reynolds numbers (or sufficiently coarse grids) the discrete representation of the flow even becomes essentially inviscid and the non-linear transfer of energy can lead to an unbounded growth of turbulence intensities and eventually to numerical instability of the computation.

### 2.3.2 Filtered equations of the motion

In LES any dependent variable of the flow,  $f$ , is split into a GS part,  $\bar{f}$ , and a SGS part,  $f'$ :

$$f = \bar{f} + f' . \quad (13)$$

Generally, the GS component,  $\bar{f}$ , represents that part of the turbulent fluctuation which remains after some smoothing which has been applied to the flow field.

When a compressible flow is considered, it is convenient define a density weighted filter since it allows to partially recover the formal structure of the equations of the incompressible case. This filter is defined as follows:

$$\tilde{f} = \frac{\overline{\rho f}}{\bar{\rho}} . \quad (14)$$

An appropriate filtering operation must be chosen to separate GS from SGS. Applying the filtering operation to the Navier-Stokes equations, Eq. (1), yields the equations of motion



of the GS flow field. Like in RANS the filtering of the non linearities is of particular interest since it gives rise to additional unknowns terms. For LES of compressible flows, the filtered form of the equations of motion for a thermally and calorically perfect gas is the following:

$$\begin{aligned}
 \frac{\partial \bar{\rho}}{\partial t} + \frac{\partial(\bar{\rho} \tilde{u}_j)}{\partial x_j} &= 0 \\
 \frac{\partial(\bar{\rho} \tilde{u}_i)}{\partial t} + \frac{\partial(\bar{\rho} \tilde{u}_i \tilde{u}_j)}{\partial x_j} &= -\frac{\partial \bar{p}}{\partial x_i} + \frac{\partial(\mu \tilde{P}_{ij})}{\partial x_j} - \frac{\partial M_{ij}^{(1)}}{\partial x_j} + \frac{\partial M_{ij}^{(2)}}{\partial x_j} \\
 \frac{\partial(\bar{\rho} \tilde{E})}{\partial t} + \frac{\partial[(\bar{\rho} \tilde{E} + \bar{p}) \tilde{u}_j]}{\partial x_j} &= \frac{\partial(\tilde{u}_j \tilde{\sigma}_{ij})}{\partial x_i} - \frac{\partial \tilde{q}_j}{\partial x_j} + \frac{\partial}{\partial x_j} (Q_j^{(1)} + Q_j^{(2)} + Q_j^{(3)})
 \end{aligned} \tag{15}$$

In the momentum equation the sub-grid terms are represented by the terms  $M_{ij}^{(i)}$  which can be defined as follows:

$$M_{ij}^{(1)} = \overline{\rho u_i u_j} - \bar{\rho} \tilde{u}_i \tilde{u}_j \tag{16}$$

$$M_{ij}^{(2)} = \overline{\mu P_{ij}} - \mu \tilde{P}_{ij} \tag{17}$$

and

$$P_{ij} = -\frac{2}{3} S_{kk} \delta_{ij} + 2 S_{ij} \tag{18}$$

where  $S_{ij}$  is the strain rate tensor defines as:

$$S_{ij} = \frac{1}{2} \left( \frac{\partial u_i}{\partial x_j} + \frac{\partial u_j}{\partial x_i} \right). \tag{19}$$

$M_{ij}^{(1)}$  takes into account the momentum transport of the sub-grid scales and  $M_{ij}^{(2)}$  represents the transport of viscosity due to the sub-grid scales fluctuations.

In the energy equation the sub-grid term are represented by the terms  $Q_j^{(i)}$  which can be defined as follows:

$$Q_j^{(1)} = \left[ \tilde{u}_i (\bar{\rho} \tilde{E} + \bar{p}) - \overline{u_i (\rho E + p)} \right] \tag{20}$$

$$Q_j^{(2)} = \overline{(\mu P_{ij} u_j)} - (\mu \tilde{P}_{ij} \tilde{u}_j) \tag{21}$$

$$Q_j^{(3)} = K \frac{\partial \tilde{T}}{\partial x_j} - K \frac{\partial \tilde{T}}{\partial x_j} \tag{22}$$

$Q_j^{(1)}$  represents three distinct physical effects:

- the transport of energy  $E$  due to small scale fluctuations;
- the change of the internal energy due to the sub-grid scale compressibility  $\left(p \frac{\partial u_j}{\partial s_j}\right)$ ;
- the dissipation of energy due to sub-grid-scale motions in the pressure field  $\left(u_j \frac{\partial p}{\partial x_j}\right)$ ;

$Q_j^{(2)}$  takes in account the dissipative effect due to the sub-grid scale transport of viscosity;  $Q_j^{(3)}$  takes in account the heat transfer caused by the motion of the neglected sub-grid scales.

### 2.3.3 Smagorinsky's model

The Smagorinsky model is an example of closure models. We assume that low compressibility effects are present in the SGS fluctuations and that heat transfer and temperature gradients are moderate. The retained SGS term in the momentum equation is thus the classical SGS stress tensor:

$$M_{ij} = \rho \overline{u_i u_j} - \bar{\rho} \tilde{u}_i \tilde{u}_j \quad (23)$$

where the over-line denotes the grid filter and the tilde the density-weighted Favre filter ( $\tilde{f} = (\overline{\rho f})/\bar{\rho}$ ). The isotropic part of  $M_{ij}$  can be neglected under the assumption of low compressibility effect in the SGS fluctuations. The deviatoric part,  $T_{ij}$ , may be expressed by an eddy viscosity term, in accordance with the Smagorinsky model extended to compressible flow:

$$T_{ij} = -2\mu_{sgs} \left( \tilde{S}_{ij} - \frac{1}{3} \tilde{S}_{kk} \right), \quad (24)$$

$$\mu_{sgs} = \bar{\rho} C_s \Delta^2 |\tilde{S}|. \quad (25)$$

where  $\tilde{S}_{ij}$  is the resolved strain tensor,  $\mu_{sgs}$  is the SGS viscosity,  $\Delta$  is the filter width,  $C_s$  is a constant which must be assigned a priori and  $|\tilde{S}| = \sqrt{\tilde{S}_{ij} \tilde{S}_{ij}}$ . The width of the filter is defined for every grid elements,  $l$ , as follows:

$$\Delta^{(l)} = \max_{i=1,\dots,6} (\Delta^{(l_i)}) \quad (26)$$

where  $\Delta_i^{(l)}$  is the length of the  $i$ -th side of the  $l$ -th element, so  $\Delta^{(l)}$  is the length of the largest edge.

In the energy equation the effect of the SGS fluctuations has been modified by the introduction of a constant SGS Prandtl number to be assigned a priori:

$$Pr_{sgs} = C_p \frac{\mu_{sgs}}{K_{sgs}} \quad (27)$$

where  $K_{sgs}$  is the SGS conductivity coefficient and it takes into account the diffusion of total energy caused by the SGS fluctuation. In the filtered energy equation, the term  $K_{sgs}$  is added to the molecular conductivity coefficient.

Another limit for LES is due to the assumption frequently done in SGS models of taking the cut-off of the filter in the inertial range, so very high computational requirements are needed.

### 2.3.4 Resolution requirements for LES

The SGS effects in a turbulent flow depend qualitatively and quantitatively on the width of the filter function applied. Generally the filter width should be as large as possible in order to minimize the computational needs of a simulation, but larger filter width gives rise to a more complex SGS turbulence. For this reason a compromise should be found.

### 2.3.5 Boundary conditions

LES simulation are generally significantly costly as regards both CPU and memory requirements, especially when high Reynolds numbers and solid walls are simulated. The grid refinement required in the near wall region has severely slowed the development of LES for flows of practical interest. For this reason several ways to treat the boundary conditions are introduced. The proposed approaches to do this can be divided in two classes:

- *near wall resolution method,*
- *near wall modeling method.*

The near wall resolution method was the first method to be used and consists in decreasing the filter width to zero at the boundaries. In this way the important flow features near the boundary are captured, but this method has high computational cost since it requires a very fine mesh near the walls. The near wall modeling method, instead, group together all the techniques aimed at keeping the grid coarse in the near wall region to reduce the computational cost. In particular those models can be classified in:

- *wall law methods,*
- *two-layer approaches.*

The wall-law methods use algebraic functions (wall-law) to reconstruct the velocity profile near the wall where the fluid resolution is poor. The methods of this class differ in the type of wall-law used and in the way in which the wall-law is employed to provided an approximate set of boundary conditions.

The two-layer approach, instead, consists in resolving a set of equations in the near-wall region derived from Navier-Stokes equations for turbulent attached boundary conditions. These methods can differ in the set of simplified solved equations.

## 2.4 Limited Numerical Scales

While LES is an increasingly powerful tool for unsteady turbulent flow prediction, it is still prohibitively expensive. To bring LES closer to becoming a design tool, hybrid RANS/LES approaches have been developed. One of these is based on Limited Numerical Scales (LNS) which combines RANS and LES in a single modeling framework. This approach has the advantage of being particularly easy to implement in existing codes. In LNS the Reynolds tensor is modeled by an eddy-viscosity which is obtained by taking the minimum value between the ones given respectively by RANS  $k$ - $\epsilon$  model and by the LES Smagorinsky model. This allows the LES approach to be used where the grid resolution is adequate for resolving the largest turbulence scales, while the RANS approach is used where the grid is not sufficiently refined. This model, as all the hybrid models, is mainly based on empiricism. Since very few applications of LNS are presented in the literature, it lacks validation to be reliably used in industry.

We can assume to use the  $k$ - $\epsilon$ , see Section 2.2.1, for the closure of the RANS equations, in which the Reynolds stress tensor is modeled as shown in Eq. 10. Thus, the LNS equations are obtained from the RANS ones by replacing the Reynolds stress tensor,  $R_{ij}$ , with the  $L_{ij}$  tensor which is equal to  $R_{ij}$  multiplied by a *blending function*,  $\alpha$ :

$$L_{ij} = \alpha R_{ij} \quad (28)$$

The blending function  $\alpha$  varies in space and time and in the LNS model proposed by Batten, Ref. [6], is defined as follows:

$$\alpha = \min \left\{ \frac{\mu_s}{\mu_t}, 1 \right\} \quad (29)$$

where  $\mu_s$  is the SGS viscosity obtained from LES closures and  $\mu_t$  is the turbulent viscosity obtained from RANS closures. If the Smagorinsky model is adopted the SGS viscosity is defined as follows, see Section 2.3.3:

$$\mu_s = \bar{\rho} C_s \Delta^2 \sqrt{\tilde{S}_{ij} \tilde{S}_{ij}} \quad (30)$$

The set of LNS equations is the follows:

$$\begin{aligned} \frac{\partial \bar{\rho}}{\partial t} + \frac{\partial(\bar{\rho} \tilde{u}_i)}{\partial x_i} &= 0, \\ \frac{\partial(\bar{\rho} \tilde{u}_i)}{\partial t} + \frac{\partial(\bar{\rho} \tilde{u}_i \tilde{u}_j)}{\partial x_j} &= -\frac{\partial \bar{p}}{\partial x_i} + \frac{\partial(\tilde{\sigma}_{ij} + L_{ij})}{\partial x_j}, \\ \frac{\partial \bar{E}}{\partial t} + \frac{\partial \tilde{u}_j (\bar{E} + \bar{p})}{\partial x_j} &= \frac{\partial \tilde{u}_i \tilde{\sigma}_{ij}}{\partial x_j} + \frac{\partial \tilde{u}_i L_{ij}}{\partial x_j} + \frac{\partial}{\partial x_j} \frac{\alpha \mu_t}{\sigma_k} \frac{\partial k}{\partial x_j} + \\ &\quad \frac{\partial}{\partial x_j} \left( \frac{C_p}{Pr} (\mu + \alpha \mu_t) \frac{\partial \tilde{T}}{\partial x_j} \right) \end{aligned}$$

$$\begin{aligned}
\frac{\partial(\bar{\rho}k)}{\partial t} + \frac{\partial\bar{\rho}\tilde{u}_j k}{\partial x_j} &= \frac{\partial}{\partial x_j} \left[ \left( \mu + \frac{\alpha\mu_t}{\sigma_k} \right) \frac{\partial k}{\partial x_j} \right] + L_{ij} \frac{\partial\tilde{u}_i}{\partial x_j} - \bar{\rho}\epsilon, \\
\frac{\partial\bar{\rho}\epsilon}{\partial t} + \frac{\partial\bar{\rho}\epsilon\tilde{u}_j}{\partial x_j} &= \frac{\partial}{\partial x_j} \left[ \left( \mu + \frac{\alpha\mu_t}{\sigma_\epsilon} \right) \frac{\partial\epsilon}{\partial x_j} \right] + C_{\epsilon 1} \left( \frac{\epsilon}{k} \right) L_{ij} \frac{\partial\tilde{u}_i}{\partial x_j} - C_{\epsilon 2} \bar{\rho} \frac{\epsilon^2}{k}. \quad (31)
\end{aligned}$$

### 3 AERO code

In this section the main features of the numerical method are described.

#### 3.1 Set of governing equations

In the AERO code the Navier Stokes equations are numerically normalized with the following reference quantities:

- $L_{ref} \Rightarrow$  characteristic length of the flow,
- $U_{ref} \Rightarrow$  velocity of the free-stream flow,
- $\rho_{ref} \Rightarrow$  density of the free-stream flow,
- $\mu_{ref} \Rightarrow$  molecular viscosity of the free-stream flow.

The flow variables can be normalized with the reference quantities as follows:

$$\begin{aligned}
\rho^* &= \frac{\rho}{\rho_{ref}} & u_j^* &= \frac{u_j}{U_{ref}} & p^* &= \frac{p}{U_{ref} p_{ref}} \\
E^* &= \frac{E}{\rho_{ref} U_{ref}^2} & \mu^* &= \frac{\mu}{\mu_{ref}} & t^* &= t \frac{L_{ref}}{U_{ref}}. \quad (32)
\end{aligned}$$

The non-dimensional form of the Navier Stokes equations can be obtained substituting the reference quantities Eq. (32) in the set of equations described in Eq. (1) and is quoted in the following:

$$\begin{aligned}
\frac{\partial\rho^*}{\partial t^*} + \frac{\partial(\rho^* u_j^*)}{\partial x_j^*} &= 0 \\
\frac{\partial(\rho^* u_i^*)}{\partial t^*} + \frac{\partial(\rho^* u_i^* u_j^*)}{\partial x_j^*} &= -\frac{\partial p^*}{\partial x_i^*} + \frac{1}{Re} \frac{\partial\sigma_{ij}^*}{\partial x_j^*} \\
\frac{\partial(\rho^* E^*)}{\partial t^*} + \frac{\partial(\rho^* E^* u_j^*)}{\partial x_j^*} &= -\frac{\partial(p^* u_j^*)}{\partial x_j^*} + \frac{1}{Re} \frac{\partial(u_j^* \sigma_{ij}^*)}{\partial x_i^*} - \frac{\gamma}{Re Pr} \frac{\partial}{\partial x_j^*} \left[ \mu^* \left( E^* - \frac{1}{2} u_j^* u_j^* \right) \right] \quad (33)
\end{aligned}$$

where the Reynolds number,  $Re = U_{ref} L_{ref} / \nu$ , is based on the references quantities,  $U_{ref}$  and  $L_{ref}$ , the Prandlt number,  $Pr$ , can be assumed constant for a gas and equal to:

$$Pr = \frac{C_p \mu}{k} \quad (34)$$

and  $\gamma = C_p / C_v$  is the ratio between the specific heats at constant pressure and volume. Also the constitutive equations for the viscous stresses and the state equations may be written in non-dimensional form as follows:

$$\begin{aligned} \sigma_{ij}^* &= -\frac{2}{3} \mu^* \left( \frac{\partial u_k^*}{\partial x_k^*} \delta_{ij} \right) + \mu^* \left( \frac{\partial u_i^*}{\partial x_j^*} + \frac{\partial u_j^*}{\partial x_i^*} \right) \\ p^* &= (\gamma - 1) \rho^* \left( E^* - \frac{1}{2} u_j^* u_j^* \right). \end{aligned} \quad (35)$$

In order to rewrite the governing equations in a compact form more suitable for the discrete formulation, we group together the unknown variables in the  $W$  vector:

$$W = (\rho, \rho u, \rho v, \rho w, \rho E)^T.$$

If we define the two vectors,  $F$  and  $V$  as function of  $W$ , as follows:

$$F = \begin{pmatrix} \rho u & \rho v & \rho w \\ \rho u^2 + p & \rho uv & \rho uw \\ \rho uv & \rho v^2 + p & \rho vw \\ \rho uw & \rho vw & \rho w^2 + p \end{pmatrix}$$

and

$$V = \begin{pmatrix} 0 & 0 & 0 \\ \sigma_{xx} & \sigma_{yx} & \sigma_{zx} \\ \sigma_{xy} & \sigma_{yy} & \sigma_{zy} \\ \sigma_{xz} & \sigma_{yz} & \sigma_{zz} \\ u\sigma_{xx} + v\sigma_{xy} + w\sigma_{xz} - q_x & u\sigma_{xy} + v\sigma_{yy} + w\sigma_{yz} - q_y & u\sigma_{xz} + v\sigma_{yz} + w\sigma_{zz} - q_z \end{pmatrix}$$

and if we substitute the vectors  $V$  and  $F$  in (33), it is possible to rewrite the governing equations in the following compact format, which is the starting point for the derivation of the Galerkin formulation and of the discretization of the problem:

$$\frac{\partial W}{\partial t} + \frac{\partial}{\partial x_j} F_j(W) - \frac{1}{Re} \frac{\partial}{\partial x_j} V_j(W, \nabla W) = 0. \quad (36)$$

One can note that the vectors  $F$  and  $V$  are respectively the convective fluxes and the diffusive fluxes.

### 3.2 Space discretization

Spatial discretization is based on a mixed finite-volume/finite-element formulation. A finite volume upwind formulation is used for the treatment of the convective fluxes while a classical

Galerkin finite-element centered approximation is employed for the diffusive terms . The computational domain  $\Omega$  is approximated by a polygonal domain  $\Omega_h$ . This polygonal domain is then divided in  $N_t$  tetrahedral elements  $T_i$  by a standard finite-element triangulation process:

$$\Omega_h = \bigcup_{i=1}^{N_t} T_i. \quad (37)$$

The set of elements  $T_i$  forms the grid used in the finite-element formulation. The dual finite-volume grid is built starting from the triangulation by the method of the medians. A finite-volume cell is constructed around each node  $a_i$  of the triangulation, dividing in 4 sub-tetrahedra every tetrahedron having  $a_i$  as a vertex by means of the median planes. We will call  $C_i$  the union of the resulting sub-tetrahedra having  $a_i$  as a vertex and they have the following property:

$$\Omega_h = \bigcup_{i=1}^{N_c} C_i. \quad (38)$$

where  $N_c$  is the number of cells, which is equal to the number of the nodes of the triangulation.

### 3.2.1 Convective fluxes

If we indicate the basis functions for the finite-volume formulation as follows:

$$\psi^{(i)}(P) = \begin{cases} 1 & \text{if } P \in C_i \\ 0 & \text{otherwise} \end{cases}$$

the Galerkin formulation for the convective fluxes is obtained multiplying the convective terms of (36) by the basis function  $\psi^{(i)}$ , integrating on the domain  $\Omega_h$  and using the divergence theorem. In this way we obtain:

$$\iint_{\Omega_h} \left( \frac{\partial F_j}{\partial x_j} \right) \psi^{(i)} dx dy = \iint_{C_i} \frac{\partial F_j}{\partial x_j} d\Omega = \int_{\partial C_i} F_j n_j d\sigma$$

where  $d\Omega$ ,  $d\sigma$  and  $n_j$  are the elementary measure of the cell, of its boundary and the  $j$ th component of the normal external to the cell  $C_i$  respectively.

The total contribution to the convective fluxes is:

$$\sum_j \int_{\partial C_{ij}} \mathcal{F}(W, \vec{n}) d\sigma$$

where  $\mathcal{F}(W, \vec{n}) = F_j(W)n_j$ ,  $\partial C_{ij}$  is the boundary between cells  $C_i$  and  $C_j$ , and  $\vec{n}$  is the outer normal to the cell  $C_i$ .

The basic component for the approximation of the convective fluxes is the Roe scheme, Ref. [18]:

$$\int_{\partial C_{ij}} \mathcal{F}(W, \vec{n}) d\sigma \simeq \Phi^R(W_i, W_j, \vec{\nu}_{ij})$$

where

$$\vec{\nu}_{ij} = \int_{\partial C_{ij}} \vec{n} d\sigma$$

and  $W_k$  is the solution vector at the  $k$ -th node of the discretization.

The numerical fluxes,  $\Phi^R$ , are evaluated as follows:

$$\Phi^R(W_i, W_j, \vec{\nu}_{ij}) = \underbrace{\frac{\mathcal{F}(W_i, \vec{\nu}_{ij}) + \mathcal{F}(W_j, \vec{\nu}_{ij})}{2}}_{\text{centered}} - \underbrace{\gamma_s d^R(W_i, W_j, \vec{\nu}_{ij})}_{\text{upwinding}}$$

where  $\gamma_s \in [0, 1]$  is a parameter which directly controls the upwinding of the scheme and

$$d^R(W_i, W_j, \vec{\nu}_{ij}) = \left| \mathcal{R}(W_i, W_j, \vec{\nu}_{ij}) \right| \frac{W_j - W_i}{2} . \quad (39)$$

$\mathcal{R}$  is the Roe matrix and is defined as:

$$\mathcal{R}(W_i, W_j, \vec{\nu}_{ij}) = \frac{\partial \mathcal{F}}{\partial W}(\widehat{W}, \nu_{ij}) \quad (40)$$

where  $\widehat{W}$  is the Roe average between  $W_i$  and  $W_j$ .

The classical Roe scheme is obtained as a particular case by imposing  $\gamma_s = 1$ . The accuracy of this scheme is only 1st order. In order to increase the order of accuracy of the scheme the MUSCL (*Monotone Upwind Schemes for Conservation Laws*) reconstruction method, introduced by Van Leer, Ref. [19], is employed. This method expresses the Roe flux as a function of the extrapolated values of  $W$  at the interface between the two cells  $C_i$  and  $C_j$ ,  $W_{ij}$  and  $W_{ji}$ :

$$\int_{\partial C_{ij}} \mathcal{F}(W, \vec{n}) d\sigma \simeq \Phi^R(W_{ij}, W_{ji}, \vec{\nu}_{ij})$$

where  $W_{ij}$  and  $W_{ji}$  are defined as follows:

$$W_{ij} = W_i + \frac{1}{2}(\vec{\nabla} W)_{ij} \cdot \vec{i}\vec{j} , \quad (41)$$

$$W_{ji} = W_j + \frac{1}{2}(\vec{\nabla} W)_{ji} \cdot \vec{i}\vec{j} . \quad (42)$$

To estimate the gradients  $(\vec{\nabla} W)_{ij} \cdot \vec{i}\vec{j}$  and  $(\vec{\nabla} W)_{ji} \cdot \vec{i}\vec{j}$  the V6 scheme is used, Ref. [4]:



$$\begin{aligned}
 (\vec{\nabla}W)_{ij} \cdot \vec{i}j &= (1-\beta)(\vec{\nabla}W)_{ij}^C \cdot \vec{i}j + \beta(\vec{\nabla}W)_{ij}^U \cdot \vec{i}j + \\
 &\quad \xi_c [(\vec{\nabla}W)_{ij}^U \cdot \vec{i}j - 2(\vec{\nabla}W)_{ij}^C \cdot \vec{i}j + (\vec{\nabla}W)_{ij}^D \cdot \vec{i}j] + \\
 &\quad \xi_c [(\vec{\nabla}W)_M \cdot \vec{i}j - 2(\vec{\nabla}W)_i \cdot \vec{i}j + (\vec{\nabla}W)_j \cdot \vec{i}j] , \quad (43)
 \end{aligned}$$

$$\begin{aligned}
 (\vec{\nabla}W)_{ji} \cdot \vec{j}i &= (1-\beta)(\vec{\nabla}W)_{ji}^C \cdot \vec{j}i + \beta(\vec{\nabla}W)_{ji}^U \cdot \vec{j}i + \\
 &\quad \xi_c [(\vec{\nabla}W)_{ji}^U \cdot \vec{j}i - 2(\vec{\nabla}W)_{ji}^C \cdot \vec{j}i + (\vec{\nabla}W)_{ji}^D \cdot \vec{j}i] + \\
 &\quad \xi_c [(\vec{\nabla}W)_{M'} \cdot \vec{j}i - 2(\vec{\nabla}W)_i \cdot \vec{j}i + (\vec{\nabla}W)_j \cdot \vec{j}i] , \quad (44)
 \end{aligned}$$

where  $(\vec{\nabla}W)_i$  and  $(\vec{\nabla}W)_j$  are the nodal gradients at the nodes  $i$  and  $j$  respectively and are calculated as the average of the gradient on the tetrahedra  $T \in C_i$ , having the node  $i$  as a vertex. For example for  $(\vec{\nabla}W)_i$  we can write:

$$(\vec{\nabla}W)_i = \frac{1}{Vol(C_i)} \sum_{T \in C_i} \frac{Vol(T)}{3} \sum_{k \in T} W_k \vec{\nabla} \Phi^{i,T} . \quad (45)$$

$(\vec{\nabla}W)_M \cdot \vec{i}j$ , for the 3D case, is the gradient at the point  $M$  and it is computed by interpolation of the nodal gradient values at the nodes contained in the face opposite to the upwind tetrahedron  $T_{ij}$ .  $(\vec{\nabla}W)_{M'} \cdot \vec{i}j$  is the gradient at the point  $M'$  and it is evaluated in the same way as  $(\vec{\nabla}W)_M \cdot \vec{i}j$ . The coefficients  $\beta$ ,  $\xi_c$ ,  $\xi_d$  are parameters that control the combination of fully upwind and centered slopes. The V6 scheme is obtained by choosing them to have the best accuracy on Cartesian meshes, Ref.[4]:

$$\beta = 1/3, \quad \xi_c = 1/30, \quad \xi_d = -2/15 .$$

### 3.2.2 Diffusive fluxes

The P1 finite-element basis function,  $\phi^{(i,T)}$ , restricted to the tetrahedron  $T$  is assumed to be of unit value on the node  $i$  and to vanish at the remaining vertices of  $T$ . The Galerkin formulation for the diffusive terms is obtained by multiplying the diffusive terms by  $\phi^{(i,T)}$  and integrating over the domain  $\Omega_h$ :

$$\iint_{\Omega_h} \left( \frac{\partial V_j}{\partial x_j} \right) \phi^{(i,T)} d\Omega = \iint_T \frac{\partial V_j}{\partial x_j} \phi^{(i,T)} d\Omega .$$

Integrating by parts the right-hand side of Eq.(3.2.2) we obtain:

$$\begin{aligned}
 \iint_T \frac{\partial V_j}{\partial x_j} \phi^{(i,T)} d\Omega &= \iint_T \frac{\partial(V_j \phi^{(i,T)})}{\partial x_j} d\Omega - \iint_T V_j \frac{\partial \phi^{(i,T)}}{\partial x_j} d\Omega = \\
 &\quad \int_{\partial T} V_j \phi^{(i,T)} n_j d\sigma - \iint_T V_j \frac{\partial \phi^{(i,T)}}{\partial x_j} d\Omega . \quad (46)
 \end{aligned}$$

In order to build the fluxes for the node  $i$  consistently with the finite-volume formulation, the contribution of all the elements having  $i$  as a vertex needs to be summed together as follows:

$$\begin{aligned} & \sum_{T, i \in T} \left( \int_{\partial T} V_j \phi^{(i,T)} n_j d\sigma - \iint_T V_j \frac{\partial \phi^{(i,T)}}{\partial x_j} d\Omega \right) = \\ & - \sum_{T, i \in T} \iint_T V_j \frac{\partial \phi^{(i,T)}}{\partial x_j} d\Omega + \int_{\Gamma_h = \partial\Omega_h} \phi^{(i,T)} V_j n_j d\sigma . \end{aligned} \quad (47)$$

In the P1 formulation for the finite-element method, the test functions,  $\phi^{(i,T)}$ , are linear functions on the element  $T$  and so their gradient is constant. Moreover, in the variational formulation the unknown variables contained in  $W$  are also approximated by their projection on the P1 basis function. For these reasons the integral can be evaluated directly.

### 3.3 Boundary conditions

Firstly, the real boundary  $\Gamma$  is approximated by a polygonal boundary  $\Gamma_h$  that can be split in two parts:

$$\Gamma_h = \Gamma_\infty + \Gamma_b \quad (48)$$

where the term  $\Gamma_\infty$  represents the far-fields boundary and  $\Gamma_b$  represents the body surface. The boundary conditions are set using the formulation on  $\Gamma_\infty$  and using slip or no-slip conditions on  $\Gamma_b$ . In the AERO code a wall-law method is used to set the no-slip boundary conditions. To have an accurate description of both laminar and inertial sub-layers the Reichardt wall-law is used:

$$\frac{\bar{u}}{U_\tau} = \frac{1}{k} \ln(1 + kz^+) + 7.8 \left( 1 - e^{\frac{z^+}{11}} - \frac{z^+}{11} e^{-0.33z^+} \right). \quad (49)$$

The boundary conditions are introduced in a weak way, in fact they are introduced in the integrals over the domain boundaries that appear in the Galerkin formulation and are not forced directly on the solution vector at each time step.

### 3.4 Time advancing

Once the equations have been discretized in space, the unknown of the problem is the solution vector at each node of the discretization as a function of time,  $W_h(t)$ . Consequently the spatial discretization leads to a set of ordinary differential equations in time:

$$\frac{dW_h}{dt} + \Psi(W_h) = 0 \quad (50)$$

where  $\Psi_i$  is the total flux, concerning both convective and diffusive terms, of  $W_h$  through the  $i$ -th cell boundary divided by the volume of the cell.

### 3.4.1 Explicit time advancing

In the explicit case a  $N$ -step low-storage Runge-Kutta algorithm is used for the discretization of Eq.(50):

$$\begin{cases} W^{(0)} = W^{(n)}, \\ W^{(k)} = W^{(0)} + \Delta t \alpha_k \Psi(W^{(k-1)}), \quad k = 1, \dots, N \\ W^{(n+1)} = W^{(N)}. \end{cases}$$

in which the subscript  $h$  has been omitted for sake of simplicity. Different schemes can be obtained varying the number of steps,  $N$ , and the coefficients  $\alpha_k$ .

### 3.4.2 Implicit time advancing

For the implicit time advancing scheme in AERO is used the following second-order accurate backward difference scheme is used:

$$\alpha_{n+1}W^{(n+1)} + \alpha_n W^{(n)} + \alpha_{(n-1)}W^{(n-1)} + \Delta t^{(n)}\Psi(W^{(n+1)}) = 0 \quad (51)$$

where the coefficients  $\alpha_n$  can be expressed as follows:

$$\alpha_{n+1} = \frac{1+2\tau}{1+\tau}, \quad \alpha_n = -1-\tau, \quad \alpha_{n-1} = \frac{\tau^2}{1+\tau}, \quad (52)$$

where  $\Delta t^{(n)}$  is the time step used at the  $n$ -th time iteration and

$$\tau = \frac{\Delta t^{(n)}}{\Delta t^{(n-1)}}. \quad (53)$$

The nonlinear system obtained is linearized as follows:

$$\begin{aligned} \alpha_{n+1}W^{(n)} + \alpha_n W^{(n)} + \alpha_{(n-1)}W^{(n-1)} + \Delta t^{(n)}\Psi(W^{(n)}) = \\ - \left[ \alpha_{n+1} + \delta t^{(n)} \frac{\partial \Psi}{\partial W}(W^{(n)}) \right] (W^{(n+1)} - W^{(n)}). \end{aligned} \quad (54)$$

Following the Unsteady Defect-Correction method of Guillard and Martin [20], the Jacobians are evaluated using the first-order flux scheme (for the convective part), while the explicit fluxes are assembled with second-order accuracy. The resulting linear system is iteratively solved by block-Jacobi relaxation.

### 3.5 Parallelization

The parallelization strategy used in AERO code combines mesh partitioning techniques and a message passing programming model (MPI). The mesh is partitioned into several sub-meshes, each one defining a sub-domain with each sub-domain computed on a different processor. Modifications occurred in the main time-stepping loop in order to take into account one or several assembly phases of the sub-domain results, depending on the order of the spatial assembly of the subdomains and on the nature of the time advancing procedure (explicit/implicit). The assembly of the sub-domain results can be implemented in one or several separated modules and optimized for a given machine. The partitioner should focus primarily on creating well-balanced sub-domains, which will induce a minimal amount of inter-processing communications.

#### 3.5.1 Explicit time integration procedure

For the explicit time advancing model at each time step the following operations are done:

- compute the local time steps,
- compute the nodal gradients and the diffusive fluxes,
- exchange the partially gathered nodal gradients,
- compute the convective fluxes,
- exchange the partially gathered nodal fluxes,
- update the physical states.

#### 3.5.2 Implicit time integration procedure

For the implicit time integration procedure, the algorithm is the following:

- form the implicit matrix,
- exchange the partially gathered diagonal blocks of the implicit matrix,
- **for**  $srl=1$  to  $nsrl$  **do**
  - exchange the partially gathered right-hand sides,
  - perform a Jacobi relaxation,

where  $nsrl$  denotes the number of Jacobi relaxations that need to be done in order to approximately solve the linear system arising at each time step.

## 4 Grid Computing

### 4.1 MecaGRID project

Computer simulations are becoming increasingly important as a means for understanding and interpreting many different processes. The scope and accuracy of these simulations are severely limited by available computational power, even using today's most powerful supercomputers. We can break through these limits by simultaneously harnessing multiple networked supercomputers running single massively parallel simulation to carry out more complex and high-fidelity simulations. This is the basic idea that, since the mid 1990s, motivates the development of computational grids. The Computational Grid concept provides the means for coordinated resource sharing and problem solving in dynamic, multi-institutional virtual organizations. The Grid Computing concept extends older concepts of distributed computing such as cluster-computing, but in contrast to older systems, Grids will in the near future allow resources to be allocated to computing needs on an ad hoc basis.

In recent years there has been a wide-spread acceptance of Grid Computing which lead to several projects. One of these is the MecaGRID project, which started in the 2002 and is sponsored by French ministry of research through the ACI-GRID program <sup>2</sup>. It is a joint project between INRIA-Sophia-Antipolis, CEMEF of the ENSMP (Ecole des Mines de Paris), located in Sophia-Antipolis and IUSTI of the University of Provence, located in Marseille. The aim of the project is to build a computational grid devoted to fluid mechanics, using clusters interconnected by a Virtual Private Network (VPN) see section 4.3.

### 4.2 MecaGRID resources

The computer resources for the MecaGRID project are the clusters of the different members of the MecaGRID project. The computational nodes available are located at three sites connected to each other by VPN. Characteristics of the clusters are detailed in Tab. 2. All nodes are Intel processors under Linux OS, but kernel versions, batch schedules, processors speed and network characteristics are different. The clusters of CEMEF and IUSTI are built on LAN (Local Area Network) where nodes are identified by a private IP address, thus communication between two nodes from different sites, as required by MPI, are not possible. Indeed, a computer in a LAN is not known and not routable through the Internet. To overcome this difficulty a VPN was created between the front end machines of the different clusters.

### 4.3 Establishment of Grid: Globus and VPN

The computational grid used for the MecaGRID project, Ref. [21], simulate one virtual parallel computer, more precisely one virtual cluster. Due to the fact that the cluster of CEMEF and IUSTI have private IP addresses a Virtual Private Network (VPN) was created to pass messages between the different clusters. The INRIA clusters have public IP

---

<sup>2</sup><http://www.recherche.gouv.fr/recherche/aci/grid.htm>

<b>CEMEF at Sophia-Antipolis</b>	
Nodes	: 32 bipro Pentium III (1GHz) with private IP
OS	: Linux Red Hat 7.1
Network	: 2 networks : Myrinet 2 Gb/s + Fast Ethernet 100 Mb/s full-duplex
Parallel libraries	: MPICH 1.2.8 Argonne Myrinet and MPICH 1.2.5 fast ethernet
Batch scheduler	: OPEN PBS
Compilers	: Portland, f90 , f77, C, C++ and GNU f77, C, C++
<b>INRIA at Sophia-Antipolis</b>	
Nodes(pf)	: 19 bipro Pentium III (933 Mhz) with public IP
Nodes(nina)	: 16 bipro Xeon (2 Ghz) with public IP
OS	: Linux Red Hat 2.2
Network(pf)	: Fast-Ethernet Network 100 Mb/s full-duplex
Network(nina)	: Gigabit-Ethernet Network 1 Gbps full-duplex
Parallel libraries	: PVM 3.4.2, MPICH 1.2.5 and LAM/MPI 6.5.4
Batch scheduler	: LSF
Compilers	: Portland, f90, f77, C, C++ and GNU f77, C, C++
<b>IUSTI at Marseille</b>	
Nodes	: 32 Pentium IV monopro (2 GHz) with private IP
OS	: Linux Red Hat 7.2 kernel 2.4.17
Network	: Fast-Ethernet Network 100 Mb/s full-duplex.
Parallel libraries	: MPICH 1.2.5
Batch scheduler	: OpenPBS
Compilers	: INTEL f77, f90, C, C++ and GNU f77, C, C++

Table 2: Table of characteristics for each cluster

addresses, but they are treated by VPN as is they were private. Fig. 2 shows a schematic of the VPN for the present MecaGRID configuration, see Ref. [21] for additional details. The first applications of the AERO code using the MecaGRID are reported by S. Wornom in Ref. [22].

To use a computational grid, a software developed for Grids is necessary. The most widely known is the Globus Toolkit<sup>3</sup> developed at Argonne National Laboratory. It is designed on three elements necessary for computing in a Grid: Resource Management, Information Services and Data Management.

#### 4.4 Parallelism and message passing

The library specification that we use in our computational grid for message-passing is the MPI standard or its implementation, MPICH<sup>4</sup>.

<sup>3</sup><http://www.globus.org>

<sup>4</sup><http://www-unix.mcs.anl.gov/mpi/mpich/>

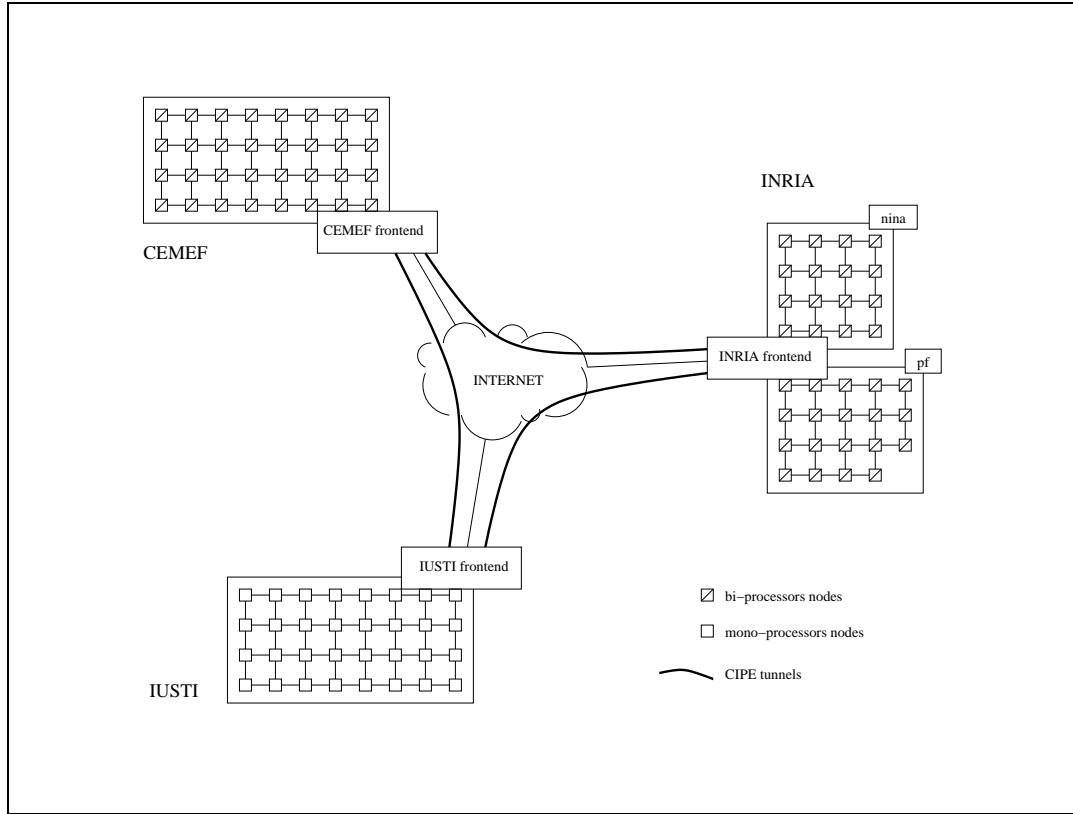


Figure 2: Interconnection of the frontends: a tunnel for each couple of frontends is used to carry TCP packets from or to private IP address.

MPI was designed for high performance on both massively parallel machines and on workstation clusters. It is based on distributed memory model and explicit control of the parallelism. Its advantages are the implicit synchronization with subroutines calls, the portability to distributed and shared memory machines and the absence of data placement problems. In the other hand its drawback are the need of high level communications, the uneasy development and debugging, the large code granularity often required to minimize latency and the possibility to have expensive global operations. MPICH is a portable implementation of MPI. The main goals that this architecture tries to achieve are portability and high performances.

## 5 Jet in cross-flow. Flow dynamics and test-case configuration

JICF configuration is typically constituted by a jet that issues into a cross-flow. In the following chapters we will discuss the case, shown schematically in Fig. 3, of a single rounded jet that issues into a flat plate.

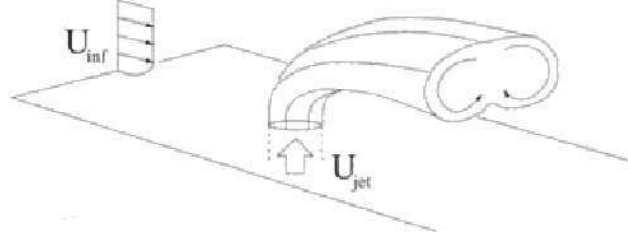


Figure 3: Global flow-field associated with a jet in cross-flow

Operating conditions for the jet in cross-flow are often characterized in terms of a variety of parameters which influence the physical behavior and that are used to scale the characteristic features of the JICF. From this view-point, the most important parameters are the mean jet-to-cross-flow momentum flux ratio,  $J$ , the mean scalar jet-to-cross-flow velocity ratio,  $R$ , and the Reynolds numbers,  $Re_j$  and  $Re_\infty$ , which are defined as follows:

$$J = \frac{\rho_j \bar{U}_j^2}{\rho_\infty \bar{U}_\infty^2}, \quad R = J^{1/2}, \quad Re_j = \frac{\bar{U}_j D}{\nu_j}, \quad Re_\infty = \frac{\bar{U}_\infty D}{\nu_\infty}.$$

where  $\bar{U}_j$  and  $\bar{U}_\infty$  stand respectively for the jet and the cross-flow velocity,  $D_j$  is the jet nozzle diameter and  $\rho_j$ ,  $\rho_\infty$ ,  $\nu_j$  and  $\nu_\infty$  are respectively the density and the kinematic viscosity of the flow for the jet and for the cross-flow.

For flows characterized by low Mach numbers, where density is approximately constant,  $R = \bar{U}_j / \bar{U}_\infty$ .

The independent non-dimensional parameters typically used are the mean scalar jet-to-cross-flow velocity ratio,  $R$ , and one of the Reynolds number, usually  $Re_j$ . Beyond the complex dynamics, difficulties in studying this subject are also related to the combined effects of these parameters.

The subject of the jet in a cross-flow (JICF) has been widely studied. It is important either from the engineering viewpoint, being very frequent in practical applications because



of its ability to mix rapidly with cross-flow and to introduce a controlled jet force into flow-field (e.g. injectors for cooling systems, jets for V-STOL aircraft, exhaust of vehicles) or for basic research, because of the variety of fluid dynamic phenomena involved. Investigations on the JICF have started in the 1930s, Ref.[28]. Since, there have been numerous investigations on the JICF leading to the perception that the JICF, in contrast to other flows like jets and mixing layers, cannot be described in terms of self similarity and Reynolds dependence, due to the strong nonlinear effects. The systematic analysis of the JICF started in 1970s with the discovery and acceptance of coherent structures that are able to explain various nonlinear effects in the JICF.

### 5.1 Vortex system associated with the transverse jet

The complicate nature of the JICF is illustrated in Fig. 4, where the flow behavior for a velocity ratio  $R = 2$  is represented. This figure was obtained from the flow-visualization measurements of Foss, Ref. [23], and from the velocity measurements of Andreopoulos and Rodi, Ref. [24]. The most obvious feature of the JICF is the mutual deflection of jet and cross-flow. The jet is bent over by the cross-stream, while the cross-stream is deflected as if it were blocked by a rigid obstacle. Fig. 4 shows also that the fundamental characteristics of the JICF are dominated by a complex, three-dimensional, inter-related set of vortex systems in the lee of the jet.

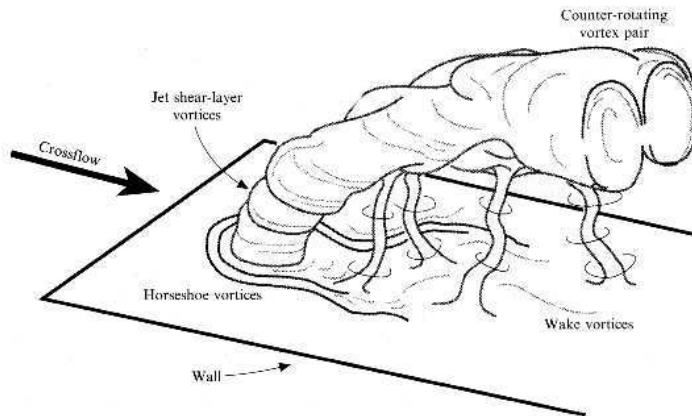


Figure 4: Schematic diagram of the vortex system associated with the JICF

With reference to Fig. 4 we may attempt to classify the main structures as follows:

- *Class 1 structures*
- *Class 2 structures*

### 5.1.1 Class 1 structures

The *class 1 structures* are originated by the interaction of the jet with the cross-flow and the wall and cannot be recognized in free jets. Among structures of this kind we may include the following vortex systems, Ref. [24] and Ref. [25]:

- *Counter-Rotating Vortex Pair (CRVP)*
- *Horseshoe Vortices (HSV)*
- *Upright vortices (UV)*

**Counter-rotating vortex pair (CRVP)** The CRVP, Fig. 5, is the most dominant vortex system and is generated as an effect of the bending of the jet itself. The mechanism for the formation of the CRVP is not yet fully understood. It can be taken as certain, that the vorticity of the CRVP has its origin at the side-walls of the jet. In fact, Haven et al. Ref. [27] investigated different nozzle geometry for the jet and discovered that for rectangular jets the amplitude of the CRVP depends on the aspect ratio of the jet section. A variety of interpretations of CRVP and its origin have evolved over the years. In general, however, CRVP is widely viewed to be formed by the vortex sheet or thin shear layer emanating from the jet nozzle.

It is generally accepted that the shear layer of the jet folds and rolls up very near to the pipe exit, leading to or contributing to the formation of the CRVP, although there are questions pertaining to the nature of vortex roll-up near the jet exit. Tilting and folding of the vortical structures are seen to contribute to the downstream components of vorticity which form, on an averaged basis, counter-rotating vortical structures.

The origin and development of the CRVP are important because control of vorticity generation and evolution is a mean of controlling transverse jet mixing and, potentially, reaction processes.

**Horseshoe vortices (HSV)** The HSV, Fig. 6, is formed upstream of the jet and close to the wall and result from the interaction between the wall boundary layer and the round transverse jet. HSV are found to be steady, oscillating, or coalescing. Frequencies of oscillation have been found to be correlated with periodic motions of upright vortices.

**Upright vortices (UV)** The UV are generated by the interaction of the wall boundary layer with the jet flow and, for low  $Re_j$ , are the only unsteady structure.

### 5.1.2 Class 2 structures

The *class 2 structures* are proper for free jets, but their vorticity content, evolution and destabilization are in some way influenced by the presence of the cross-flow. Structures of this kind are:

- *Ring-Like Vortices (RLV)*

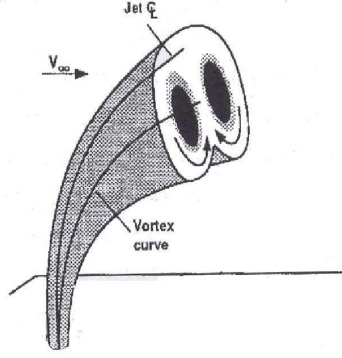


Figure 5: Counter-rotating vortex pair

**Ring-like vortices** The RLV are formed from the shear layer of the jet flow and their shape and spatial evolution is distorted by the presence of the cross-stream. With the CRVP, they determine the dominant features of the velocity and vorticity fields and their dynamics is of great interest from the practical viewpoint since they are mainly responsible for mixing and for mass, momentum and heat transfer.

## 5.2 Flow configuration

The flow configuration used in our simulations is that of a jet which forms from a pipe flow and then issues into a flat-plate boundary layer through an orifice in the plane of the flat plate.

The velocity ratio,  $R$ , is a very important parameter for this configuration, indeed, the flow regime can change depending on  $R$ . If  $R < 0.5$  the jet flow is weaker than the cross-flow, so it is not able to break through the wall boundary layer of the cross-flow and plays the role of an obstacle for the cross-flow. In this case the far field is primarily governed by the cross flow. This flow configuration is important for turbine blade coolings. If  $1 < R < 10$  the jet is able to push through the boundary layer, which plays a smaller role. These velocity ratio are common for combustion applications. The velocity ratios higher than 10 have different features as they behave more and more like free jets with increasing velocity ratio.

In our simulations we have used a velocity ratio of 2. The considered Reynolds number, based on the pipe diameter and on the jet velocity,  $U_j$ , is:

$$Re = \frac{L U_j}{\nu} = 82000, \quad (55)$$

and the Mach number of the undisturbed flow,  $M$ , is assumed to be equal to 0.1.

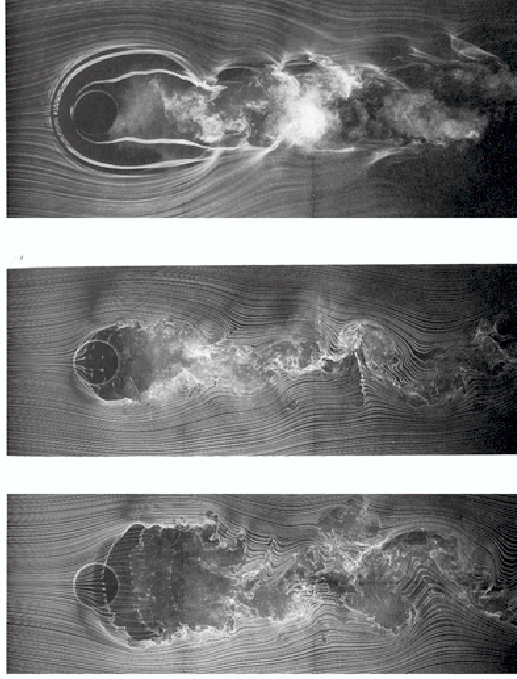


Figure 6: Streamlines obtained experimentally by Roshko [29] for velocity ratio  $R = 2$  and  $Re_{cf} = 7600$  for planes at  $z = 0^+$ ,  $z = 0.5D$  and  $z = 1D$

### 5.3 Mesh geometry

The chosen coordinate system is described in Fig.9. The origin of the coordinate system is located at the center of the pipe at the same level of the flat plate and  $x, y, z$  represent respectively the coordinates in the streamwise, spanwise and normal-wall directions. Moreover,  $u, v, w$  represent the velocities in each of the three directions.

The size of the domain is  $L_x = 26D$  in the streamwise direction,  $L_y = 8D$  in the spanwise direction and  $L_z = 9D$  in the vertical direction. The center of the jet is  $L_{jet}^{in} = 5.5D$  downstream of the cross-flow inlet plane and the pipe length is  $L_{jet} = 5.5D$  plus another  $5D$  length to simulate the plenum chamber.

The spatial discretization of the flow is based on hybrid meshes. This kind of meshes allow structures meshes to be used where a better control of the point distribution in the

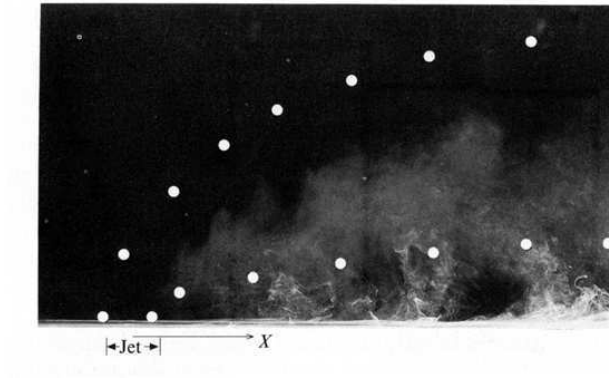


Figure 7: Sideviews of upright vortices visualized by Roshko [29]

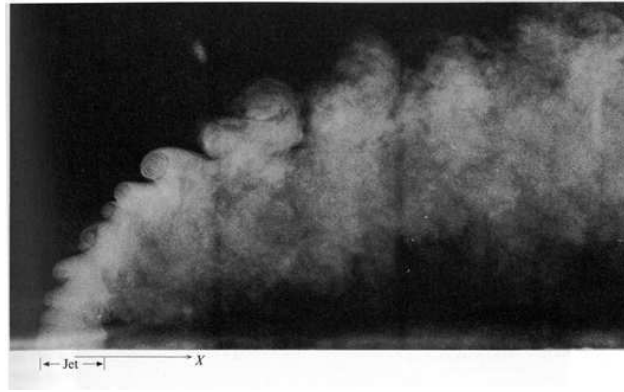


Figure 8: Transverse jet shear layers structures visualized by Roshko [29]

flow is needed.

These grids have been built by decomposing the computational domain in subdomains. The used subdomains are shown in Figure 10 Meshing the pipe, Figure 12, the part of the flat plate upstream and downstream of the jet orifice, respectively Figure 14 and Figure 13, the joint between the structured and unstructured part of the mesh over the pipe, Figure 15, and the boundary layers is very important to have good simulations results so they are built using a fine structured mesh. For the pipe, in fact, there is an influence of the cross-flow to the jet in the pipe. The existence of a recirculation zone at the edge of the jet nozzle

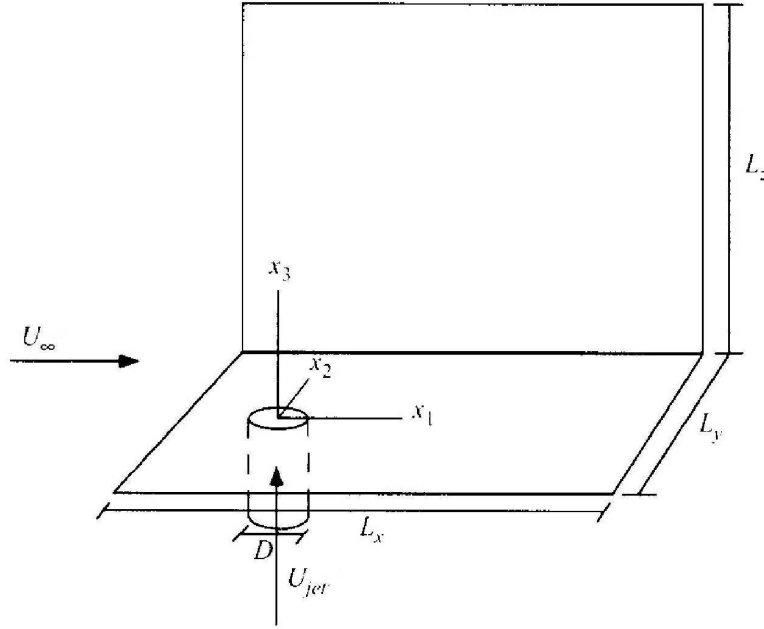


Figure 9: Coordinate system

makes this area sensitive to mesh point distribution. Thus, the mesh has to be fine enough to capture the recirculation zone. The part of the flat plate downstream of the jet is very important because, as described in Chap.5.1, here are located several vortical structures.

The total number nodes is  $3.98 \cdot 10^5$  and about  $1/3$  of them is in the pipe. The dimension of the first control volume next to the jet exit, next to the flat plate wall at the entry of the flow and next to the boundary layer of the flat plate on the symmetry plane of the flat plate downstream and upstream of the jet orifice are described in Table 3.

#### 5.4 LES validation test case

The case chosen to validate the simulation is a series of experiments carried out by Andreopoulos and Rodi, Ref.[24]. They provide detailed hot wire measurements of the mean velocity components, the turbulent kinetic energy, the Reynolds stresses and measurements of the turbulent kinetic energy budget. In these experiments the velocity ratio varies from  $R = 0.5$  to  $R = 2$  and for this values  $Re_j = 20500$  and  $Re_j = 82000$  are used respectively.

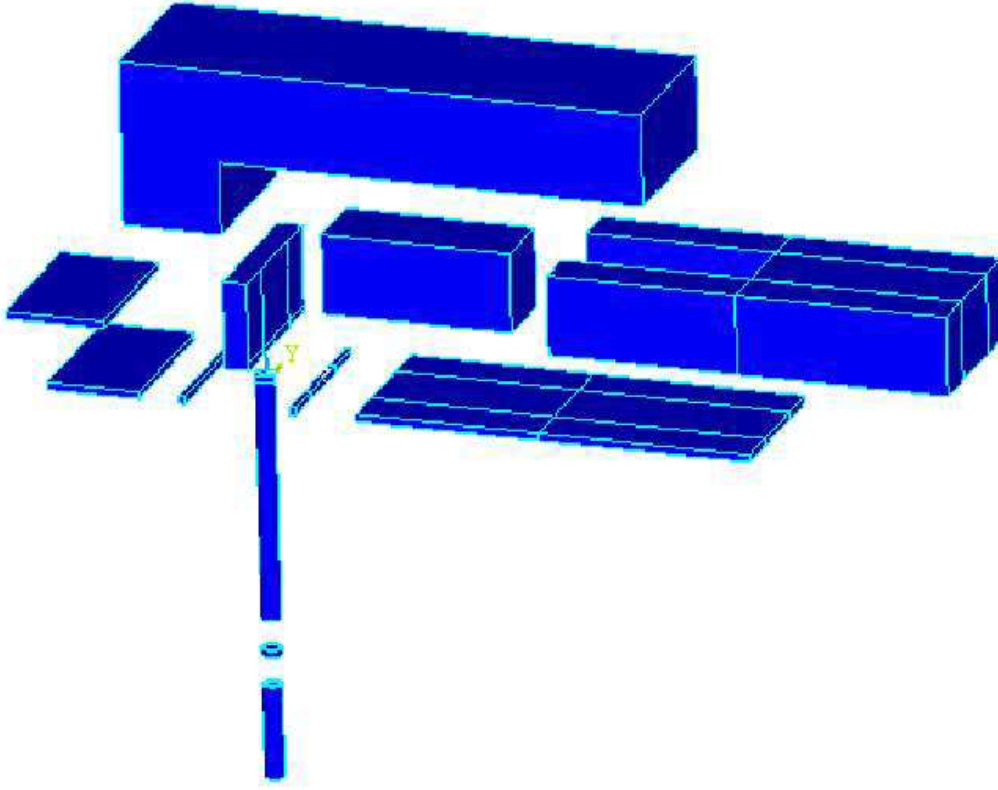


Figure 10: Domains used to build the mesh

### 5.5 Boundary and initial conditions

On the lateral and top surfaces of the flat plate free-slip boundary conditions are prescribed, while on the bottom of the flat plate and on the lateral walls of the pipe no-slip boundary conditions are assigned. The outflow condition used is a zero gradient condition for all flow variables. In Andreopoulos and Rodi, Ref.[24], both pipe flow and cross-flow are turbulent and four diameters upstream of the jet exit, on the plate, where the jet interference on the cross-stream is negligible, a friction coefficient  $C_f = 0.0037$  and a boundary-layer thickness of  $\delta = 0.278D$  are measured. To try to obtain this condition a plenum chamber 5D long was introduced before the pipe. A constant velocity profile is used as input for both flat plate entry and pipe entry. The boundary conditions for the velocities are:

$$\vec{v}^* = U_{cf} \cdot \vec{i}, \quad \vec{v}^* = U_j \cdot \vec{k}$$

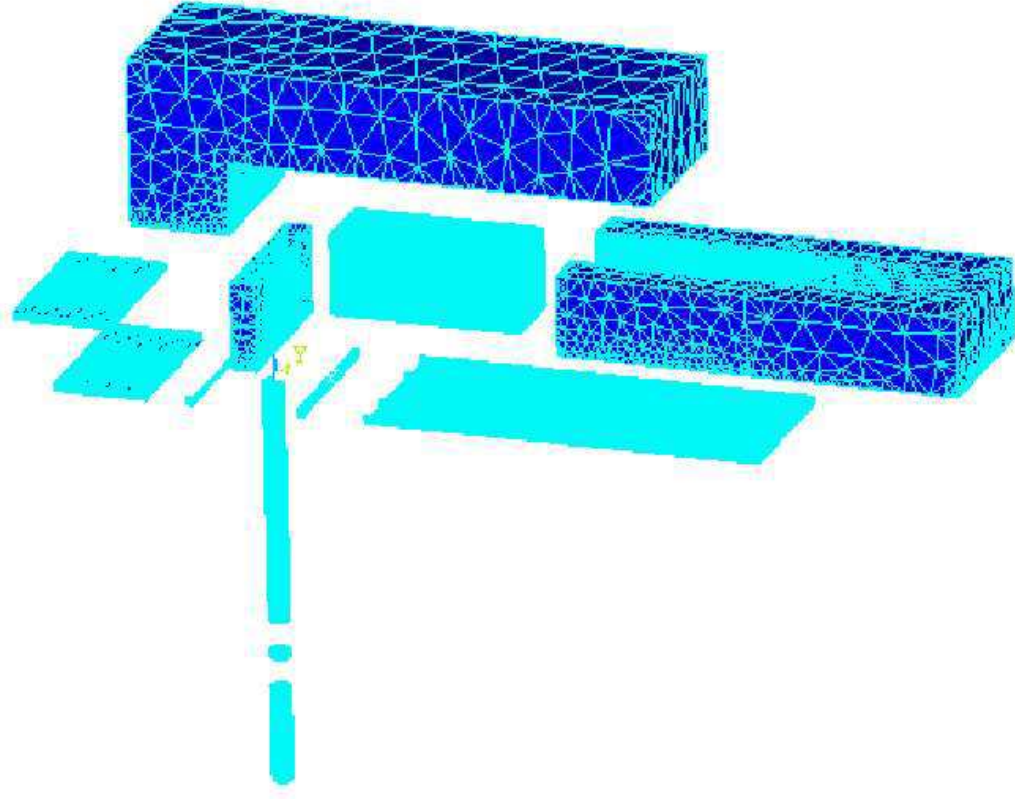


Figure 11: Whole mesh of the test case

where  $U_{cf} = 1$  and  $U_j = 2$  and the sign “\*” stands for non-dimensional quantities.

For the other variable, instead, is chosen:

$$p^* = 1, \quad \rho^* = 1 .$$

To set the initial condition the domain is divided in 5 parts. The cross-flow is characterized by a constant velocity along all the streamwise length equal to  $\vec{v}^* = U_{cf} \cdot \vec{i}$ .

The velocity in the pipe is constant and equal to  $\vec{v}^* = U_j \cdot \vec{k}$  in the zone next to the entry and decreases linearly until zero in the joint between the pipe and the flat plate. As for velocity, pressure is constant at the inlet of flat plate and pipe and equal to the reference value, so  $p_{in}^* = 1$ . Moreover, it is constant in a zone next to the outlet of the flat plate and equal to  $p_{out}^* = p_{in}^* \cdot 0.98$  and decrease linearly in the other place in such a way to have no



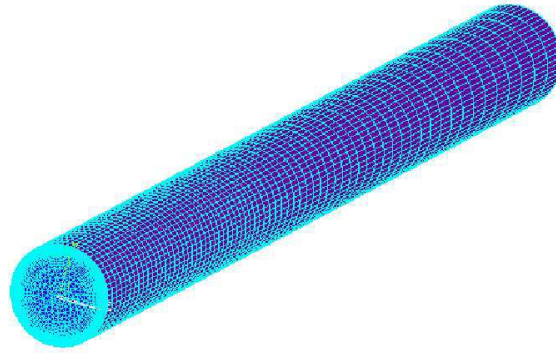


Figure 12: Detail of the mesh of the part of the domain over the flat plate boundary layer upstream of the pipe

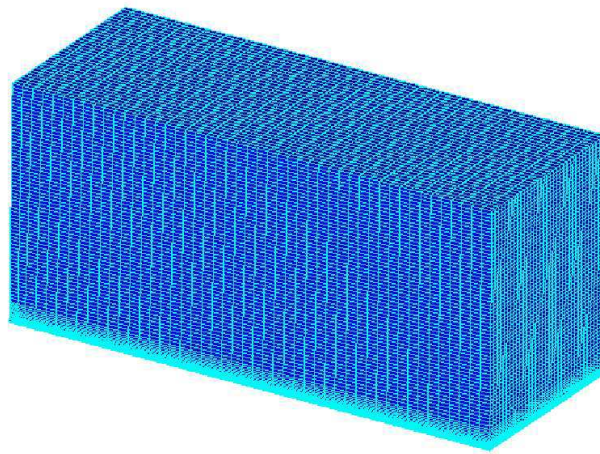


Figure 13: Detail of the mesh of the part of the domain over the flat plate boundary layer downstream of the pipe

discontinuity. The same is done for the density. The initial conditions are shown in Figure 16.

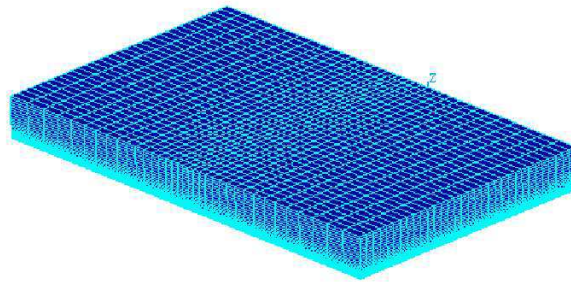


Figure 14: Detail of the mesh of the flat plate upstream the jet orifice

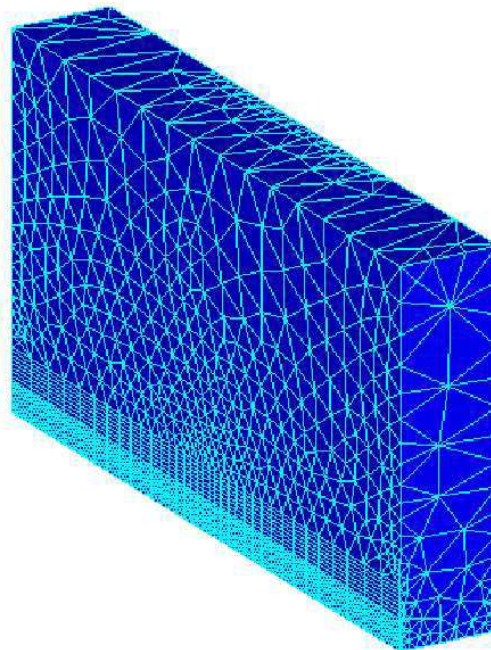


Figure 15: Detail of the mesh of the joint over the pipe

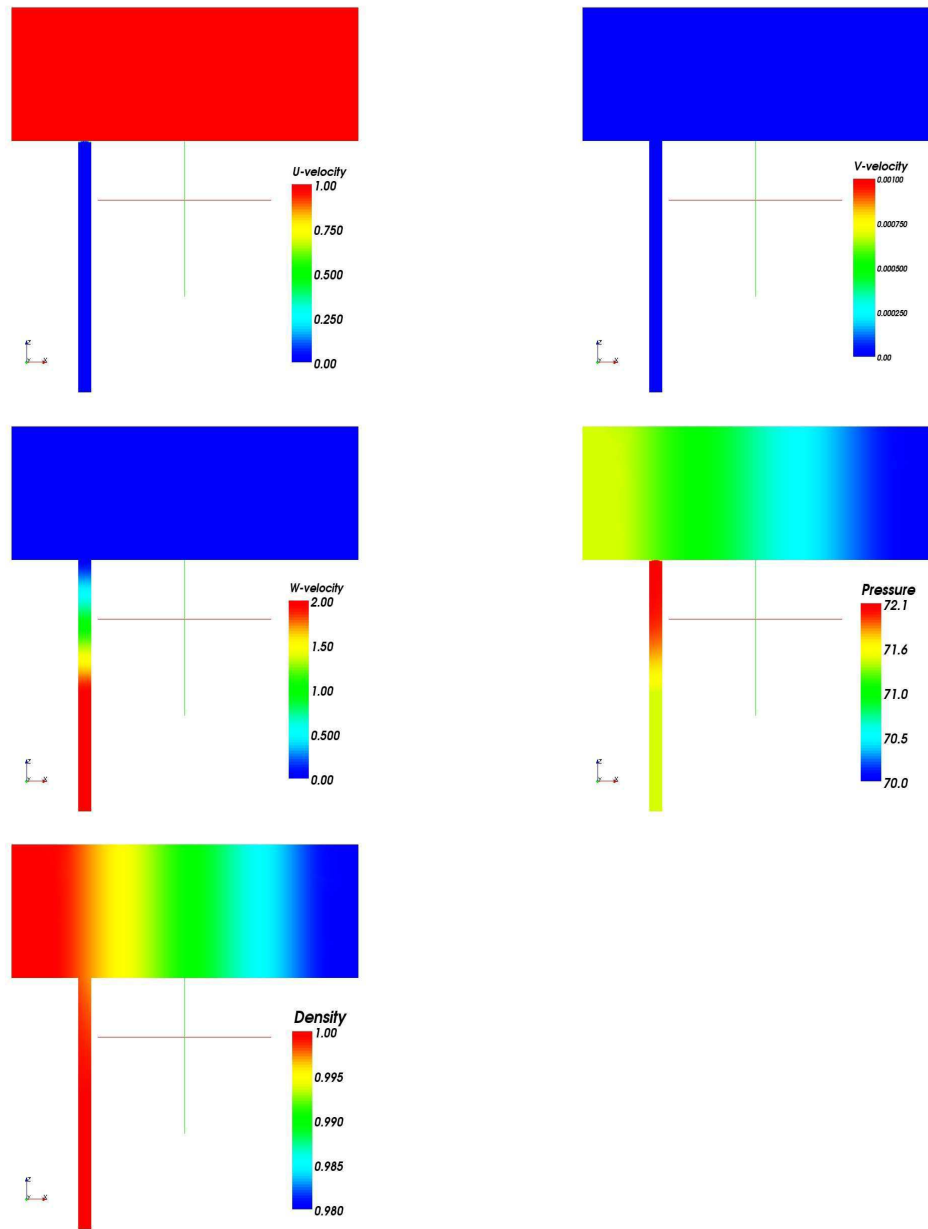


Figure 16: Initial conditions

<b>Structured part of the pipe</b>
$\Delta r = 0.002D$ (24 nodes) $\Delta \theta = 0.052D$ (60 nodes) $\Delta z = 0.118D$ (68 nodes)
<b>Flat plate boundary layer</b>
$\Delta x = 0.719D$ $\Delta y = 0.103D$ $\Delta z = 0.011D$ ( $h^+ \simeq 30$ )
<b>Flat plate upstream of the pipe over the boundary layer</b>
$\Delta x = 0.153D$ $\Delta y = 0.385D$ $\Delta z = 0.047D$
<b>Flat plate downstream of the pipe over the boundary layer</b>
$\Delta x = 0.202D$ $\Delta y = 0.103D$ $\Delta z = 0.067D$

Table 3: Characteristics of the mesh: All the value about the cross-flow are referred to the symmetry plane of the flat plate.  $\Delta r$  is the radial dimension of the element and  $D$  is the diameter of the pipe;  $\Delta \theta$  is the circumferential dimension of the element;  $\Delta z$  is the axial dimension of the element;  $h^+ = zU_\tau/\nu$  where  $U_\tau$  is the friction velocity;  $\Delta x$  is the streamwise dimension of the element;  $\Delta y$  is the spanwise dimension;  $\Delta z$  is the normal-wall dimension.

## 6 Results of the LES simulation

### 6.1 Simulation parameters

The results shown in the following sections are referred to the jet in cross-flow configuration described in Chap. 5 and they have been obtained by a LES computation using the code AERO (Chap. 3). For the spatial discretization of the equations the V6 scheme has been used, while for the time advancing the implicit scheme with a maximum CFL number equal to 20 has been selected. For SGS modeling the Smagorinsky model (see Sec. 2.3.3) has been used.

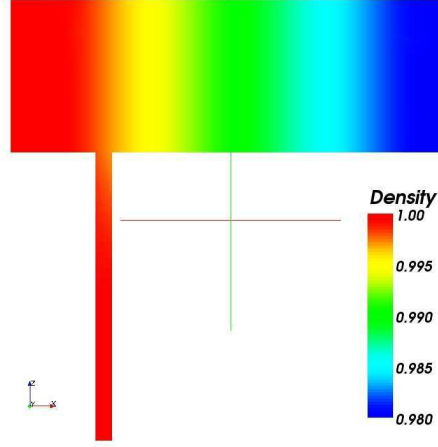


Figure 17: Initial density

In the AERO code, the parameter  $\gamma_s$ , (see Sec. 3.2.1), controls the numerical viscosity of the scheme. Results of previous studies, Ref. [4], indicate that the numerical viscosity should be reduced as far as possible in order to obtain reliable results in LES. On the other hand, it was also shown that SGS viscosity acts as a stabilizing term for the velocities and that significantly less upwind is necessary for stability when SGS models are used. The lowest value of  $\gamma_s$  needed for the numerical stability of the simulation described in the following section is equal to 0.5 for the first part of the simulation until the simulation time  $t = 16T$ , where  $T$  is the characteristic time, i.e. the time that a particle with the same velocity of the cross-flow needs to cover 1 pipe diameter,  $D$ . After  $t = 16T$ ,  $\gamma_s = 0.4$  is used.

These values were needed to ensure the stability of the simulation mainly in the pipe, which is the most critical region for the used grid. The time interval used to compute the statistical quantities is  $6T$ , where  $T$  stands for the characteristic time, from  $t_1 = 30T$  to  $t_2 = 36T$ . This interval has been chosen because we have verified, by comparison with statistical quantities obtained over  $12T$  that it is sufficient to have converged statistics.

## 6.2 Reproduction of general flow characteristics

The part of the domain interesting for post-processing is the zone immediately downstream of the jet orifice, until  $x = 10$ , where the mesh is fine enough for LES. In Figure 18, the density field in the symmetry section of the flat plate is shown. We can see that, when the mesh becomes coarser, the numerical damping is such that the structures are no more maintained.

In the following sections we will describe the main structures of the flow and we will compare the averaged and fluctuating fields with experimental results.

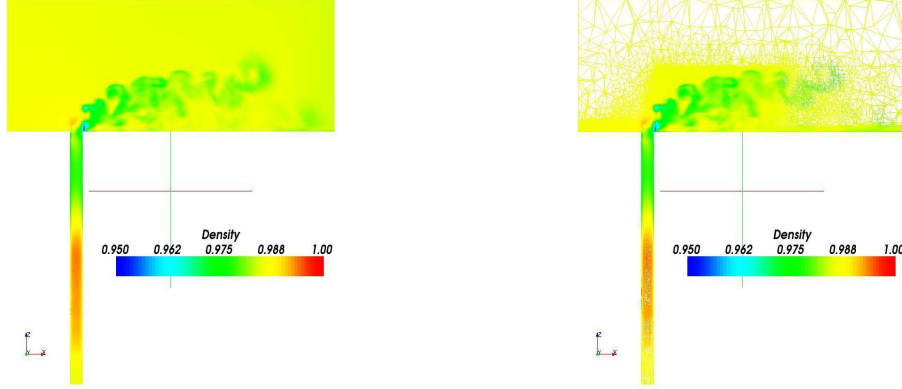


Figure 18: Mesh and density fields in the symmetry plane after a simulation time  $t = 30T$ .

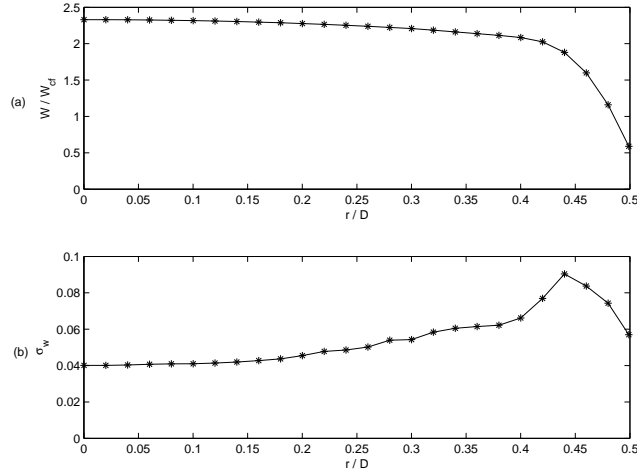


Figure 19: Averaged  $W$  velocity profile and RMS for the  $W$  velocity in the pipe at  $z = -1 D$ .

In Figure 19 the averaged velocity profile obtained in our simulation at  $1D$  upstream of the jet exit is shown. It is computed by averaging in time and in the homogeneous azimuthal direction. We can see in Figure 19(a) the typical top hat profile which characterizes turbulent flows and in Figure 19(b) the fluctuations present in the pipe. They are described through the RMS,  $\sigma_w$ , of the fluctuations in the axial directions,  $w'$ . Even if the plot of Figure 19(b)

only shows the resolved part of the fluctuations and the sub-grid part of the fluctuations is not described, we can see that we have significant fluctuations in the pipe, which have developed from steady plug flow inlet condition without need at ad-hoc treatments.

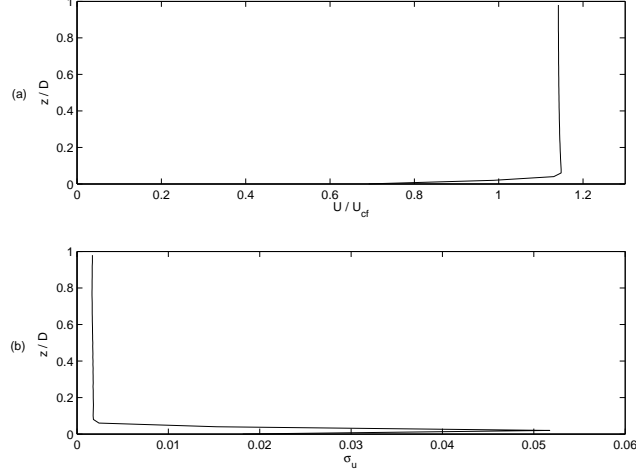


Figure 20: Averaged U velocity profile and RMS for the U velocity in the flat plate at  $x = -4D$ .

Figure 20 represents the velocity profile on the flat plate 4 diameters upstream the jet orifice. The boundary layer thickness is approximately equal to  $\delta_{num} = 0.1D$ , instead of  $\delta_{exp} = 0.278D$  of the experiments of Andreopoulos et al., Ref. [24]. It means that the inlet velocity profile in our simulation is not well developed in comparison with the experiments of Andreopoulos et al.. However, from the previous numerical works, as the one of Yuan et al., Ref. [31], it seems that the boundary conditions at the inlet of the flat plate are not so important as the ones at the inlet of the pipe. In the future, a Reichardt velocity profile, which allows the same friction coefficient and boundary layer thickness of the experiments to be obtained (see Section 3) could be used to have a better matching between experimental and numerical cross-flow conditions.

### 6.2.1 Horseshoe vortex (HSV)

Figures 6 (a)-(b)-(c) show the streak lines on planes at  $z = 0^+D$ ,  $z = 0.5D$  and  $z = 1D$  respectively, for a velocity ratio,  $R = 2$  and a Reynolds number,  $Re = 3800$ , obtained experimentally by Roshko et al., Ref. [29].

Even if the Reynolds number of our simulation is much higher, they represent qualitatively the HSV that characterize jets in cross-flow at  $R = 2$ . From the visualization of Roshko et al. [29], we can see that the HSV phenomena is similar to the vortex shedding which is present behind a cylinder, thus, the HSV is better described by the instantaneous

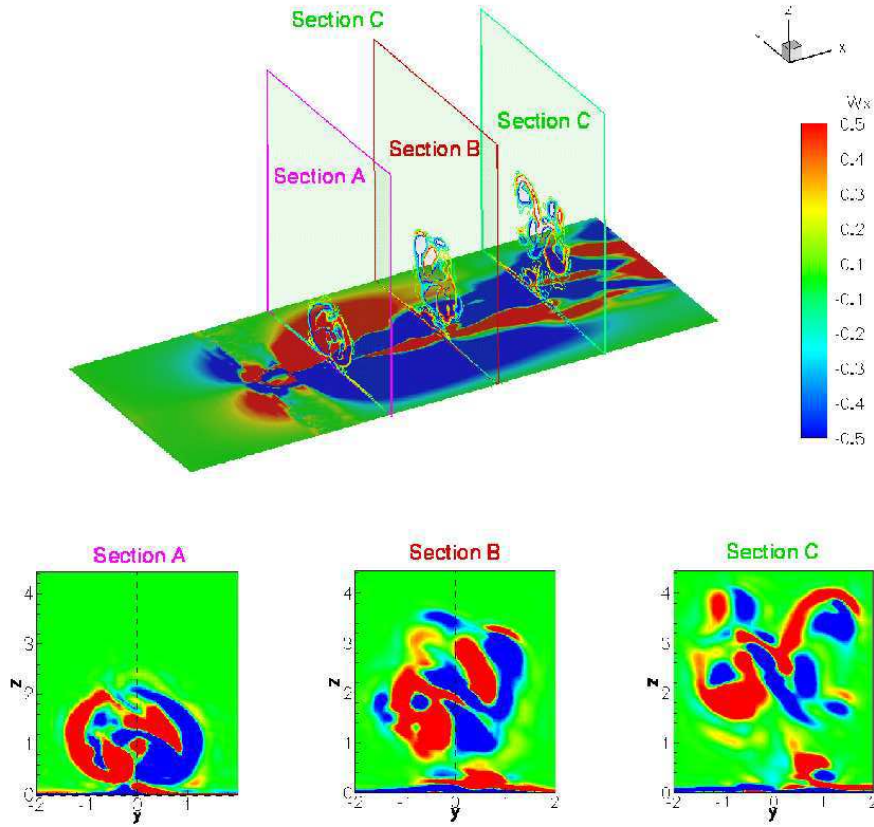


Figure 21: Instantaneous streamwise component of the vorticity field on a plane at  $z = 0.001D$  and in some planes in the streamwise direction. Section A, B, C are planes at  $x = 2D$ ,  $x = 6D$  and  $x = 10D$  respectively

variables. Due to the fact that it is impossible to reproduce streak lines with our tool-box, we can prove the existence of structures similar to the ones shown by Roshko by plotting the instantaneous streamwise vorticity field represented in Figure 21. The upper part of the figure shows the streamwise component of the vorticity,  $\omega_x$ , for a plane at  $z = 0.001D$  and the ISO-contours of the streamwise component of the vorticity for three sections downstream the jet orifice,  $x = 2$  (Section A),  $x = 4$  (Section B) and  $x = 10$  (Section C). The bottom part of the figure shows the zoom of the streamwise component of the vorticity on the  $y$ - $z$  planes previously mentioned. Near the wall, the two vorticious zones of opposite vorticity value represent the HSV. In the visualizations of Roshko, see Figure 6, we can see that an alternate structure characterize the HSV. This can be found in our simulation too, by



looking, for instance, at the modulus of the velocity, Figure 22. A trace of these structures can also be found in the averaged field, see Figure 24.

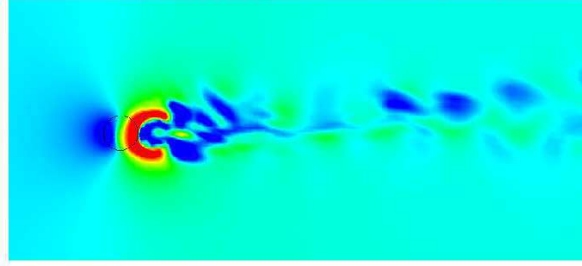


Figure 22: HSV: Modulus of the instantaneous velocity field on a plane at  $z = 0.5D$

In Figure 23 a zoom of the zone near the pipe is shown. Near the flat plate inlet there is a region where the vorticity is positive for  $y > 0$  and negative  $y < 0$ . This is due to the presence of a transverse velocity due to the need of the crossflow located near the wall to turn around the jet. Due to the fact that the velocity at the wall is near to zero, we have a velocity gradient in the vertical direction which create the streamwise vorticity shown in Figure 23. The vorticity present nearer and after the pipe, instead, is due to the presence of the HSV. Both those vortical regions are interrupted at the side of the jet exit. This is due to the mesh used in this zone, which is shown in Figure 23 (b)-(c)-(d). Indeed, in this zone we have an unstructured mesh which joints the structured grid upstream and downstream the jet orifice and in the pipe. In the streamwise direction the mesh is fine enough, as shown in Figure 23(b), which shows the mesh on a plane at  $z = 0.001D$ . Conversely, in the normal-wall direction it is too coarse to be able to give a good representation of the vorticity, as shown in Figure 23(c) and (d). Figure 23(c) shows the mesh on a plane x-z at  $y = -2D$  and Figure 23(d) describes the zoom indicated in Figure 23(c) related to the zone near the wall of the plane at  $y = -2$ . At the end of the unstructured zone, the vorticity starts again to be well represented. Thus, due to the fact that the vorticity is computed in a post-processing tool from the discrete velocity field, numerical errors are larger for this variable, especially where the mesh is coarser.

### 6.2.2 Counter-rotating vortex pair (CRVP)

In Figure 24 the averaged vorticity fields on the bottom wall ( $z = 0.001D$ ) and in some sections at constant  $x$  (Section A:  $x = 2$ ; Section B:  $x = 6$ ; Section C:  $x = 10$ ) are shown. Here we can see the CRVP which are described by the largest vortical structures located in the upper part of the sections. We can see that these structures are well represented near the pipe orifice and are less concentrated if we move more downstream. This can be due to the fact that the phenomenon is less strong or that the mesh becomes coarser moving downstream.

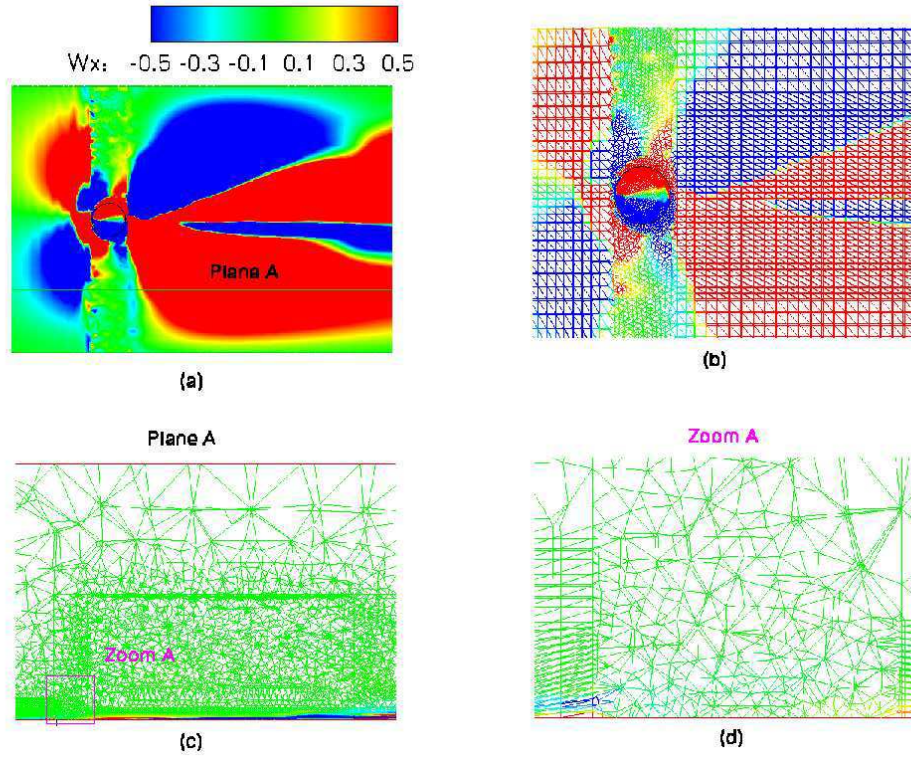


Figure 23: HSV:(a) vorticity field on a plate at  $z = 0.001D$ ; (b) mesh on a plane at  $z = 0.001$  (c) mesh and vorticity field on a the plane A, shown in figure (a) at  $y = -2$ ; (d) zoom of the mesh near the jet orifice on a plane x-y

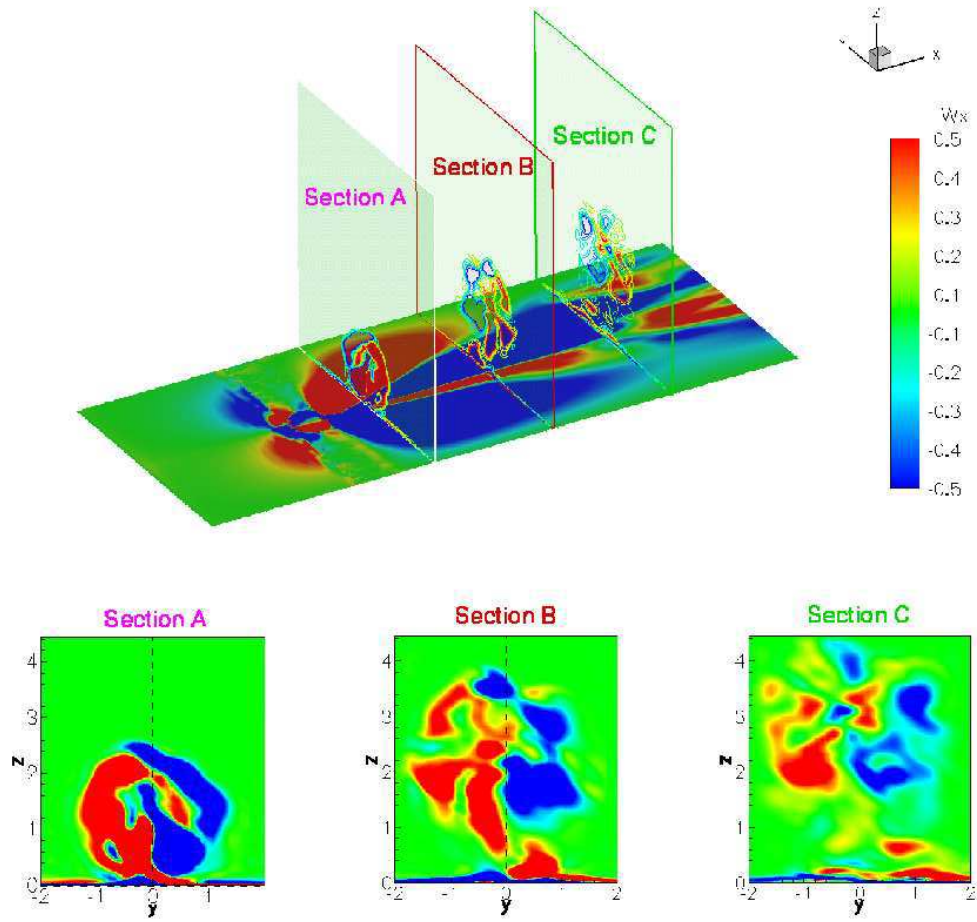


Figure 24: Averaged vorticity field on a plane at  $z = 0.001$  and on some sections at  $x$  constant ( $x = 2$ , section A;  $x = 6$  section B;  $x = 10$  section C)

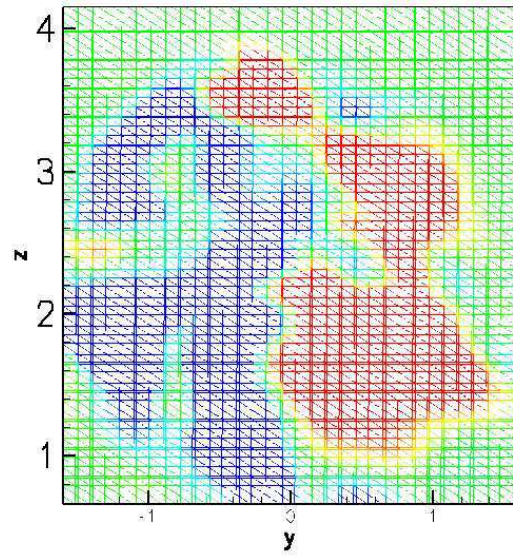


Figure 25: Zoom of the mesh and vorticity field on a plane  $x = 6D$ . All tetrahedron are cut in the same direction

the jet orifice. These vortices should be symmetric as regards to the jet symmetry plane, but this is not verified in our simulation, especially far from the jet orifice. If we look carefully to the mesh we can note that it is non-symmetric. All tetrahedron are cut in the same direction and this may create a preferential direction in which the vortices are elongated, as shown in Figure 25

### 6.2.3 Ring like vortices (RLV)

In Figure 26 RLV are represented. We can see that the structure of these vortices is similar to the one obtained by Roshko et al., Figure 8. In the upstream shear layers of the jet the vortices are more similar to the ones that characterize the flow of a free jet, but in the downstream shear layer of the jet these vortices are present only near the jet exit and, then, they are inglobed in the other vortical structures, mainly CRVP which are supposed to be created by this vortical structures which originate from the pipe.

### 6.2.4 Upright vortices (URV)

The URV are not reproduced in our simulation. Probably, this is due to the fact that at  $R = 2$  the CRVP and the HSV are very close each other and, hence, the URV are very short and thus difficult to be identified (see Figure 7).

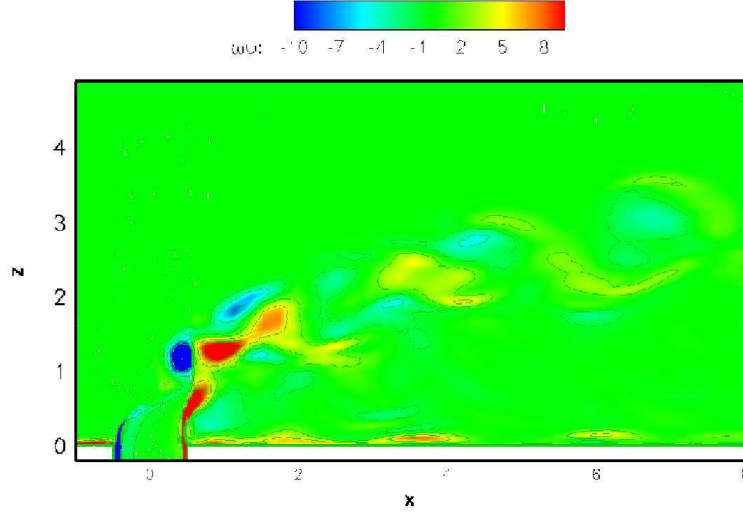


Figure 26: RLV: Instantaneous transverse component of the vorticity on the jet symmetry plane

## 6.3 Flow statistics

### 6.3.1 Mean velocities

In Figure 27 the ISO-contours of the computed, time-averaged vertical velocity field,  $W$ , in the symmetry plane of the pipe are shown.

As expected, the cross-flow bends the jet which rise from the pipe and the jet velocity profile is rapidly blunted by this interaction. The ISO-contours are qualitatively similar to the large eddy simulation of Yuan et al., Ref. [31] even if we can not make quantitative comparisons because our flow conditions are different from those in Ref [31] ( $R = 3.3$  and  $Re = 4820$ ). Nevertheless, in Figure 27, as in the Figure 22 Ref. [31], two regions of strong upward velocity are shown. The upper region is located directly over the jet exit and is due to the vertical momentum of the jet. The magnitude of this vertical momentum decays as the jet flow is dispersed away from the center plane. The lower region of vertical velocity forms behind the jet exit.

In Figure 28 the ISO-contours of the computed, time-averaged streamwise velocity field,  $U$ , in the symmetry plane of the pipe are shown down. Near the flat plate, the cross-flow

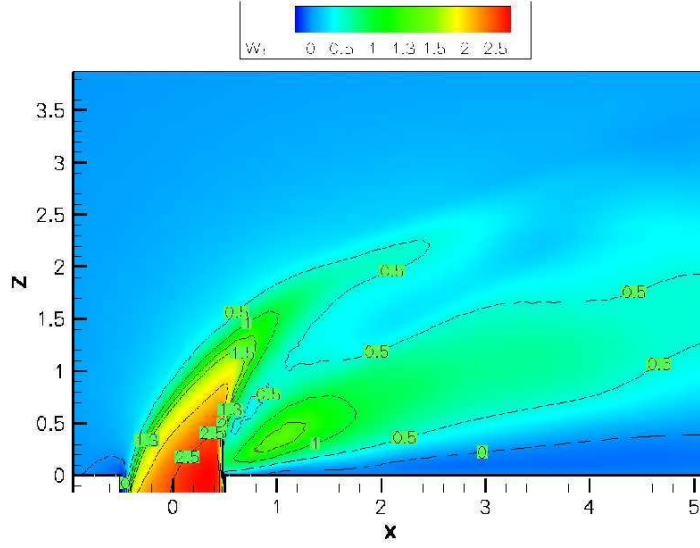


Figure 27: Time-averaged vertical component of the velocity,  $W$ , in the jet symmetry plane

slows and stagnates as it approaches the jet exit. Where the cross-flow is deflected over the bending jet, the cross-flow accelerates. Where we have the maximum bending of the jet, the maximum of the streamwise velocity values lie on the jet axis. More downstream, maximum streamwise velocities lie above the trajectory. It means that the fluid is pushed upward by the flow created by the CRVP and is concord with the results shown in Figure 21 by Yuan, Ref. [31].

Figure 29 shows how longitudinal mean velocity  $U$  varies with distance,  $z$ , from the wall at various downstream positions,  $x$ , in the jet symmetry plane. The velocity profiles correspond, from left to right, to  $x$ -positions of 2D, 4D, 6D and 10D respectively and they are compared to the experimental data from Andreopoulos et al., Ref. [24].

The experimental measurements very near the wall are not available, because they could not be carried out in this zone. For the velocity ratio which is used for our simulation,  $R = 2$ , the velocity overshoots the free stream value only before  $x/D = 10$ . As shown in Figure 29 the  $U$ -velocity profiles are similar to the experimental data even if in our simulation the  $U$ -velocity is higher near the wall. For  $x/D = 10$  the axial velocity component obtained in our simulation tends to the asymptotic velocity of the cross-flow, as if the jet was not present. Conversely, in the experiments it tends to a lower value. This can be due to the excessive numerical dissipation present in our simulation due to the coarseness of the mesh at those location, which may lead to an early mixing between the jet and the cross-flow.

Figures 30 and 31 show the transverse and normal velocity components,  $V$  and  $W$  respectively. The measurements are given on the jet symmetry plane for some sections downstream



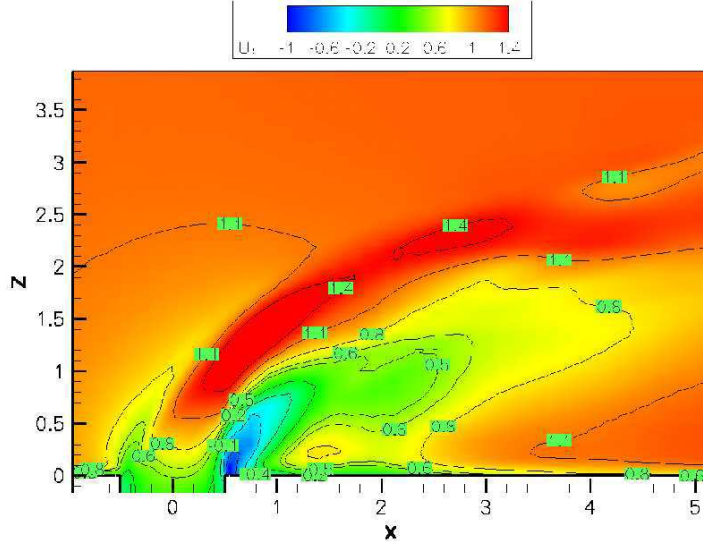


Figure 28: Time-averaged streamwise component of the velocity,  $U$ , in the jet symmetry plane

the jet orifice and namely for planes at  $x = 4$  (a),  $x = 6$  (b) and  $x = 10$  (c). For the transverse velocity the differences between experimental and numerical results are quite small, while they are larger for normal velocity. This is mainly due to the fact that the counter rotating vortices are not perfectly symmetric with respect to the jet symmetry plane on which the profiles are measured, as shown in Figures 24 and Figure 25. Thus, in our simulation this plane cuts a zone with negative vorticity belonging to the right counter rotating vortices, as shown in Figure 24; this vorticity induces a significant  $W$  velocity.

### 6.3.2 Turbulent kinetic energy

Figure 32 shows the profiles of turbulent kinetic energy  $\frac{1}{2}\bar{q}^2 = \frac{1}{2}(\bar{u}^2 + \bar{v}^2 + \bar{w}^2)$  of Ref. [24], (a), compared with those obtained in our simulation, (b). The experimental turbulent kinetic energy profiles are characterized by two peaks, one approximatively located in the core of the CRVP and the other near the core of the HSV. We can see that the shape of the profiles obtained numerically are similar to the experimental ones only in the upper part, i.e. where CRVP are located, especially close to the jet orifice. Conversely, near the wall the shape of the profiles is quite different and in our simulation the effect of the HSV on  $q$  is not present. This can be due to the fact that, with the used mesh, at that location most of the fluctuations are not resolved and thus they are included in the SGS term. More surprisingly, the peaks of  $q$  in the upper part of the profiles, although at the right location

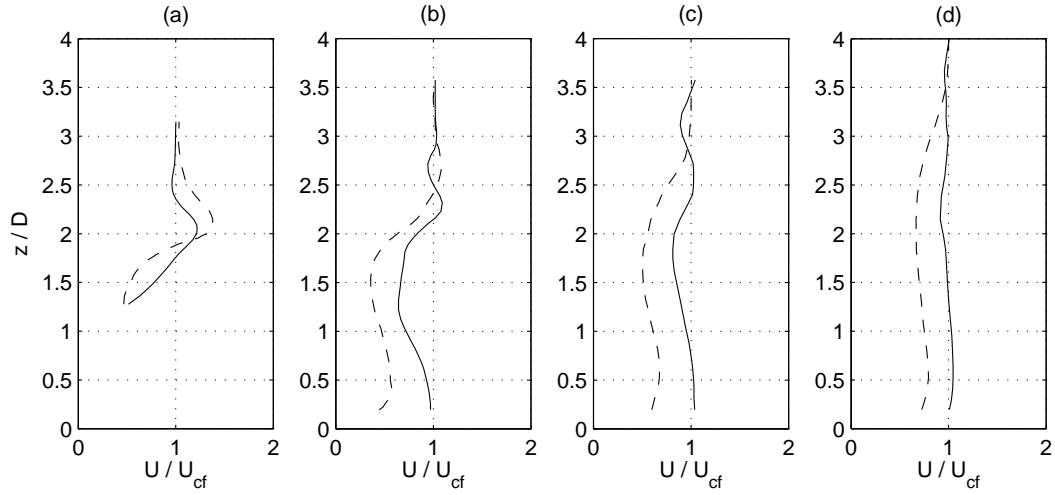


Figure 29: Mean U-velocity for plane constant  $x$ : (a)  $x = 2D$ , (b)  $x = 4D$ , (c)  $x = 6D$ , (d)  $x = 10D$ ; dotted lines represents experimental results, solid lines represents numerical results

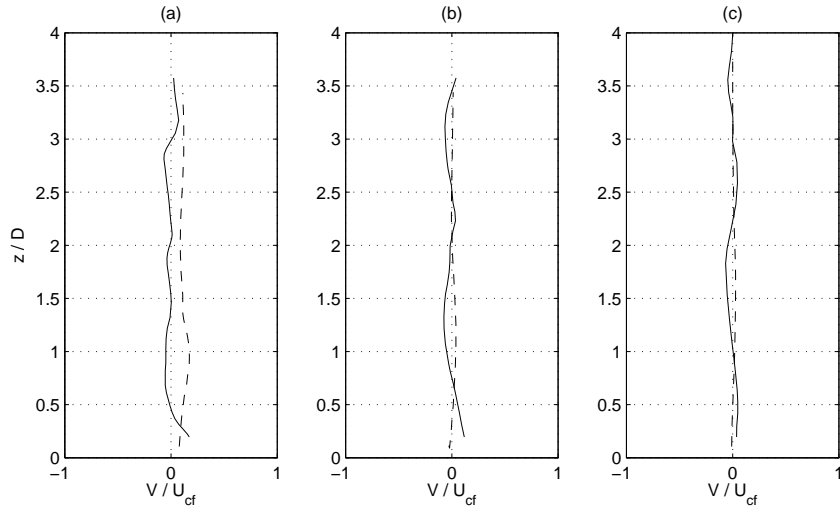


Figure 30: Mean V-velocity for sections at constant  $x$ : (a)  $x = 2D$ , (b)  $x = 4D$ , (c)  $x = 6D$ , (d)  $x = 10D$ ; dotted lines represents experimental results, solid lines represents numerical results



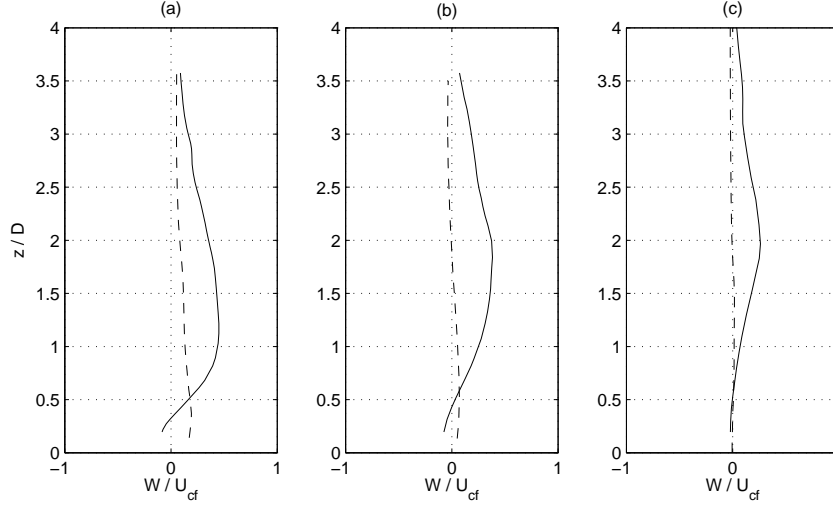


Figure 31: Mean W-velocity for sections at  $x$  constant: (a)  $x = 4D$ , (b)  $x = 6D$ , (c)  $x = 10D$ ; dotted lines represents experimental results, solid lines represents numerical results

for  $x = 2D$  and  $6D$ , are higher than in experiments. This may be due again to the lack of symmetry of the CRVP, which induces significant fluctuations in the considered plane.

### 6.3.3 Turbulent shear stress

For sake of completeness in Figures 33, 34 and 35 the experimental turbulent shear stress profiles, Ref. [24], and the ones obtained with our simulation are reported. It is difficult to compare this results one with the other because our data are referred to the resolved part of the fluctuation, while an important part of the fluctuation, especially near the wall, is included in the SGS term.

## 7 Results of the LNS simulation

### 7.1 Simulation parameters

The results described in the following sections are referred to the LNS simulation of the JICF test case described in Chap. 5. For the LES part, the used SGS model is the Smagorinsky model, while for the RANS the  $k-\epsilon$  model has been used. As for the LES simulation described in Chap. 6, the V6 scheme and implicit time advancing have been employed. For the LNS simulation we have set  $CFL = 10$  and  $\gamma_s = 0.5$ .

As in the LES case the averaged quantities are computed over approximately  $6T$ .

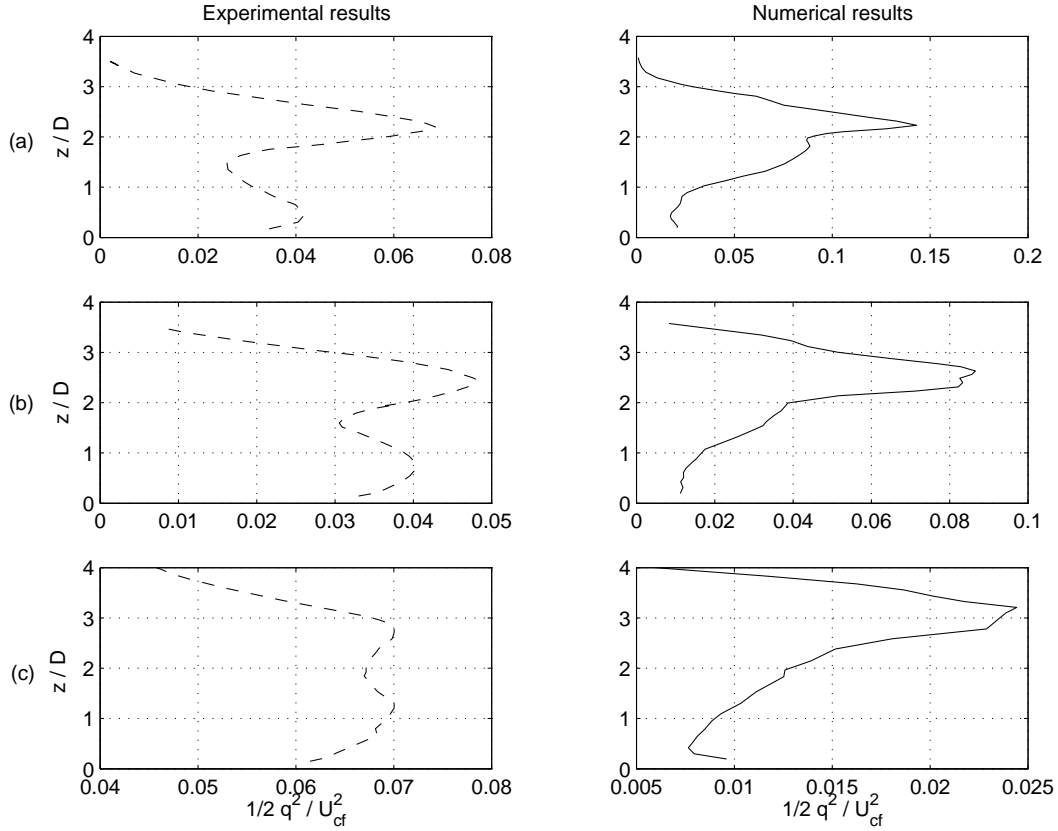


Figure 32: Turbulent kinetic energy for sections at  $x$  constant: (a)  $x = 4D$ , (b)  $x = 6D$ , (c)  $x = 10D$ ; dotted lines stand for experimental results, solid lines stand for numerical results

## 7.2 Reproduction of general flow characteristics

As for the LES simulation, the part of the domain of interest for the post-processing is the zone immediately downstream the jet orifice, approximately before  $x = 10D$ . An important point to investigate for the LNS simulation is the division of the domain between the zone where LES is used and the ones where the RANS model is activate.

Figures 36 and 37 show the damping function,  $\alpha$ , defined as follows:

$$\alpha = \min\left\{\frac{\mu_s}{\mu_t}, 1\right\} \quad (56)$$

where  $\mu_s$  and  $\mu_t$  stand for the SGS viscosity obtained by the LES closure model and the viscosity obtained by the RANS approach respectively. Figure 36 shows the damping func-

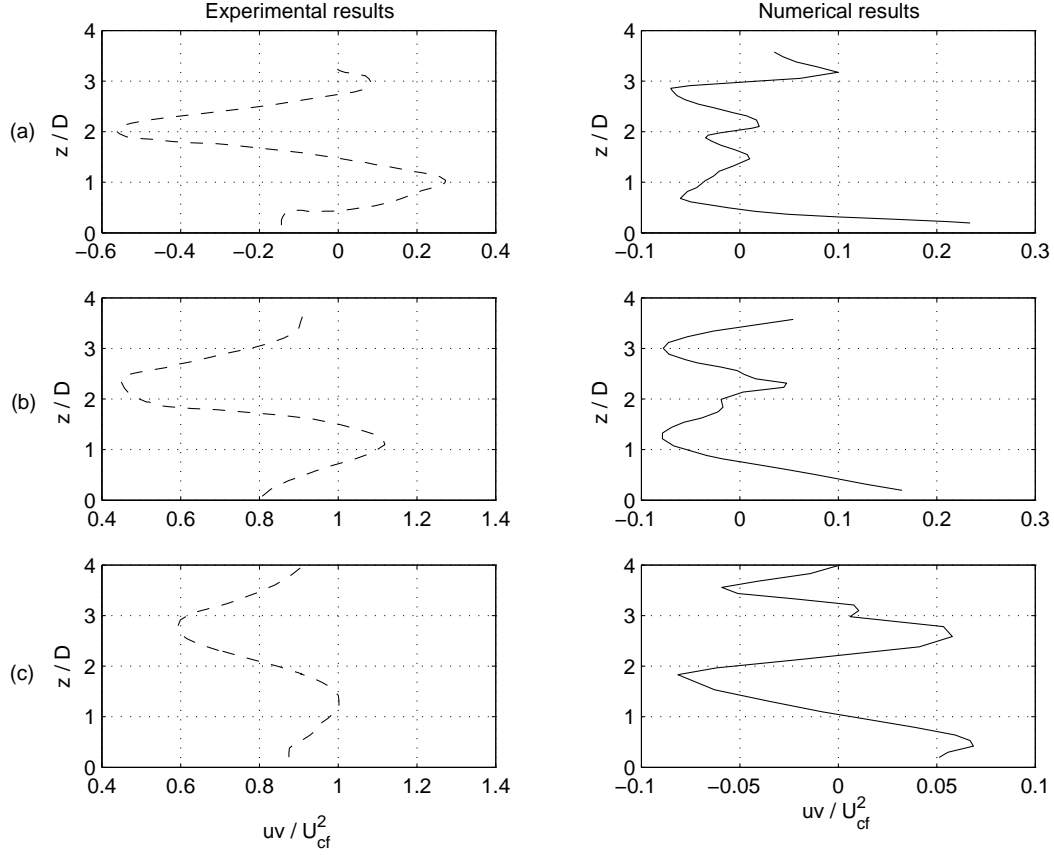


Figure 33:  $\overline{uv}$  shear stress profile for sections at  $x$  constant: (a)  $x = 4D$ , (b)  $x = 6D$ , (c)  $x = 10D$ ; dotted lines represents experimental results, solid lines represents numerical results

tion  $\alpha$  on a plane  $z = 0.001D$  and on sections at  $x = 2D$ ,  $x = 6D$  and  $x = 10D$ . In these the ISO-contours for  $\alpha = 0.95$  are also plotted, which is assumed as the threshold between regions in which the LNS model works in LES mode and those in which RANS is recovered. In Figure 36 and Figure 37, we can see that the RANS equations are solved approximately in all the plane at  $z = 0.001D$ , except the region where the jet orifice is located. It is due to the fact that this plane is inside the cross-flow boundary layer, which is always computed using RANS for both the flat plate and pipe. Only in the middle of the jet on the plane at  $z = 0.001$  LES is used. The RANS closure is also used above the flat plate in the jet shear layers immediately after the jet orifice (upstream  $x = 6D$ ), as shown in Section A

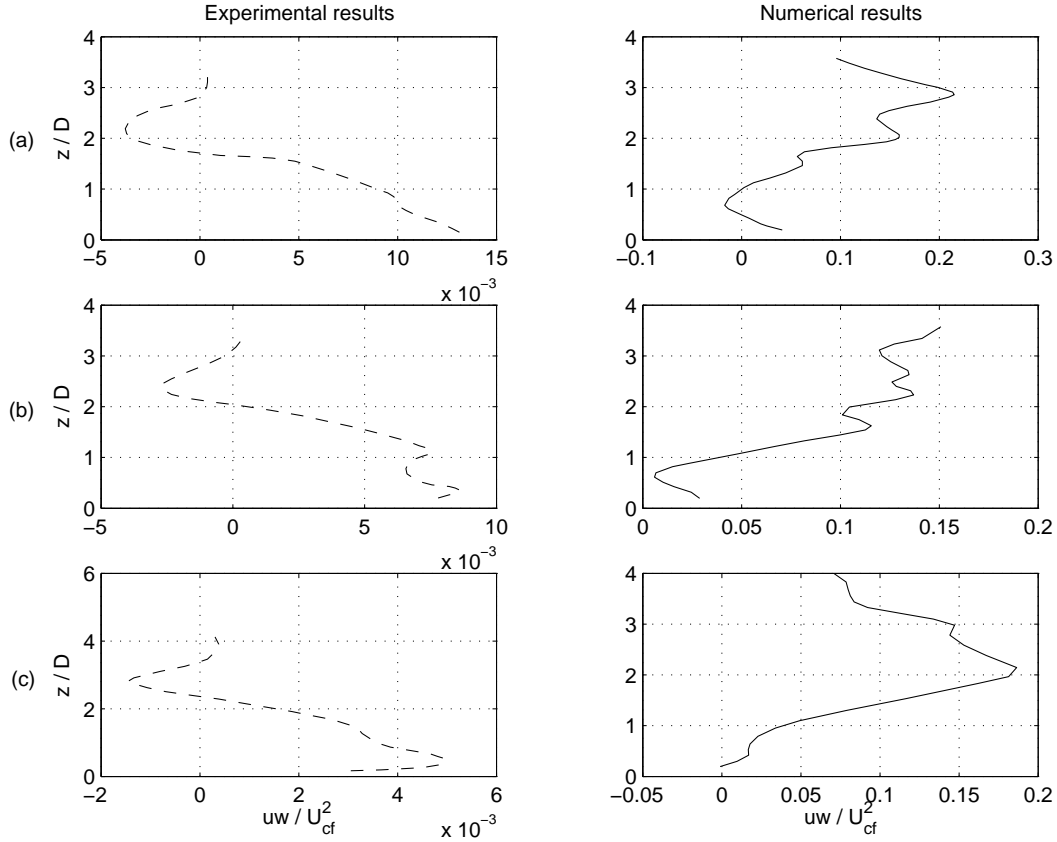


Figure 34:  $\overline{uw}$  shear stress profiles for sections at  $x$  constant: (a)  $x = 4D$ , (b)  $x = 6D$ , (c)  $x = 10D$  ; dotted lines represents experimental results, solid lines represents numerical results

of the Figure 36 and in Figure 37. Moreover, from Figure 37 we can see that, also in the pipe, RANS equations are mainly used, especially in the bottom part of the pipe and in the plenum chamber. In conclusion, we can see that the RANS equations are used where the mesh is not fine enough to give a good description of the mean flow using LES and this is consistent with what was a priori expected.

The boundary conditions at the inlet of both flat plate and pipe for LNS and LES simulation are shown in Figure 38 and Figure 39. Figure 38 shows the component of the velocity in the direction of the axe of the pipe,  $W$ , at  $z = -1D$  upstream the pipe exit. As shown in the figure, the  $W$  velocity obtained using LNS is flatter in the middle of the pipe than the one obtained using LES simulation, so it may be thought as more turbulent. The

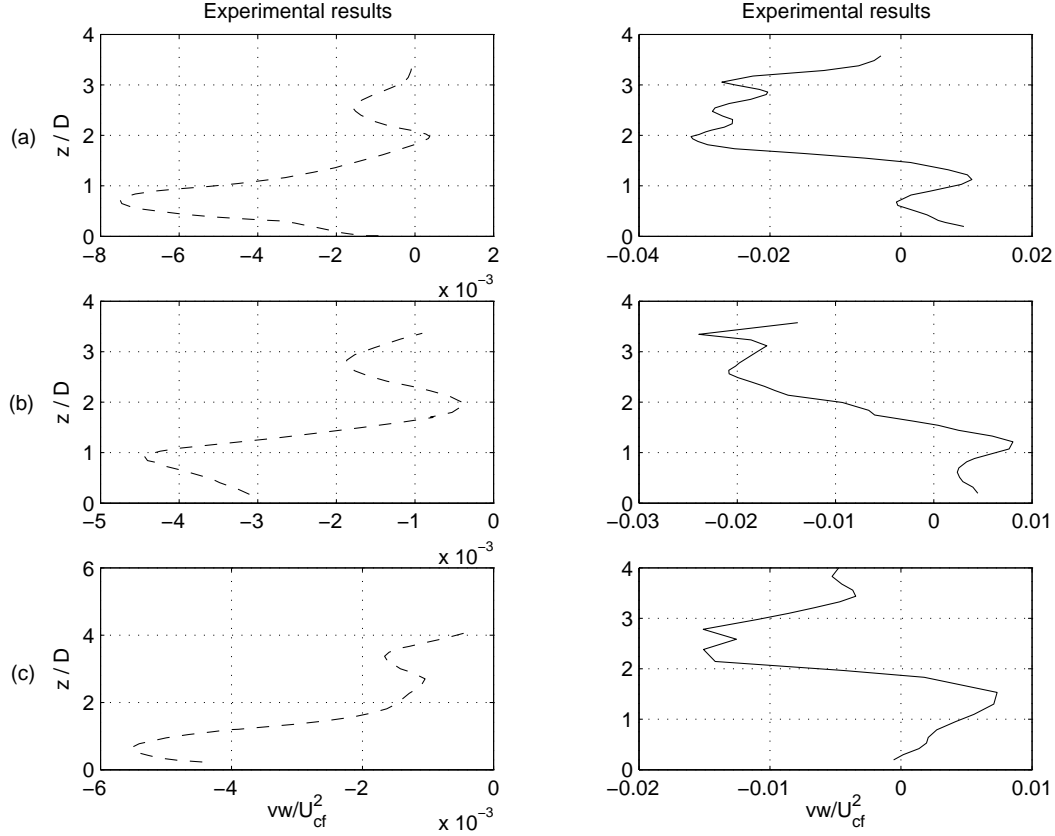


Figure 35:  $\overline{vw}$  shear stress profiles for sections at  $x$  constant: (a)  $x = 4D$ , (b)  $x = 6D$ , (c)  $x = 10D$ ; dotted lines represents experimental results, solid lines represents numerical results

RMS for the LNS case is not characterized by a peak, as it should happen for a turbulent profile, because in the pipe RANS equations are used, so the main contribution to the fluctuations is given by the turbulent kinetic energy,  $k$ , obtained from the  $k-\epsilon$  model used for RANS. Figure 39 shows the flat plate streamwise velocity,  $U$ , at  $x = -4D$  upstream the jet orifice. This profile is quite similar to the one obtained in the LES simulation, but since here RANS is used, we have a smaller asymptotic velocity over the flat plate even if the boundary layer thickness is always smaller of the one in the experiment of Andreopoulos, Ref. [24]. Nevertheless, the velocity ratio,  $R$ , is always approximately 2.

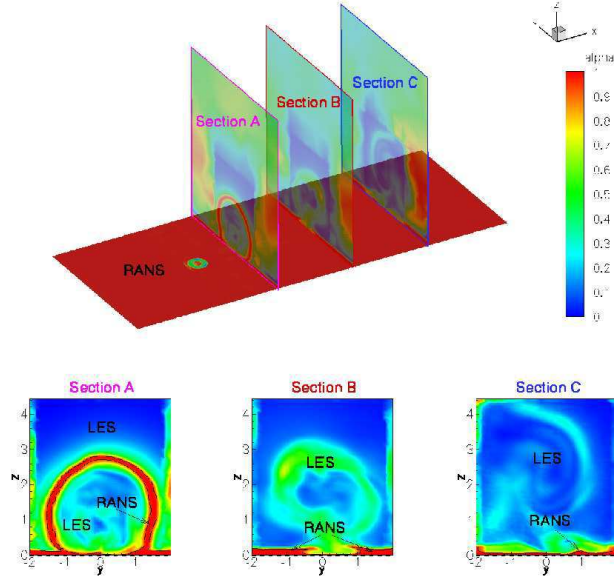


Figure 36: Value of the damping function,  $\alpha$ , in a plane at  $z = 0.001D$  and in the plane at  $x = 2D$  (Section A),  $x = 6D$  (Section B) and  $x = 10D$  (Section C) and ISO-contours for  $\alpha = 0.95$

### 7.2.1 Horseshoe vortex (HSV)

As for LES, we can try to show the HSV by plotting the streamwise component of the vorticity,  $\omega_x$ , on a plane parallel to the flat plate very near to the wall ( $z = 0.001D$ ) and for the sections A, B, C, shown in Figure 40 which are on the planes  $x = 2D$ ,  $x = 4D$  and  $x = 10D$  respectively. We can notice that, in LNS is more difficult to identify the HSV, especially near the jet orifice, i.e. in section A of Figure 40. This is probe to the fact that, as shown in Figure 36, near the wall, where the HSV are located, RANS equations are solved. This region is quite small near the flat plate outlet, i.e. it is quite absent near the jet symmetry plane for  $x = 6D$ , but near the jet orifice it coincides quite completely with the region where the HSV are located. Due to the fact that the RANS approach gives a good description of the mean flow, but a poor description of the fluctuating part of the flow, which are not directly resolved, but are taken into account using the  $k-\epsilon$  model, the instantaneous structures related to the HSV are not well described near the pipe. Conversely they are reproduced in a better way near the flat plate outlet, because there the layer where RANS approach is used is quite small.

As for the LES case, the vorticity obtained in the LNS simulation, is interrupted where the joint between the upstream and downstream structured mesh of the flat plate and the

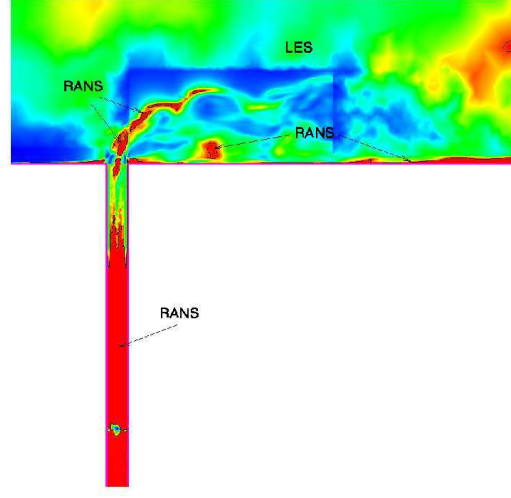


Figure 37: Value of the damping function,  $\alpha$ , in the jet symmetry plane and ISO-contours for  $\alpha = 0.95$

mesh of the pipe is located. This effect is less strong than in LES, as shown in Figure 41, especially for what that concern the vorticity of the HSV, which is described in the figure by the region of high vorticity closer to the pipe exit.

### 7.2.2 Ring like vortices (RLV)

Figure 42 shows the comparison between the RLV obtained using LNS 42(a), and those given by LES computing, Figure 42(b). In the LNS simulation, the vortical structures are not present in the jet boundary layer, upstream the jet orifice. This is due to the fact that, as shown in Figure 37, in these zones the RANS equations are solved, thus, the instantaneous structures, as the RLV, are less well reproduced.

### 7.2.3 Counter-rotating vortex pair (CRVP)

In Figure 43 the averaged streamwise component of the vorticity,  $\omega_x$ , in the same sections described in Section 7.2.1 is shown. We can see that the CRVP, which are represented by the upper concentration of vorticity, are well captured only near the jet orifice and that, already for  $x = 6D$ , they are more diffused than in the LES simulation, see Figure 24. This can be due to the fact that the CRVP originate from the RLV. As described in Section 7.2.2,

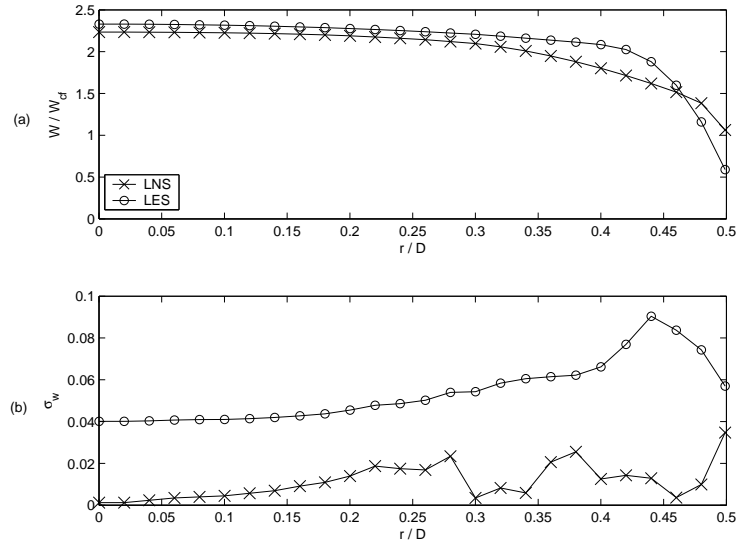


Figure 38: Averaged W velocity profile and RMS for the W velocity in the pipe at  $z = -1 D$ .

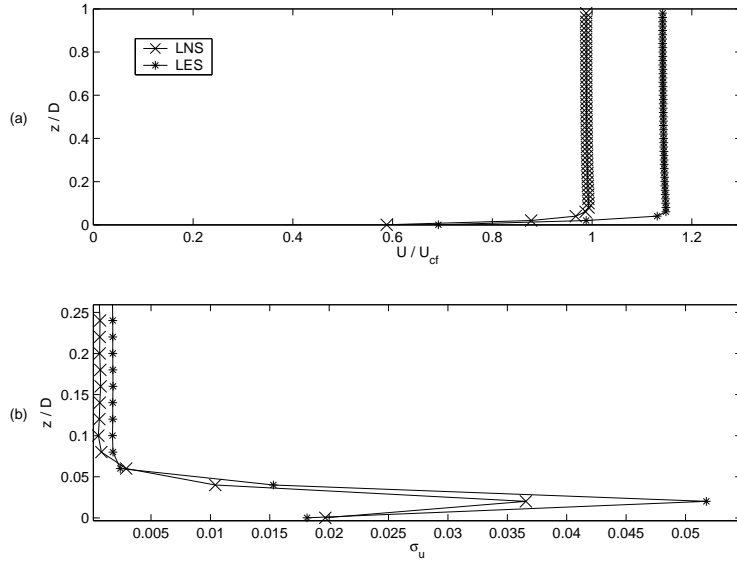


Figure 39: Averaged U velocity profile and RMS for the U velocity in the flat plate at  $x = -4D$ .



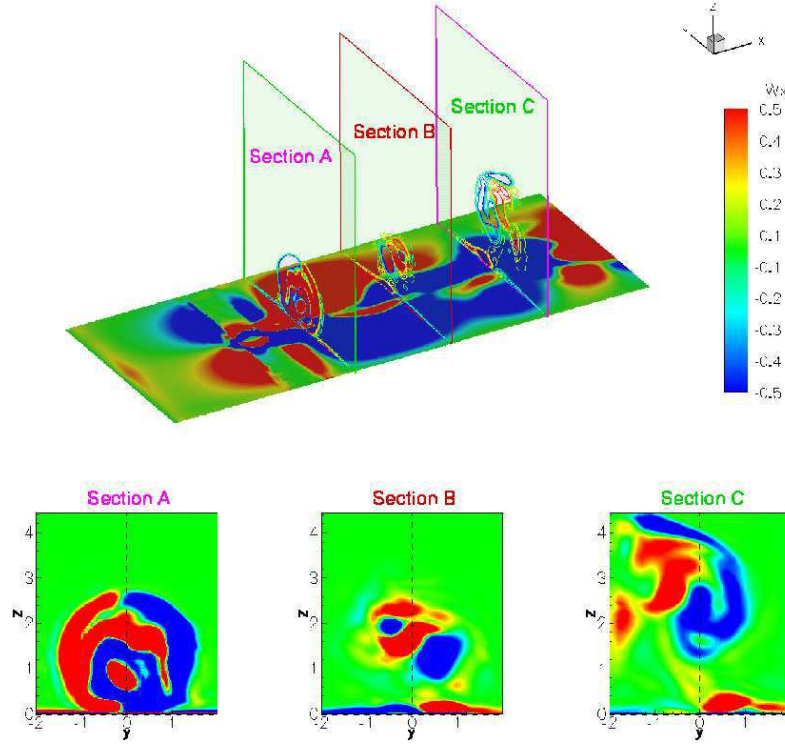


Figure 40: Instantaneous vorticity field on a plane at  $z = 0.001D$  and in some planes in the streamwise direction. Section A, B, C show the vorticity field in a plane at  $x = 2D$ ,  $x = 6D$  and  $x = 10D$  respectively

only their trace on the mean flow is described in the simulation, but not the instantaneous structures. The CRVP are still non symmetric with respect to the jet symmetry plane.

#### 7.2.4 Upright vortices (URV)

As for LES the URV are not present.

### 7.3 Flow statistics

#### 7.3.1 Mean velocities

Figure 44(a) and (b) show the differences between the averaged vertical velocity,  $W$ , obtained using LNS and LES approach respectively. The black points of Figure 44(a) and (b) describe

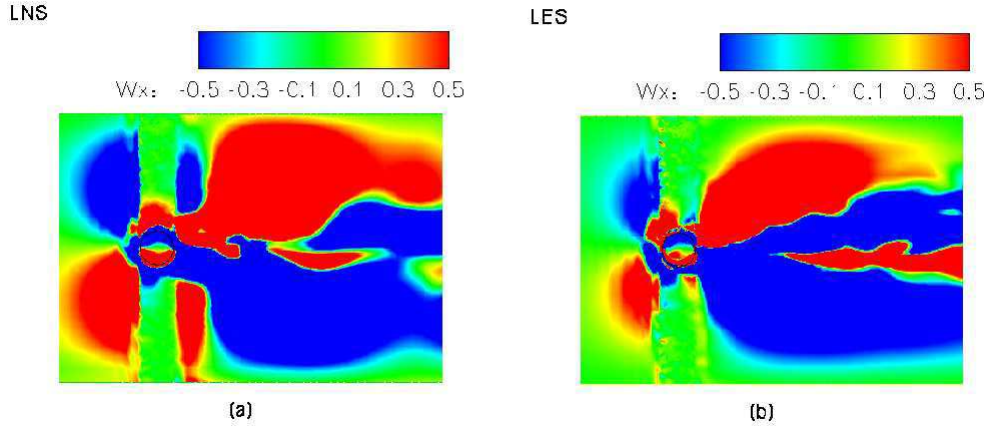


Figure 41: Instantaneous vorticity field on a plane at  $z = 0.001$  for both LNS (a) and LES (b) computing

the axis of the jet, defined as the locus of the maximum velocity, computed using LES, while in Figure 44(b) the grey squares show the axis of the jet obtained using LNS. We can see that the one given by LNS is above the one obtained in LES. This may be due to the fact that, as described in Section 7.2.2, the instantaneous structures related to the RLV are not reproduced. It means that we have less mixing between the jet and the cross-flow and thus the axis of the pipe is less bended. at the exit of the pipe are smaller. Moreover, if the LES approach is used in the whole domain, the jet is more spread, as we can see following the streamlines which originate from the pipe, described in Figure 42.

Figure 44 (a) and (b) are similar each other upstream the jet exit, but they are quite different more downstream. If we analyze the the LNS results we can see that immediately after the jet shear layers we have a region characterized by a downward velocity which is not present in the LES results. This is related to the presence of the vorticious structures, located downstream the jet orifice, shown in Figure 42 and which are not present in LES. These vortices can be related to a sort of recirculation bubble that is formed behind the jet . If LNS approach is used, as we have previously pointed out, the jet is less bended and spread, so the jet is, from the cross-flow point of view, more similar to a circular solid cylinder, than in the LES simulation. If we have a solid cylinder, we would have a recirculation bubble after the body, typical of buff bodies. In the JICF case we should obtained something similar, but disturbed by the fact that the jet is bended by the cross-flow. Indeed, in LES, the jet is more diffused after the pipe exit and is more bended, thus this sort of recirculation bubble is quite small, as shown in Figure 45(b), which reports the streamlines which originate before the jet orifice on a plane at  $z = 0.5D$ . The LNS approach is used, instead, the recirculation

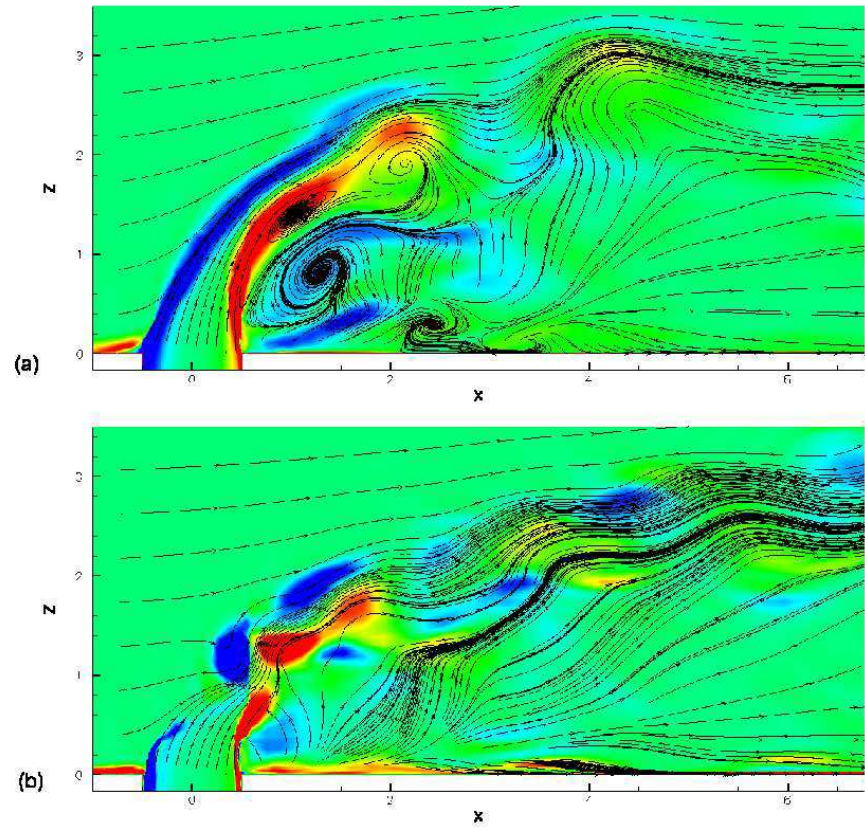


Figure 42: Streamlines instantaneous transverse component of the vorticity in the jet symmetry plane

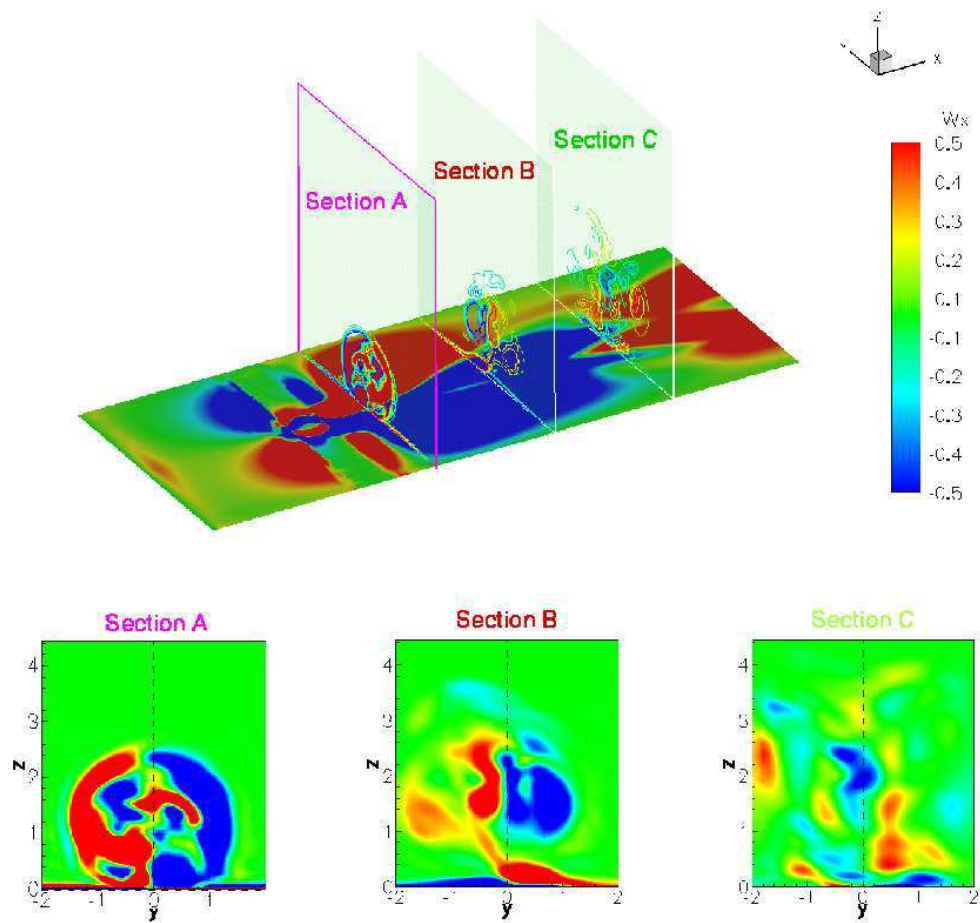


Figure 43: Averaged vorticity field on a plane at  $z = 0.001$  and on some sections at  $x$  constant ( $x = 2$  section A;  $x = 6$  section B;  $x = 10$  section C)

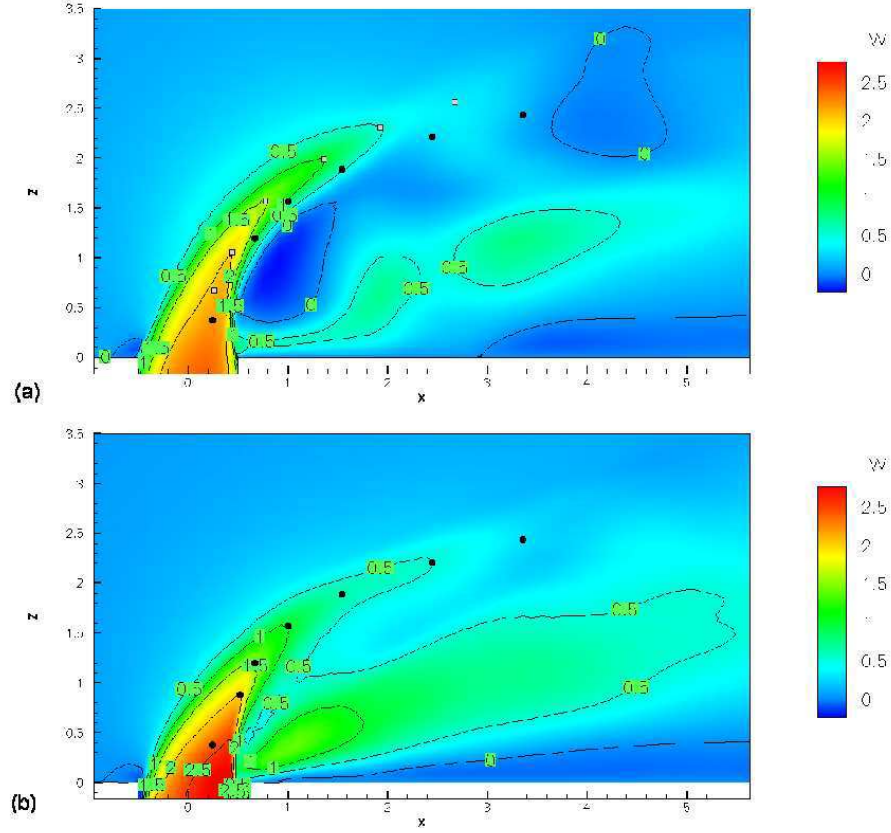


Figure 44: Time-averaged vertical velocity in the jet symmetry plane

bubble is larger, 45(a). The streamlines have a shape more similar to that of the streaklines obtained experimentally by Roshko, Ref. [29], (see Figure 6) in the LES case.

Figure 46 shows the mean streamwise velocity obtained using LNS, (a), and LES, (b) respectively. As for the vertical velocity, the streamwise velocity fields obtained with the two approaches are quite different due to the presence of the recirculating structures behind the jet in the LNS case.

Qualitatively Figure 44(b) and 46(b) are more similar to the Figures 32 and 33 shown by Yuan in his work, but these are obtained using different parameters.

In Figure 47, 48 and 49 the averaged streamwise, transverse and vertical velocity profiles obtained with LNS, LES and by Andreopoulos in his experiments, Ref. [24] are shown. We can note that LES results are mainly closer to the experimental data than the LNS results.

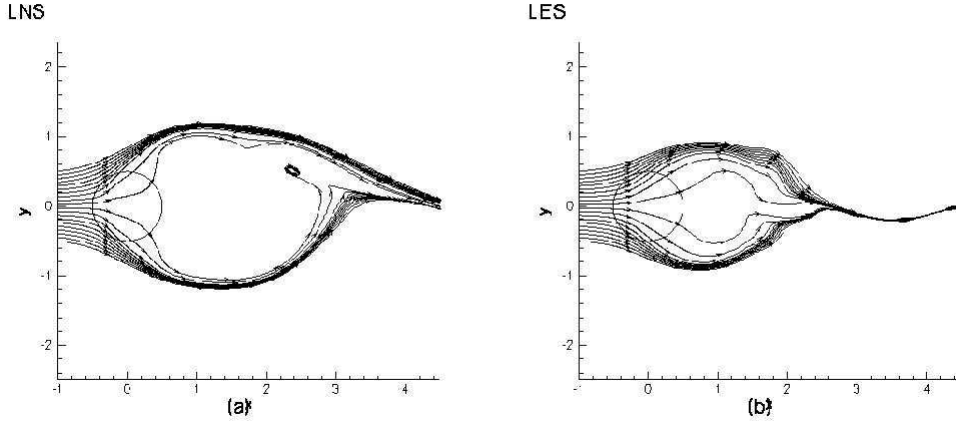


Figure 45: Streamlines with originate upstream the jet orifice in a plane  $z = 0.5D$  obtained by LNS, (a), and LES computing, (b)

We can see from Figure 47 that, especially near the jet orifice, Figure 47(a), the stream-wise velocity profile obtained with LES is nearer to the experimental data than the LNS one. It means that, as we have already pointed out from qualitative comparisons, the recirculation bubble obtained with LNS is too large and the structures present in the LNS case are due only to the coarseness of the mesh. Indeed, for the LNS case we have, especially near the jet orifice downstream the jet, quite big errors especially near the wall and these are due to the presence of the vortical structures previously described. Thus, quantitative results are in agreement with the qualitative shape of the velocity field and of the streamlines. More downstream, instead, LES and LNS results are in agreement and the flow acts, in both cases, as if the jet was not present.

The transverse velocity obtained with LNS simulation, see Figure 48 is approximately close to the one obtained with LES and is globally not very far from the experimental results.

The vertical velocity on the plane at  $x = 4D$ , Figure 49 (a), is closer to experimental data near the jet orifice because there, in the LNS, the CRVP seem to be more symmetric, but downstream  $x = 6D$  we have essentially the same results for both LES and LNS case.

### 7.3.2 Turbulent kinetic energy and turbulent shear stress

Figure 50 shows the turbulent kinetic energy on the jet symmetry plane. We can see that the results for LES and LNS are quite similar, only for  $x = 10D$  using LNS approach the double peaks are described. We have again bigger value of the kinetic turbulent energy as for the LES case.



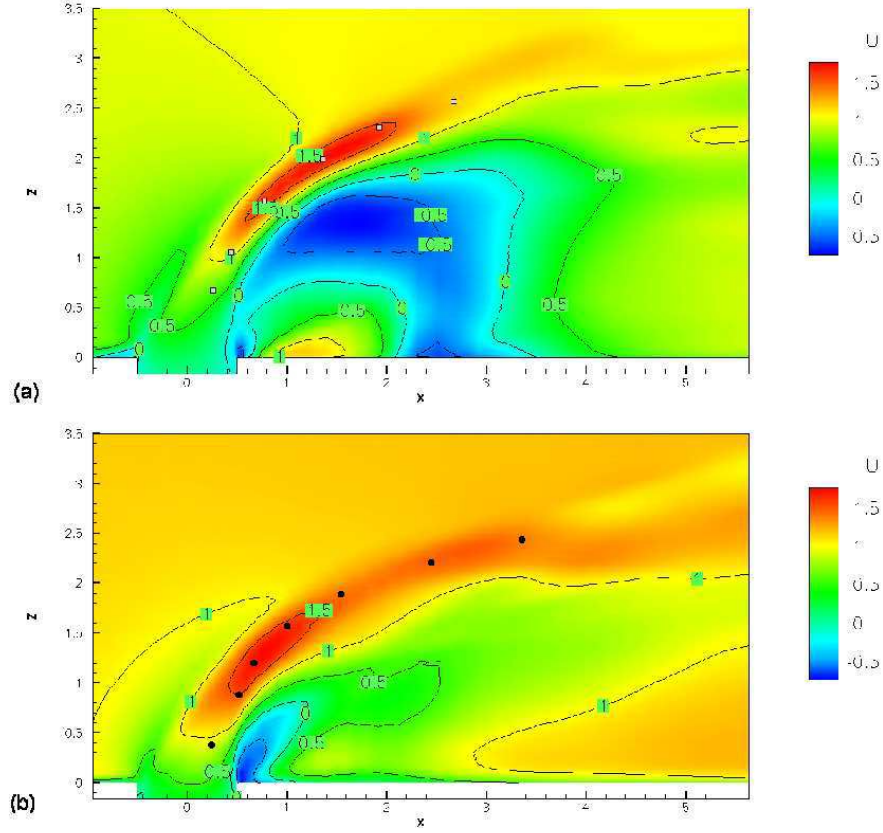


Figure 46: Time-averaged streamwise velocity in the jet symmetry plane

Figure 51, 52, 53 are included for sake of completeness and show the shear stresses.

## 8 Grid results

### 8.1 Computational resources

The computational resources used to compute the JICF have been classical parallel computers and Grid Computing. The classical parallel computer used is the CINES (National Computer Centre of Higher Education) located in Montpellier (France), with 768 processors R14000+/500 mhz. This computer has a theoretical performance peak of 512 Gflops. Grid Computing of the MecaGRID project is also carried out (see Section 4.2) for more

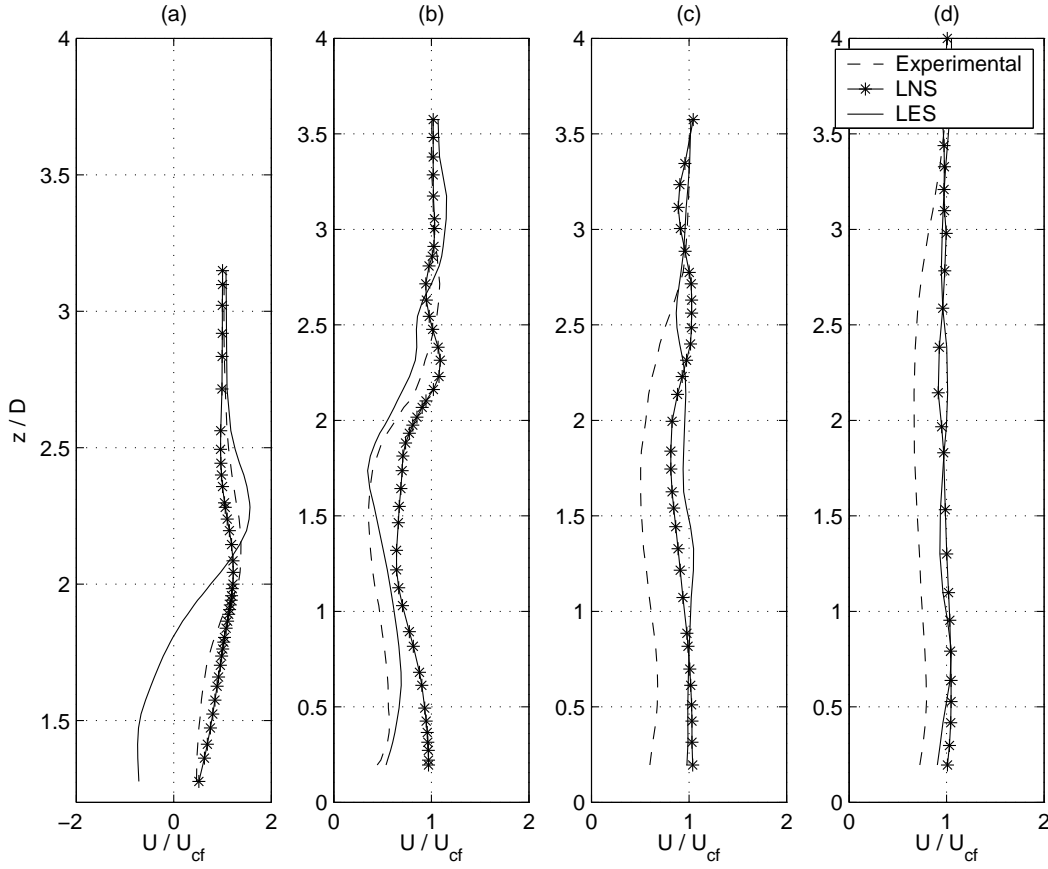


Figure 47: Mean U-velocity; dotted lines represents experimental results, solid lines represents numerical results

details. For this work, only the computers of the INRIA Sophia-Antipolis and IUSTI were used, because of technical problems. In this section we describe the performance obtained with the two systems for the LES simulation of the JICF test case, described in Section 5, and for the flow in a pipe similar to the one present within the JICF, but shorter and characterized by a finer mesh.

## 8.2 Pipe with 241K vertices

We describe now the performance of Globus obtained in the LES simulation of the flow in a pipe similar to the one present in the jet in crossflow test case (see Section 5.3) but 5D



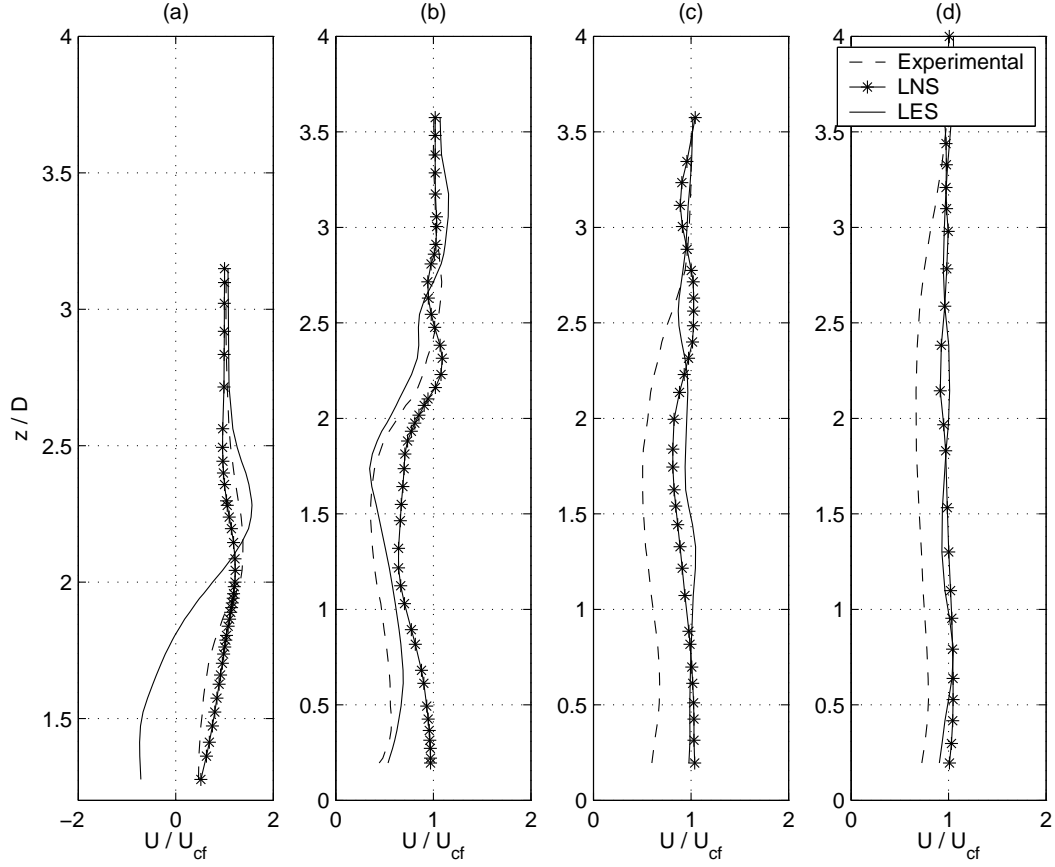


Figure 48: Mean V-velocity; dotted lines represents experimental results, solid lines represents numerical results

long. The mesh used is shown in Figure 54 and contains 241000 vertices. The simulation is carried on using AERO code (see Section 3) using implicit time advancing.

Due to the fact that the performance of Globus are influenced by the speed of the net, which are not constant in time, all data are referred to Globus are the mean computed over three different runs, carried out using the same parameters.

In Table 4 the performance of grid computing for different combinations of the Meca-GRID cluster is summarized and the compared with the runs on the CINES computer, for 100 iterations. NINA and PF stands for the computers of the cluster of the INRIA Sophia Antipolis and IUSTI stands for the cluster of IUSTI. The main characteristics of these com-

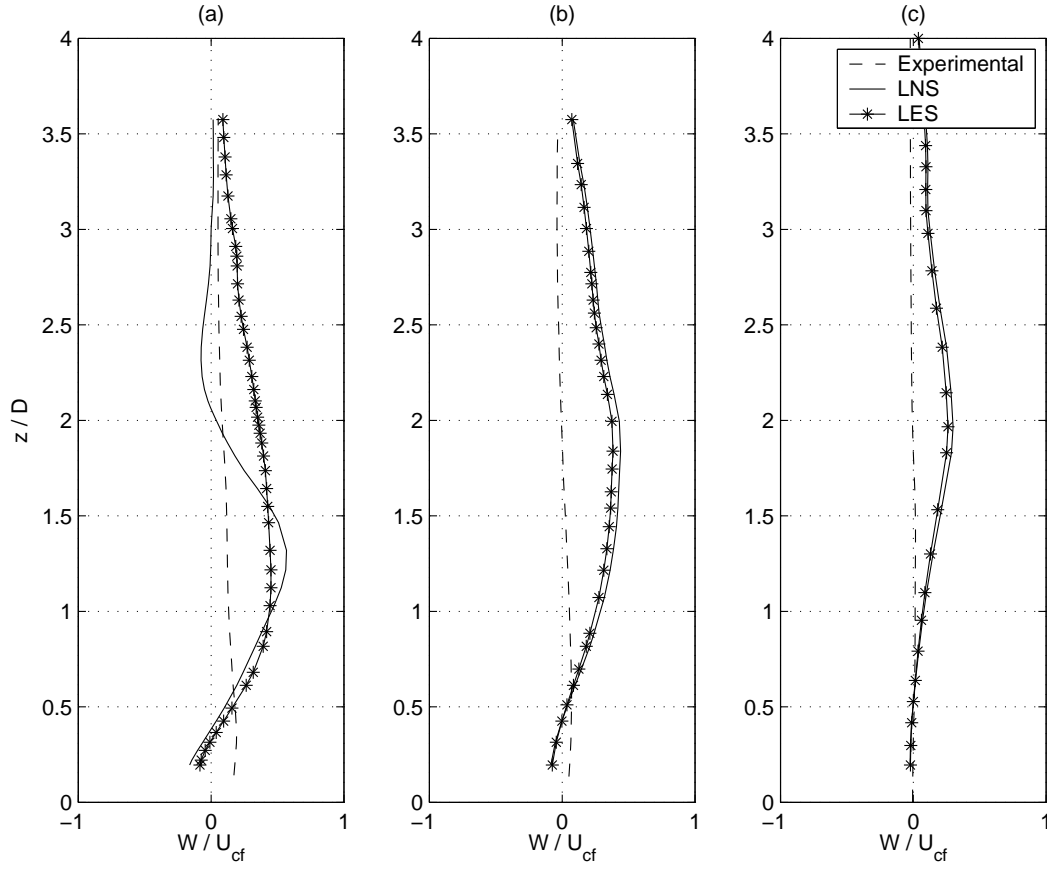


Figure 49: Mean W-velocity; dotted lines represents experimental results, solid lines represents numerical results

puters are described in Table 2. The Communication/Work ratio,  $CW$ , is the ratio between the total communication time,  $TC$ , and the Work,  $W$ :

$$CW = \frac{C}{W} \quad (57)$$

where  $W$  is the difference between the total computational time,  $TCpT$ , and the total communication time,  $TCmT$ :

$$W = TCpT - TCmT = TCpT - (LICT + GICT) \quad (58)$$

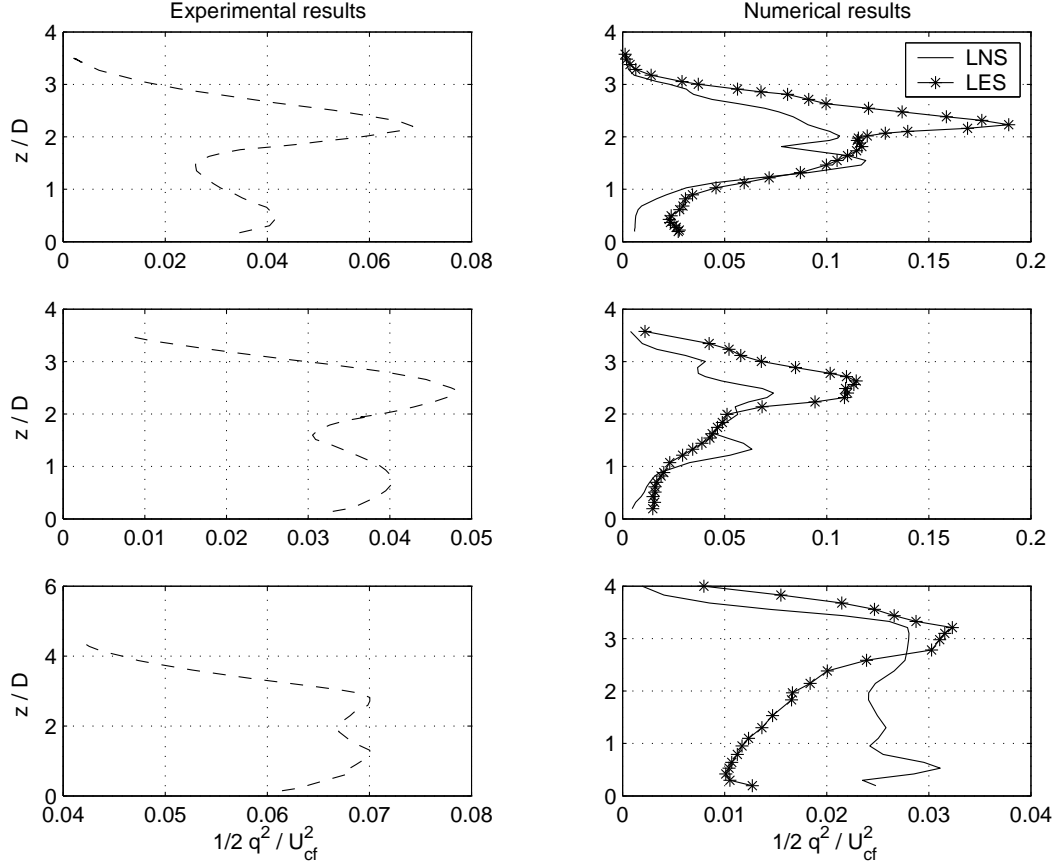


Figure 50: Turbulent kinetic energy for sections at  $x$  constant in the jet symmetry plane: (a)  $x = 4D$ , (b)  $x = 6D$ , (c)  $x = 10D$ ; dotted lines represents experimental results, solid lines represents numerical results

where  $LICT$  is the local inter-communication time and  $GICT$  is the global inter-communication time

We can notice that in this case globus (NINA-PF-IUSTI case and NINA-IUSTI case) gives the worst performance, but if all processors with high speed are used, as in the case in which NINA processors and IUSTI processors are used, the computational ratio is not very different from the one obtained using all processors located at the INRIA. We have not introduced the results related to the performance of only nina processors because, due to the number of this kind of processors present in the cluster of the INRIA, it is very difficult

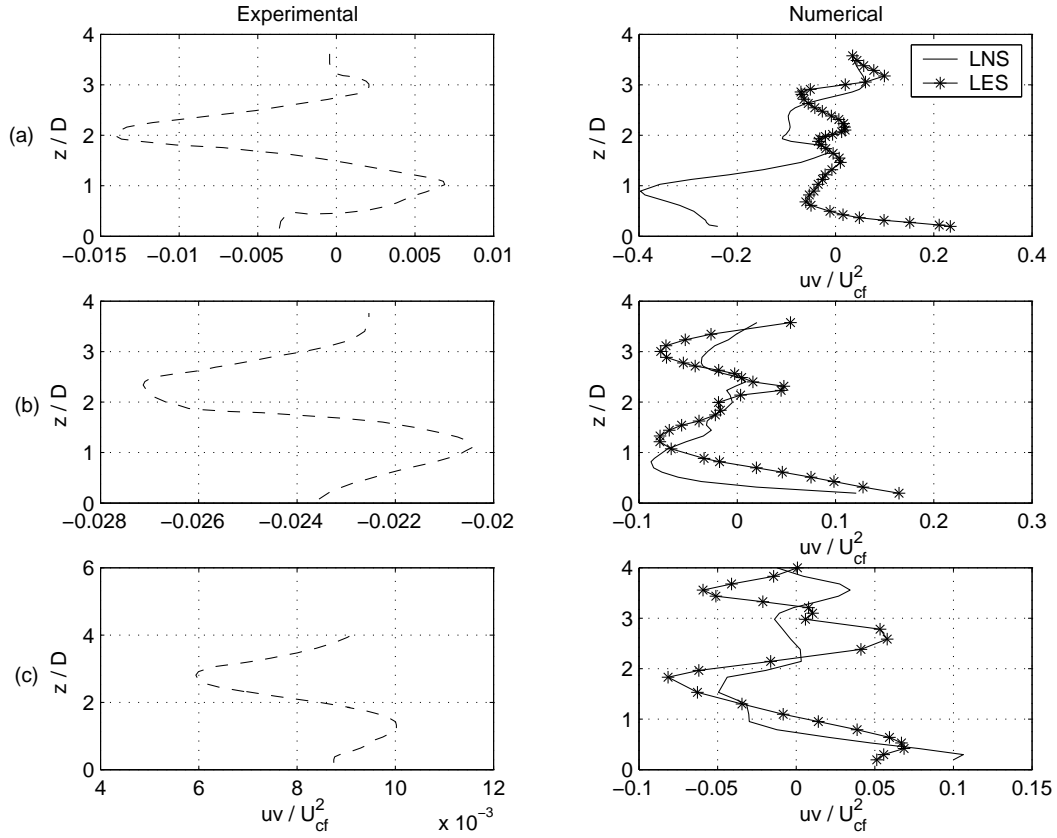


Figure 51:  $\overline{uv}$  shear stress profile for subsections at  $x$  constant: (a)  $x = 4D$ , (b)  $x = 6D$ , (c)  $x = 10D$  in the jet symmetry plane; dotted lines represents experimental results, solid lines represents numerical results

to have all the needed processors available. This is, indeed, one of the big advantages of using GRID, i.e. that allows a large number of processors from different sites to be used in a single run.

### 8.3 JICF with 398K vertices

In this section the performances of Globus using the mesh of the JICF test case described in Section 5.3 is presented. The simulations are carried out using an explicit time advancing scheme. In Table 5 the results obtained using 32 partitions to compute 100 iterations are shown.

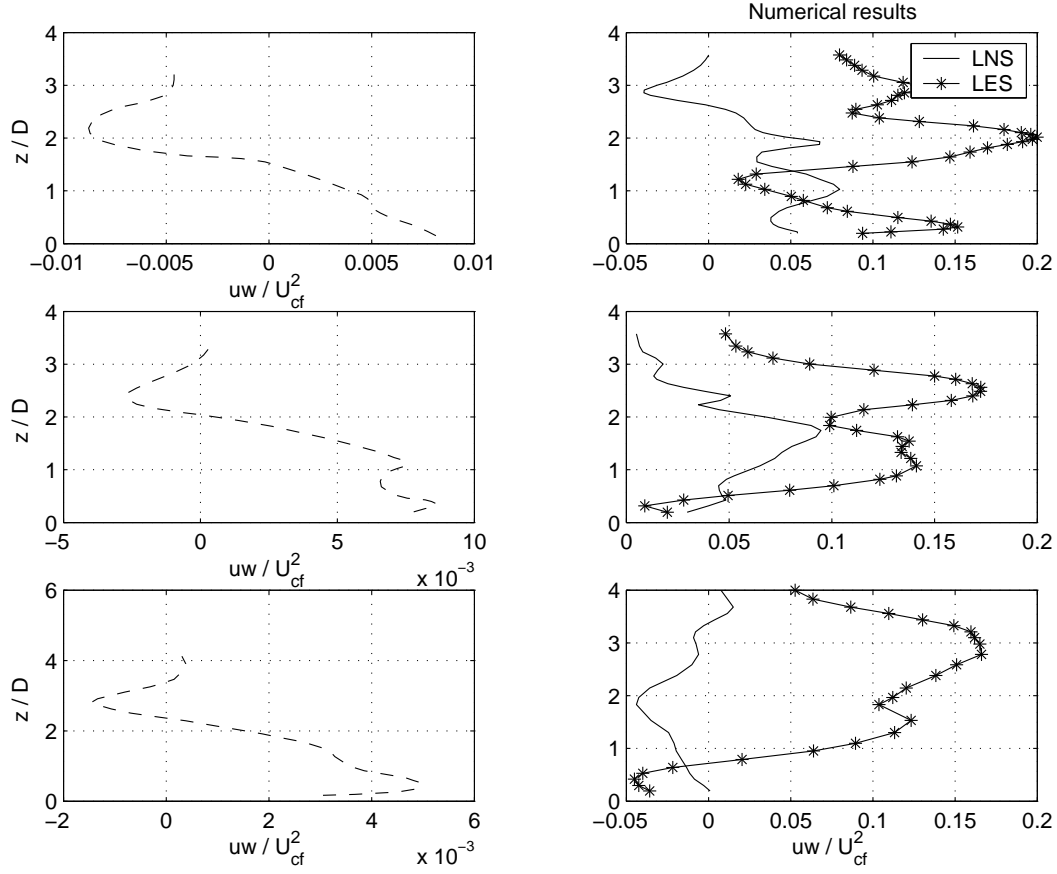


Figure 52:  $\overline{uw}$  shear stress profiles for subsections at  $x$  constant and for  $y = 0.5$ : (a)  $x = 4D$ , (b)  $x = 6D$ , (c)  $x = 10D$ ; dotted lines represents experimental results, solid lines represents numerical results

We can see that in this case Globus, combining NINA and IUSTI processors, gives the best results. This can be due to several reasons. First of all explicit runs are used. It reduces the complexity of the problem to be solved and in particular the number of information to be exchanged. Another point which may influence the results is the geometry of the test case analyzed. The area where the interface between the pipe and the crossflow is located is quite small, thus, if the information is exchanged only for this zone, the number of communications decreases. Indeed, one of the main problems of Grid Computing is the communication between sites located in different places. To exchange information the web

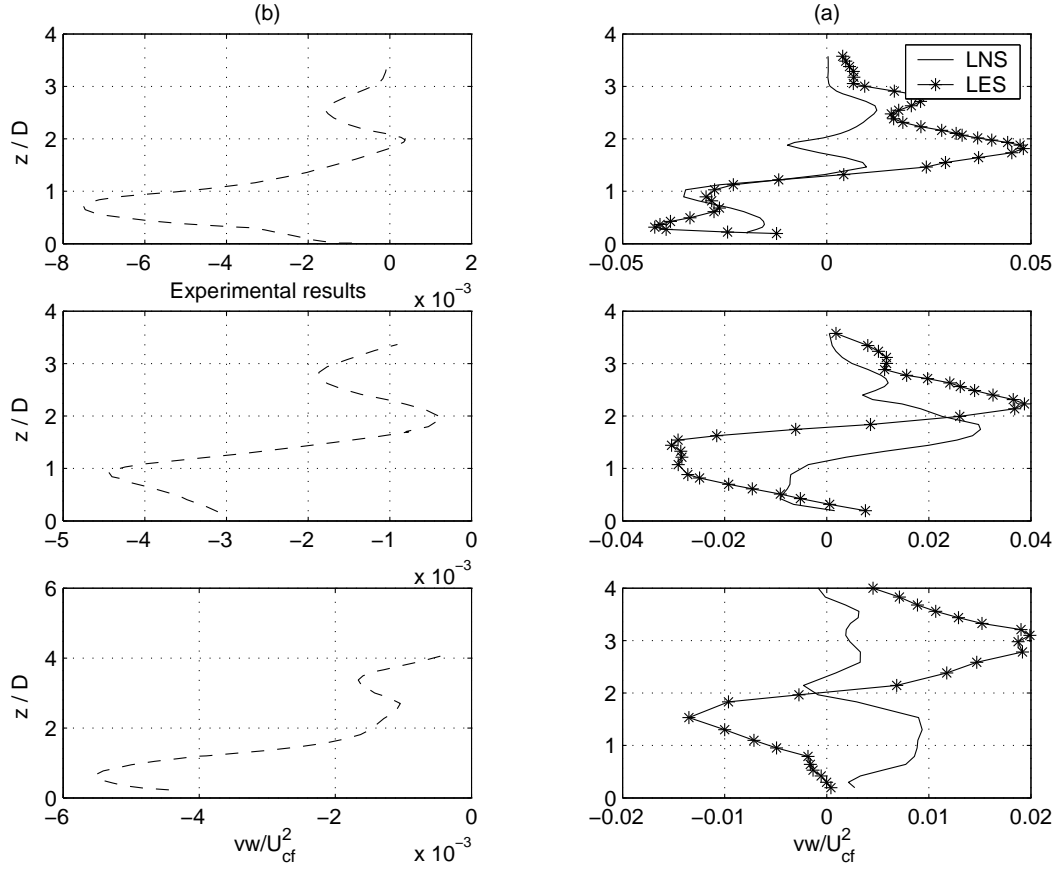


Figure 53:  $\overline{vw}$  shear stress profiles for sections in at  $x$  constant and for  $y = 0.5$ : (a)  $x = 4D$ , (b)  $x = 6D$ , (c)  $x = 10D$ ; dotted lines represents experimental results, solid lines represents numerical results

is used, but this kind of communication is quite slow in comparison with the data rate that can be exchanged with a local net.

Table 6 shows the results, obtained with Globus, for two runs related to the JICF case carried out using the same mesh, partitionated with 38 and 48 processors. With the increase of the number of processors the computational ratio increases. Increasing the number of the processors the charge at each processor decreases, but the communication exchange increases. The overall computational time may increase or decrease, depending on the balance between these two effects. The fact that in our simulations the computational time increases if we



Figure 54: Mesh of the pipe used for the Grid Computing

Name of cluster	<b>CINES</b>	<b>NINA-PF</b>	<b>NINA-IUSTI</b>	<b>NINA-PF-IUSTI</b>
Processor speed [GHz]		2/1	2/2	2/1/2
Cache(K)[GHz]		512/256	512/512	512/256/516
Executable size [MB]	523	523	523	523
Number of processors	32	16-16	16-16	16-16
Total computational time	594.38	729.93	817.01	1181.93
Local intra-commun. time	32.21	77.07	234.14	227.14
Global intra-commun. time	14.92	53.46	238.24	302.49
Computational ratio	1.00	1.23	1.37	1.99
Communication/Work	0.03	0.09	0.69	0.46

Table 4: Comparison between Globus performance (GRID), CINES and CLUSTER of Inria Sophia-Antipolis, for a pipe using 32 processors, implicit case

pass from 32 to 48 processors means that the second effect is more important, as could be expected since the cost of communications is critical for Grid Computing.

## 9 Conclusions

In the present work, two different simulations of a JICF configuration have been carried out. The first one is based on a LES approach to turbulence, while the latter employs a hybrid RANS/LES method based on the LNS criterion. Both simulations have reproduced

Name of cluster	<b>NINA-PF</b>	<b>NINA-IUSTI</b>	<b>NINA-PF-IUSTI</b>
Processor speed [GHz]	2/1	2/2	2/1/2
Cache(K)[GHz]	512/256	512/512	512/256/516
Executable size [MB]	432	432	432
Number of processors	16-16	16-16	8-8-16
Total computational time	827.34	728.87	965.55
Local intra-commun. time	63.87	283.28	224.99
Global intra-commun. time	7.39	51.13	40.75
Computational ratio	1.00	0.88	1.17
Communication/Work	0.01	0.13	0.06

Table 5: Comparison between Globus performances (GRID), CINES and CLUSTER of Inria Sophia-Antipolis, for the JICF test case partitioned in 32 processors, explicit case

Number of processors	<b>32-proc</b>	<b>48-proc</b>
Number of nina processors	8	12
Number of pf processors	8	12
Number of IUSTI processors	16	24
Total computational time	935.69	1047.98
Local intra-commun. time	230.40	288.29
Global intra-commun. time	40.75	83.33
Computational ratio	1.00	1.12
Communication/Work	0.06	0.12

Table 6: Comparison of the Globus performances , using 32-partitions or 48-partitions, explicit case

the structures of the flow which have a trace in the mean field, i.e. the CRVP, even if they are damped downstream the jet orifice. HSV are qualitatively well captured only in the LES simulation, while with LNS, especially near the jet orifice, they are not accurately described. RLV are well described with LES, while only a trace on the mean flow is reproduced with LNS. The inability to capture these structures in the LNS case is due to the fact that in the flat plate boundary layer and in the jet shear layers, where HSV and RLV are approximatively located, RANS approach is used. This approach usually gives a good description of the mean flow, but it tends to damp the fluctuations also in its unsteady version. The fact that instantaneous structures connected to the RLV are not captured influences the development of CRVP which originate from RLV. Moreover, the absence of RLV involves a lack of mixing between jet and cross-flow which gives a less bending of the jet axis and a less spreading than the in the LES simulation. Due to the fact that, from the cross-flow point of view,



the jet is similar to an obstacle, if the jet is less bended and spread, it is more similar to a solid cylinder. Thus implies that the recirculation bubble, which is formed behind the jet, is larger than in LES and in experiments and that behind the jet are present some structures that are not present in the experiments. Consequently, in these regions the velocity profiles are less close to the experimental results than those obtained in LES.

The results obtained in the LES simulation are qualitatively more similar to the experimental results than the ones obtained with LNS. The largest errors are present near the wall, where the mesh is not fine enough to accurately capture the HSV vortices. Downstream the jet orifice, near the flat plate outlet, the flow obtained in the simulations is quicker than in the experiments and, near the wall, it acts as the jet was not present. This is still due to the coarseness of the mesh especially near the wall. Moreover the presence of a preferential direction in the grid, due to the fact that the tetrahedron of the mesh are all cut in the same direction, makes CRVP not perfectly symmetric. This gives a significant vertical component of the velocity on the jet symmetry plane, which is not found in the experiments.

The errors in the mean velocity profiles can be also due to the different inflow conditions between simulations and experiments and to the value of the velocity ratio that, which is not exactly 2. In the future the Reichardt velocity profile can be used as inflow condition for the cross-flow and a finer mesh especially near the wall should be used.

As for Grid Computing, we have obtained good results in the simulation of JICF, for which Grid Computing has been found to work better than classical clusters. This can be due to the geometry of the test case, which is particularly suitable for this kind of computing, or to the fact that explicit time advancing was used, which needs less data exchange. Indeed, the main problem in Grid Computing is the exchange of communications between processors located in different sites, which is realized through the web. Conversely, the main advantage of Grid Computing is the possibility to use a large number of processors, using existing processors allocated in different sites. For example, to run the JICF simulation, we have used 32 processors and we had some problems in carrying out the simulation using only the cluster of the INRIA, because the quantity of memory per node needed for our simulation was available only for one kind of processors, the nina processors, present in the INRIA cluster in a limited number. Thus, to have 32 nina processors simultaneously available was quite impossible. Conversely, with Grid Computing we can bypass this problem using powerful processors allocated in different sites.

**Acknowledgements:** This work was permitted by the support of MecaGRID, Italian-French exchange programme of Région Provence-Alpes Côte d’Azur, and the access to the CINES computers.

## References

- [1] I. Abalakin, M. Braza, S. Camarri, A. Dervieux, B. Koobus, T. Kozubskaya, P. Rodes, M.-V. Salvetti, Unstable and unsteady aerodynamics : compared information from different numerical models, INRIA research report, 4077, 2000,

- <http://www.inria.fr/RRRT/RR-4077.html> in “Fluid Dynamics and Aeronautics: new challenges”
- [2] R. Peyret, *Handbook of computational fluid mechanics*, Academic Press, 2004
  - [3] A. N. Kolmogorov, *The local structure of turbulence in incompressible viscous fluid for very large Reynolds numbers* Dokl. Akad. Nauk SSR30, 299-303
  - [4] S. Camarri, *Modelli di ordine ridotto per la simulazione di flussi turbolenti*, Tesi di dottorato, Dipartimento di Ing. Aerospaziale, L. Lazzerino, Pisa
  - [5] J. Jones, B. Launder, *The prediction of laminarization with a two-equation model of turbulence*, Int. J. Heat and Mass Transfer (1972), vol. 15, pp. 301-314.
  - [6] P. Batten, *LNS - an approach towards embedded LES*, AIAA Paper 2002-0427 (2002), American Institute of Aeronautics and Astronautics.
  - [7] J. Smagorinsky, *General circulation experiments with the primitive equations. I. The basic experiment*, Mon. Weather Rev.91(1963)99.
  - [8] P. R. Spalart and A. Leonard, *Direct numerical simulation of equilibrium turbulent boundary layers*, in Proc. 5th Symp. on Turbulent Shear Flows, Ithaca, NY, 1985
  - [9] T. S. Lund, X. Wu, K. D. Squires, *Generation of turbulent inflow data for spatially developing boundary layer simulations*, J. of Computational Physics (1998), vol. 140, pp. 233-258.
  - [10] P. Batten, U. Goldberg, S. Chakravarthy, *Interfacing statistical turbulence closures with large eddy simulation*, AIAA Journal (2004), Vol.42, No.3, March, pp. 485-492.
  - [11] P. Batten, U. Goldberg, S. Chakravarthy, *Reconstructed sub-grid methods for acoustics predictions at all Reynolds numbers*, AIAA Journal 2002-2511 pp. 1223-1231
  - [12] R. H. Kraichnan, *Diffusion by a Random Velocity Field*, Physics of Fluids (1970), Vol.13 No.1, Jan, pp.22-31.
  - [13] A. Smirnov, S. Shi, I. Celik, *Random flow generation technique for Large Eddy Simulations and Particle-dynamic modeling*, J. of Fluid Eng. (2001), vol. 123, pp 359-371 .
  - [14] S. Basu, E. Foufoula-Georgiou, F. Porte'-Angel, *Synthetic turbulence, fractal interpolation, and large-eddy simulation*, Physical Review (2004) E70, 026310.
  - [15] A. Scotti, C. Meneveau, *A fractal model for large eddy simulation of turbulent flow*, Physica D (1999), vol. 127, pp. 198-232.
  - [16] S. Camarri, M. V. Salvetti, *On the approximate treatment of wall boundary conditions in large eddy simulation*, ADIA 2002-3, Dic.2002, Dipartimento di Ing. Aerospaziale L.Lazzerino, Pisa

- [17] L. Lanteri, *Parallel Solutions of three-dimensional compressible flows*, RT-2594, June 1995, INRIA Sophia Antipolis.
- [18] P. Roe, *Approximate Riemann solvers, parameters, vectors and difference scheme*, J. Comp. Phys. (1981), vol. 43, pp. 357-372.
- [19] B. Van Leer, *Flux vector spitting for the Euler equations*, Lecture notes in Physics (1982) vol. 170, pp. 405-512
- [20] R. Martin, H. Guillard, *A second order defect correction scheme for unsteady problems*, Comput. and Fluids (1996), vol.25, pp. 9-27.
- [21] P. Nivet, *A computational grid devoted to fluid mechanics*, Technical report, INRIA Sophia Antipolis, May 2004 in progress
- [22] S. Wornom, *Parallel computations of one-phase and two-phase flows using the Meca-GRID*, Technical report, INRIA Sophia Antipolis, RT-0297, August 2004.
- [23] J. Foss, *Interaction region phenomena for the jet in a cross-flow problem*, Rep. SFB 80/E/161.
- [24] J. Andreopoulos, W. Rodi, *Experimental investigation of jet in a crossflow*, J. Fluid Mech. (1984), vol.138, pp 93-127
- [25] R. Camussi, G. Guj, A. Stella, *Experimental study of a jet in a crossflow at very low Reynolds number*, J. Fluid Mech. (2002), vol. 545, pp. 113-144.
- [26] J. Andreopoulos, *On the structures of jet in cross-flows*, J. Fluid Mech (1984), vol. 157, pp. 163-197.
- [27] B. A. Haven, M. Kurosaka, *Kidney and anti-kidney vortices in crossflow jets*, J. Fluid Mech. (1997), vol. 352, pp.27-64.
- [28] H. Schlichting, In Z. Andew. Math. Mech. (1933), vol. 13, pp. 260-263.
- [29] T. F. Fric, A. Roshko, *Vortical structure in the wake of a transverse jet*, J. Fluid Mech. (1994), vol. 279, pp. 1-47.
- [30] S. B. Pope, *Turbulent flows*, University of Cambridge Press 2003
- [31] L. L. Yuan, R. L. Street, J. H. Ferziger, *Large-eddy simulation of a round jet in crossflow*, Journal of Fluid Mech. (1999), vol. 379, pp. 71-104



---

Unité de recherche INRIA Sophia Antipolis  
2004, route des Lucioles - BP 93 - 06902 Sophia Antipolis Cedex (France)

Unité de recherche INRIA Futurs : Parc Club Orsay Université - ZAC des Vignes  
4, rue Jacques Monod - 91893 ORSAY Cedex (France)

Unité de recherche INRIA Lorraine : LORIA, Technopôle de Nancy-Brabois - Campus scientifique  
615, rue du Jardin Botanique - BP 101 - 54602 Villers-lès-Nancy Cedex (France)

Unité de recherche INRIA Rennes : IRISA, Campus universitaire de Beaulieu - 35042 Rennes Cedex (France)

Unité de recherche INRIA Rhône-Alpes : 655, avenue de l'Europe - 38334 Montbonnot Saint-Ismier (France)

Unité de recherche INRIA Rocquencourt : Domaine de Voluceau - Rocquencourt - BP 105 - 78153 Le Chesnay Cedex (France)

---

Éditeur  
INRIA - Domaine de Voluceau - Rocquencourt, BP 105 - 78153 Le Chesnay Cedex (France)  
<http://www.inria.fr>  
ISSN 0249-6399